

**Nano-fabrication of Accommodative Intraocular Lenses Using Gray-scale
Electron Beam and Soft Lithography**

BY

EVAN ZAKER
B.S., Northern Illinois University, 2005

THESIS

Submitted as partial fulfillment of the requirements
for the degree of Master of Science in Electrical and Computer Engineering
in the Graduate College of the
University of Illinois at Chicago, 2012

Chicago, Illinois

Defense Committee:

Vitali Metlushko, Chair and Advisor
Jeremiah Abiade, Mechanical Engineering
Bruce Gaynes, Loyola University

ACKNOWLEDGMENTS

First, I would like to thank my advisor, Prof. Vitali Metlushko, for the opportunity to work on this research in the Nanotechnology Core Facility (NCF). I also want to thank him for employing me during part of my research and giving me several other opportunities through exposure on various projects. Next, I thank my thesis committee, Dr. Bruce Gaynes of Loyola University and Dr. Jeremiah Abiade, for reviewing my thesis and participating in my defense. Third, I am thankful for the mentoring and help that Kasun-Anupama Gardiye Punchihewa provided me in the course of this project. Also, I want to thank Bob Lajos and Dr. Se-Young An for the training and assistance that they provided me while researching in NCF. Finally, I thank my parents, Richard and Lorelei Zaker, for their continuing encouragement, Iris Caldwell for her support throughout my master's study and all of my friends for everything else.

EZ

PREFACE

The goal of my master's study was to gain semiconductor and micro-fabrication experience that was both theoretical and practical. As director of NCF, Prof. Metlushko had access to equipment and was heading the research in which I was interested. I am very pleased to work and perform research as part of his team at NCF. This opportunity is by far the highlight of my time at UIC.

The research presented in the thesis interested me for multiple reasons. First off, I received practical experience with micro-fabrication techniques. Second, it allowed me to research state-of-the-art equipment and processes. Last, because the project was interdisciplinary, it exposed me to a much broader subject matter in my research.

TABLE OF CONTENTS

<u>CHAPTER</u>	<u>PAGE</u>
1 Introduction	1
1.1 Reason for Study	1
1.2 Eye Biology	4
1.3 Lens Structure	9
1.4 Accommodation.....	15
1.5 Cataract.....	16
1.6 Cataract Surgery.....	18
1.7 Objective	21
2 Intraocular Lenses	23
2.1 Basic Optics	23
2.2 Fresnel Lens.....	29
2.3 History.....	31
2.4 Modern-Day	35
2.5 Types	37
2.5.1 Mono-focal.....	37
2.5.2 Toric	38
2.5.3 Multi-focal.....	38
2.5.4 Accommodative IOL	39
2.6 Future.....	40
2.7 Materials	43
2.8 Eye Biometry	47
2.9 Traditional Fabrication and Cost	48
3 Micro- and Nano-fabrication	50
3.1 Introduction	50
3.2 Electron Beam Lithography.....	55
3.2.1 Electron Theory.....	57
3.2.2 Vacuum Systems	57
3.2.3 Electron Sources.....	59
3.2.4 Acceleration Potential.....	63
3.2.5 Beam Blanker	63
3.2.6 Lenses.....	63
3.2.7 Stigmators	66
3.2.8 Apertures	66
3.2.9 Scanning	67
3.2.10 Stitching	67
3.2.11 Substrates	68
3.2.12 Photo resists.....	69
3.2.13 Resolution	70
3.2.14 Scattering and Proximity Effect.....	73
3.2.15 Environment.....	74
3.3 Gray-scale Lithography	75
3.3.1 3D Electron Beam Lithography	81
3.3.2 Soft Lithography.....	83

TABLE OF CONTENTS (continued)

<u>CHAPTER</u>	<u>PAGE</u>
4 Process	85
4.1 Design.....	85
4.1.1 Channels.....	86
4.1.2 Spiral	87
4.2 Substrate.....	89
4.3 Photo resist	89
4.4 Samples	90
4.5 Electron Beam Lithography System	91
4.6 Pattern	93
4.7 Image Generation and Conversion	95
4.8 Proximity Correction	96
4.9 Exposure.....	98
4.10 Development.....	98
4.11 Post Processing	99
4.12 Soft-lithography	100
4.13 Measurement.....	101
5 Results.....	105
5.1 Binary Spirals.....	105
5.1.1 Micro-spiral	107
5.1.2 Nano-spiral.....	108
5.2 3D Spirals	110
5.2.1 Dose Factor	110
5.2.2 3D Micro-spiral.....	111
5.2.3 3D Nano-spiral	113
5.3 Soft-lithography	116
5.3.1 3D Micro-spiral.....	116
5.3.2 Binary Nano-spiral.....	118
5.3.3 3D Nano-spiral	120
5.4 Larger Patterns.....	123
5.5 Proximity Correction	126
5.6 Thermal Reflow	126
5.7 Conclusion.....	132
5.7.1 Analysis	132
5.7.2 Improvements.....	132
5.7.3 Limitations.....	134
5.7.4 Alternative Additional Processing.....	136
5.7.5 Future Research	138

TABLE OF CONTENTS (continued)

<u>CHAPTER</u>	<u>PAGE</u>
Works Cited.....	139
Appendices.....	147
Calculation.....	148
Copyright Reprint Approvals.....	149
Vita	154

LIST OF TABLES

<u>TABLE</u>		<u>PAGE</u>
I.	COMMON IOL MATERIALS	45
II.	VARIOUS ELECTRON SOURCES AND THEIR PARAMETERS.....	62
III.	DEFAULT VALUES FOR PROCESS.....	105
IV.	NANO-SPIRAL DOSE FACTOR VS. MAX CHANGE IN DEPTH	113

LIST OF FIGURES

<u>FIGURE</u>	<u>PAGE</u>
1. Age-standardized disability-adjusted life year (DALY) rates from cataracts by country (per 100,000 inhabitants).....	2
2. Schematic diagram of the human eye.....	5
3. Diagram of the internals of the eye including the cornea, anterior chamber and posterior chamber.....	7
4. Accommodation by the lens.....	8
5. Stage of eye embryology.	10
6. Photomicrograph and diagram of the vertebrate lens.	11
7. SEM images of a rabbit lens.	13
8. AFM image of the healthy rabbit lens for a longitudinal section in the nucleus area, 15 mm 15 mm.....	14
9. A hypermature age-related cortico-nuclear cataract with a brunescent nucleus.	17
10. Phacoemulsification of cataract.	20
11. Diagram of a refracted light ray.....	24
12. Parallel light rays converge after passing through lens.....	26
13. Model of the optical system of the eye.....	28
14. Approximation of a normal lens (first on left) by a Fresnel lens (farthest right).	30
15. Anterior chamber lens.....	33
16. Iris-supported IOL.	34
17. Posterior chamber lens.....	36
18. Representation of a mono-focal IOL.....	37
19. Representation of a multi-focal IOL.....	39
20. DAC International MLC Mill/Lathe Combination System	49
21. Examples of PR contrast curves.....	52
22. Schematic of a EBL system	56

LIST OF FIGURES (continued)

<u>FIGURE</u>	<u>PAGE</u>
23. Generic electron band diagram.....	59
24. Cross-section of an Einzel electrostatic lens.....	64
25. Cross-section of an electro-magnetic lens.	66
26. Beam diameter vs. convergence angle.....	72
27. Example of forward and back scattering.....	74
28. Binary lithography exposure via mask and resulting PR profile.	75
29. Idealized PR contrast curve.	76
30. Energy absorbed at depth z.....	77
31. Varied dosing across the PR and its ideal development.....	78
32. Shades of gray approximated by half-tone in monochrome and continuous tone in true gray-scale.	80
33. Varying channel size and resulting curvature change.	86
34. Raith 100 e_LINE in NCF at UIC.....	93
35. Diagram of AFM operation.....	102
36. SEM of an AFM cantilever with tip.....	104
37. Microscopic image of SU-8 2150 structure with thickness of 600 μm	106
38. AFM scan of micro-spiral.....	107
39. AFM profile of micro-spiral.....	108
40. AFM of nano-spiral.....	109
41. Dose depth curve from nano-scale tests.....	110
42. Depth profile of a micro-spiral.....	111
43. AFM scan of a micro-spiral represented in a 3D image.....	112
44. AFM of 3D nano-spiral.....	114
45. Depth profile with curvature trend of a nano-spiral.....	115

LIST OF FIGURES (continued)

<u>FIGURE</u>	<u>PAGE</u>
46. AFM height profile of PDMS 3D micro-spiral	116
47. 3D image of AFM scan of PDMS 3D micro-spiral.....	117
48. Depth profile of PDMS binary nano-spiral.....	118
49. 3D AFM image of PDMS binary nano-spiral	119
50. AFM of PDMS 3D nano-spiral	121
51. SEM image of PDMS 3D nano-spiral.....	122
52. Optical microscope image of a large micro-spiral	124
53. AFM image of a large micro-spiral.....	125
54. Surface roughness from thermal reflow sample analysis	127
55. Depth profile for spiral after 0 minutes of thermal reflow	128
56. Depth profile for spiral after 5 minutes of thermal reflow	129
57. Depth profile for spiral after 10 minutes of thermal reflow	130
58. 3D AFM image of spiral after 10 minutes of reflow	131
59. Overview of the LIGA process used in creating a 3D lens.	137

NOMENCLATURE

AC	Anterior Chamber
AccIOL	Accommodative IntraOcular Lens
ACD	Anterior Chamber Depth
ACL	Anterior Chamber Lens
AFM	Atomic Force Microscope(y)
AHV	Acceleration High Voltage
AL	Axial Length
A-P	Anterior to Posterior
ASCII	American Standard Code for Information Interchange
BioMEMS	Biology Micro-Electro-Mechanical Systems
CCC	Continuous Circular Capsulorhexis
CEBL	Complementary Electron Beam Lithography
ChG	Chalcogenide Glass
CIF	Caltech Intermediate Form
CMTF	Critical Modulation Transfer Function
CNT	Carbon Nano-Tube
CSF	Calma Stream File
DMD	Digital Micro-mirror Device
DPL	Dip Pen Lithography
DUV	Deep Ultra-Violet
DXF	Drawing eXchange Format
e_LiNE	electron beam Lithography and Nano Engineering workstation
EA	Ethyl Acrylate
EBL	Electron Beam Lithography
ECCE	Extra-Capsular Cataract Extraction
EHT	Extra-High Tension
ELP	Effective Lens Position
EMA	Ethyl MethAcrylate

NOMENCLATURE (continued)

FE	Field Emission
GDSII	Graphic Database System II
GSL	Gray-Scale Lithography
GTM	Gray-Tone Masks
HEBS	High-Energy-Beam-Sensitive
HEMA	2-hydroxyethyl methacrylate
HEXMA	6-hydroxyhexyl methacrylate
HMDS	HexaMethylDiSilazane
HSQ	Hydrogen SilseQuioxane
ICCE	Intra-Capsular Cataract Extraction
IOL	IntraOcular Lens
LDW	Laser Direct-Write
LIGA	Lithographie, Galvanoformung, Abformung ¹
LT	Lens Thickness
MAP	Multi-photon Absorption Polymerization
MEMS	Micro-Electro-Mechanical Systems
MMA	Methyl MethAcrylate
MOEMS	Micro-Opto-Electro-Mechanical Systems
MTF	Modulation Transfer Function
MW	Molecular Weight
MWCNT	Multi-Walled Carbon Nano-Tube
NCF	Nanotechnology Core Facility
Nd:YAG	NeoDymium:Yttrium-Aluminum-Garnet
NIL	Nano-imprint Lithography
OPC	Optical Proximity Correction
PC	Posterior Chamber
PCL	Posterior Chamber Lens

¹ German for “Lithography, Electroplating, and Molding”.

NOMENCLATURE (continued)

PCO	Posterior Capsule Opacification
PDMDMS	Poly(DiMethylDipheylSiloxane)
PDMS	PolyDiMethylSiloxane
PE	PhacoEmulsification
PEA	Phenethyl Acrylate
PEMA	PhenEthyl MethAcrylate
PGMEA	Propylene Glycol Methyl Ether Acetate
PL	PhotoLithography
PMMA	Poly(Methyl MethAcrylate)
PR	Photo Resist
PVDF	PolyVinylidene Fluoride
RCS	Refractive Cataract Surgery
SAD	Self-Amplified De-polymerization
SEM	Scanning Electron Microscope(y)
SIA	Surgically-Induced Astigmatism
SPL	Scanning Probe Lithography
SPMs	Scanning Probe Microscopes
TEM	Tunneling Electron Microscope(y)
TFE	Thermal Field Emission
TFEMA	TriFluroEthyl MethAcrylate
UIC	University of Illinois at Chicago
VA	Visual Acuity
VLSI	Very Large Scale Integration
WD	Working Distance
WHO	World Health Organization
XUV	eXtreme Ultra-Violet

SUMMARY

An estimated 45 million blind people and 135 million visually impaired people live in the world, and an estimated 3.1% of deaths are directly or indirectly due to cataract, glaucoma, trachoma, and onchocerciasis. Cataract, which is clouding of the crystalline lens of the eye, is the leading cause of blindness world-wide. The only truly effective treatment of cataract is surgery to replace the lens with an artificial implant, which is known as an intraocular lens (IOL).

The ultimate IOL should restore vision and accommodation entirely like the original lens of the eye. A novel design of a spiral mold composed of nano channels is fabricated using advanced 3D electron beam lithography. Using the technique of soft lithography, IOL will be created from this mold. The main goal is to design the new type of IOL that will be reliable, versatile, cost and time effective.

1 INTRODUCTION

1.1 Reason for Study

An estimated 45 million blind and 135 million visually impaired people live in the world [1], and an estimated 3.1% of deaths are directly or indirectly due to cataract, glaucoma¹, trachoma², and onchocerciasis³. [2] Approximately 80 % of visually impaired people live in the rural areas of low-resource countries in Africa and Asia. [3] Out of this population, 7 million of the blind and 27 million of the visual impaired persons live in sub-Saharan Africa [4], which makes up 0.3 to 1.3 % for blindness⁴ and 1.4 to 3.6 % of low vision [3] of the population. According to the estimates of the World Health Organization (WHO), this gives Africa the highest prevalence of blindness and visual impairment for all of the regions. However, the rates of blindness are not much lower in other parts of the world. At the national level, Myanmar has one of the highest rates of blindness in the world [5], and among the Americas and the Caribbean nations, Haiti is among the worst at over 10 times the rate of Canada [6].

Cataract, which is clouding of the crystalline lens of the eye, is the leading cause of blindness world-wide. Responsible for 48 % of the cases [1], it is the focus of many global health initiatives. VISION 2020: The Right to Sight is a joint initiative of the WHO and the International Agency for the Prevention of Blindness whose goal is to eliminate avoidable blindness by the year 2020. [3] Curing cataracts is a major part of obtaining that goal. Cataracts affect approximately 18 million people, 90 % of whom are in low- to middle-income countries [7], and the rates of blindness or low VA are much higher in specific countries. In the Kilimanjaro Region of Tanzania, cataract accounts for 52.4 % of blindness and 70.6 % of visual impairment. In the Americas, Chile and Brazil have rates of 55 and 62 %, respectively, and among

¹ A group of eye conditions that lead to damage of the optic nerve, which carries visual information from the eye to the brain.

² A bacterial infection of the eye.

³ A Neglected Tropical Disease (NTD), also known as river blindness, caused by the parasitic worm *Onchocerca volvulus*.

⁴ According to the WHO, blindness is considered to be a visual acuity less than 20/400 (feet) or 3/60 (m).

the Caribbean nations at 60 %. Locally in Chimbote, Peru and Campinas, Brazil, the rates reach an estimated 72 to 74 %. [8] Figure 1 shows the effect of cataract world-wide.

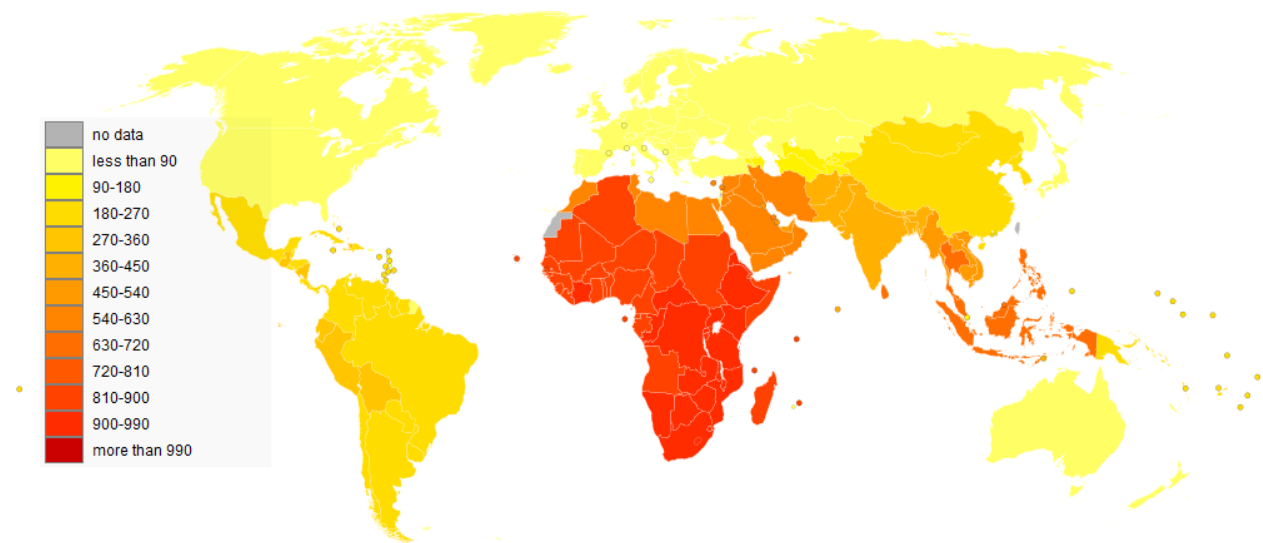


Figure 1 Age-standardized disability-adjusted life year (DALY) rates from cataracts by country (per 100,000 inhabitants).

Created by Lokal_Profil. http://en.wikipedia.org/wiki/File:Cataracts_world_map_-_DALY_-_WHO2004.svg. Image used under the Creative Commons Attribution-Share Alike 2.5 Generic license.

Although the United States has one of the lowest rates of all countries, cataract remains the leading cause of vision loss. Rates of blindness due to cataract are especially high in the Hispanic and African-

American populations at 27 %. [6] Treatments of cataract comprise 60 % of all Medicare costs related to vision. [9] The problem of cataract will increase as the population ages and risk factors, such as diabetes, become more prevalent. [6] According to some projections [9], cataract will increase 50 % and rise to 30.1 million by 2020.

In children, cataract is one of the most important causes of visual impairment and is responsible for 20 % of pediatric blindness. [10] In the Americas and the Caribbean, childhood (under age 15) blindness was estimated at 0.45 out of 1,000, and as much as 1.45 in 1,000 children from low-income countries in Africa and Asia. There are many causes of cataracts present at birth, such as prenatal infections (rubella, cytomegalovirus), maternal diabetes and hereditary disorders. Referred to as congenital cataracts, they are especially severe. Timely surgical intervention is extremely important in order to achieve good vision and sensory functioning. Visual deprivation during the pre-cortical stage of visual development, which is the first 6 weeks of life, will result in lazy eye (amblyopia¹) and disturb development of binocularity. [11] If cataracts are not removed within the first year of life, vision will never be fully regained. Furthermore, even though cataracts can be easily removed by surgery, it is imperative that the child receive glasses to correct loss of focus by removal of the lens; otherwise, the child will develop permanent visual impairment.

This is acutely problematic for the poorest regions of Africa and Asia because approximately three-quarters of the world's blind children live there. Congenital cataract also affects the immediate family by requiring additional time to care for and assist the affected child. In low-income countries, this extra time can result in a disruptive financial burden. Therefore, not only is blindness an outcome of poverty, but blindness can indeed further contribute to impoverishment. Further, successful cataract surgery can improve a household's economic status. [7] This is suggested by the estimation that better eyesight

¹ The loss of one eye's ability to see details.

would enable more formal education. [3] Thanks to improvements in surgical techniques that make it an outpatient procedure, cataract surgery is one of the most cost-effective of all health interventions [7]. Even though that is true, lack of insurance [6], and therefore cost, was the highest reason recorded [5] for being unable to have the procedure performed. Unlike in wealthier countries, such as Japan, where routine cataract surgery is highly cost-effective for both eyes [12], cataract extraction can be performed, for example, in Myanmar for \$20 – approximately 3 weeks of income for a village farmer. [5]

Although it is difficult to measure the total amount of blindness in society [13], the rates are staggering and cannot be ignored. The largest rates of blindness are in low-income countries, and a large portion of these cases are caused by cataracts. Unilateral or bilateral cataract is a leading cause of treatable blindness. [14] Although there are many drugs alleging anti-cataract properties around the world, there has been no evidence of effectiveness shown through rigorous clinical investigations [15]. The only truly effective treatment of cataract is surgery to replace the lens with an artificial implant, known as an intraocular lens (IOL).

1.2 Eye Biology

Before further explanation of IOL and the surgical procedure, it is necessary to review the biology of the eye. The eye is a complex optical system that collects light from the surrounding environment, regulates its intensity, focuses and converts it into a set of electrical signals. Light first hits the cornea, which is referred to as the “window” of the eye. The cornea is the area of strongest focusing power and accounts for two-thirds of the optical power of the eye; however, its focus is fixed. There are five layers of the cornea and the outermost, the epithelium, makes up 90 % of it. The layers are thinnest in the center of the eye.

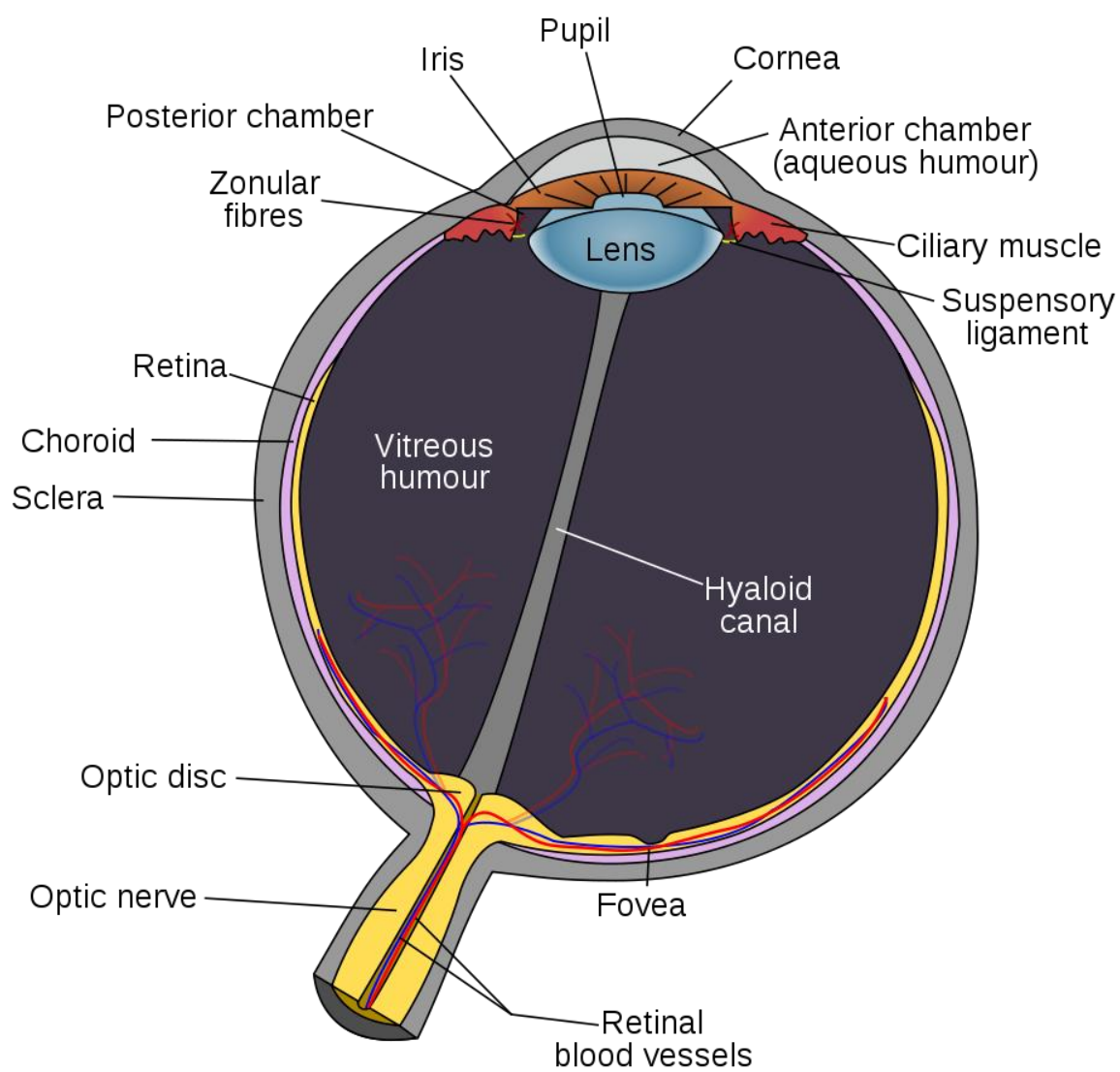


Figure 2 Schematic diagram of the human eye.

Shown in Figure 2, the inside of the eye is divided into two segments: the anterior and posterior. The anterior segment is further divided into two chambers anterior (front) and posterior (rear). Between the cornea and the iris is the anterior chamber that contains aqueous humour, a fluid that provides nutrients to areas lacking blood vessels, such as the crystalline lens and the cornea. Separating the anterior and posterior chambers is the iris. The iris expands and contracts in order to adjust the size of the pupil, which is the opening in the middle, and thus controls the amount of light entering the eye.

The magnified cross-section of the eye (see Figure 3) shows the crystalline lens of the eye loosely opposed to the iris in the posterior chamber and suspended by fibers called zonules that are attached to ciliary muscles. Unlike the cornea, the lens' focus can be adjusted, which provides the remaining one-third of the eye's total optical power. The ciliary muscles along with the zonular fibers enable changes in the lens' shape. In relaxation of the ciliary muscles, the zonular fibers become taut causing the lens to flatten out and thus increasing long range focus. Contraction of the ciliary muscles pulls towards the axis of the eye making the lens more spherical and increasing the power for short range focus. In addition, the eyes converge and the pupil gets smaller. This entire process, called accommodation, focuses light onto the retina as shown in Figure 4. Accommodation plays a role in depth perception as the brain uses the amount of focusing to approximate distance to an object.

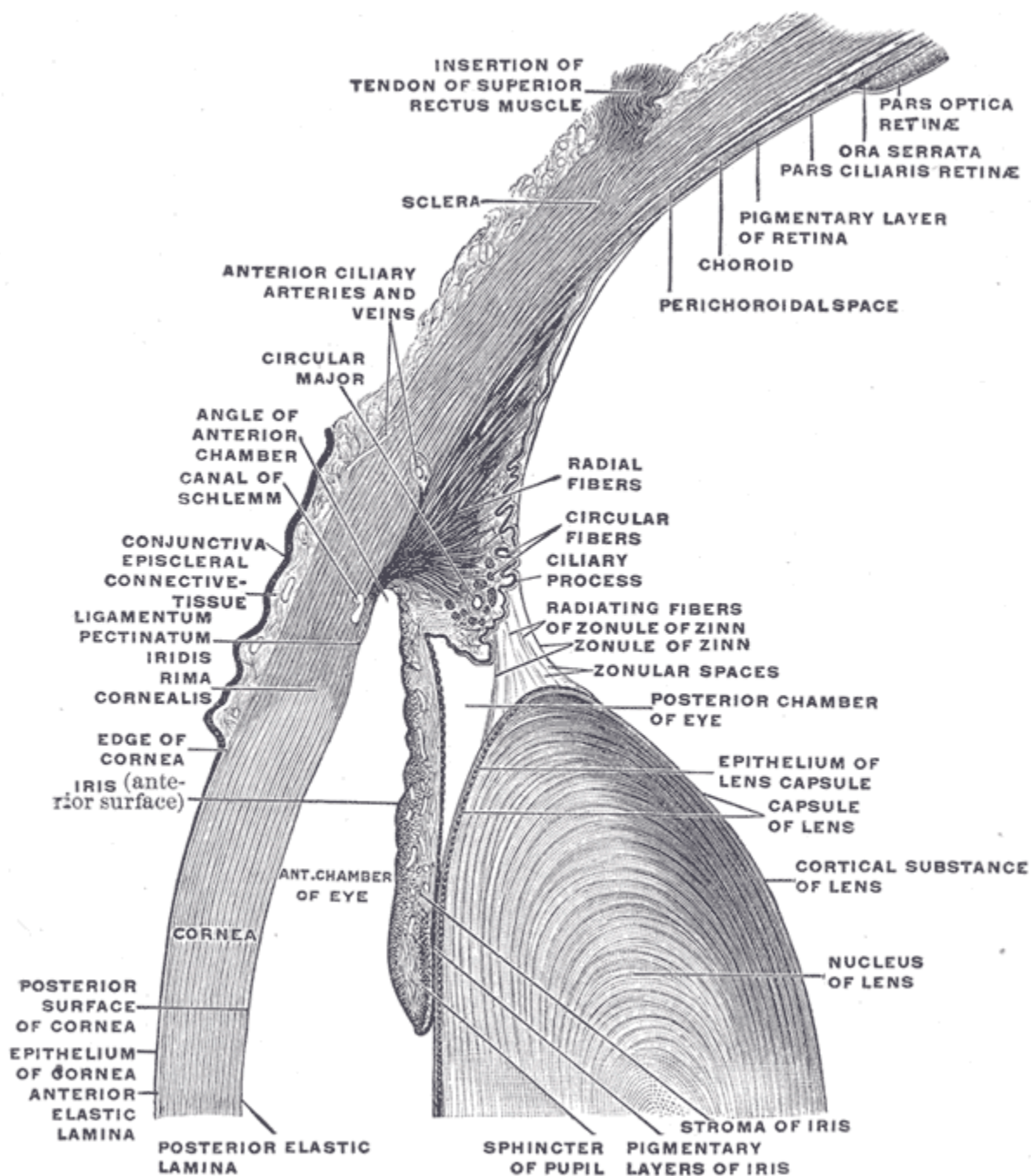


Figure 3 Diagram of the internals of the eye including the cornea, anterior chamber and posterior chamber.

Gray's Anatomy. Public Domain.

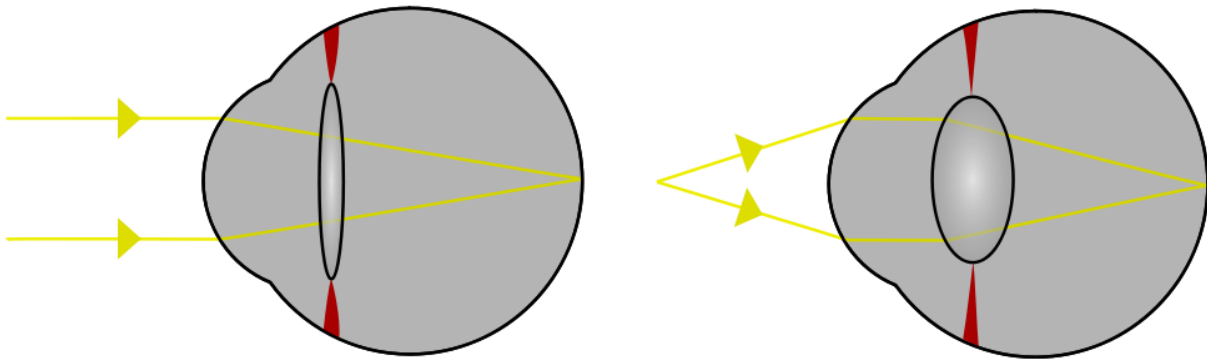


Figure 4 Accommodation by the lens.

Created by Erin Silversmith and Theresa Knott. Used under the Creative Commons Attribution-Share Alike 2.5 Generic license.

The human lens is not perfect and can have many refractive errors such as astigmatism, myopia and hyperopia. Astigmatism is an aberration due to the inability of the eye to focus to a sharp point on the retina and therefore makes the image blurry. Myopia, commonly known as nearsightedness, occurs when the lens cannot adjust to objects in the distance. Hyperopia, or farsightedness, is the opposite; and is the inability of the lens to adjust to objects up close. Presbyopia is the combination of myopia and hyperopia, and it usually starts to affect people around the age of 45.

Finally, the posterior segment of the eye contains the vitreous, choroid and retina. The vitreous fills the eye with a jelly-like fluid. The choroid contains blood vessels for the retina. And, the retina contains the photoreceptors – rods and cones – that convert the light into neurotransmitters.

1.3 Lens Structure

The physiology, or the active transport mechanisms of metabolites, of the eye is not of concern in this paper. Rather, it is more important to understand the structure of the lens and its physical nature. The lens is a biconvex structure (or, asymmetrical oblate spheroid [16]) and has an elliptical shape when viewed from the side. Its thickness measures about 3.5 to 4.0 mm anterior to posterior (A-P) and diameter is typically between 9.0 to 10.0 mm. [15] The overall structure of the lens is composed of three main parts: capsule, epithelium and fibers. The fibers form the interior of the lens and are then covered by the epithelium and encased by the lens capsule.

The normal anatomy of the lens is better understood through its embryology. Very early in the formation and development of the embryo (embryogenesis), lens cells form. Shown in Figure 5, the forebrain, i.e., prosencephalon, small inverted membrane-enclosed sacks, or optic vesicles, enlarge and come into contact with the primary cell layer of an embryo, known as the surface ectoderm. This thickens in order to form the lens plate. Simultaneously, the optic vesicle begins to fold inward (i.e., invaginate), and an indentation called the lens pit forms. Surface ectoderm cells multiply while the lens pit continues to invaginate. A sphere of cells eventually breaks off the stalk that connected it to the remainder of the surface. This becomes the lens vesicle and is composed of a single layer of cuboidal cells within a basement membrane called the lens capsule. The thickness of the lens capsule varies from its thickest at the anterior to the thinnest at the posterior pole.

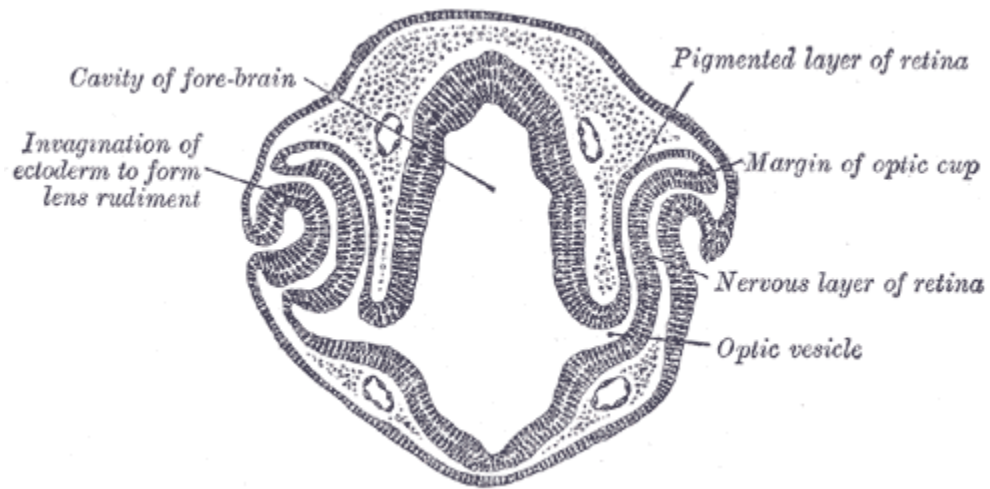


Figure 5 Stage of eye embryology.

Gray's Anatomy. Public Domain.

Posterior cells of the lens vesicle elongate towards the anterior and become the primary lens fibers. The fibers meet the anterior lens cuboidal cells and eliminate any open space (lumen¹) inside the lens vesicle. The primary lens fibers form the embryonic nucleus as shown in Figure 6, and the anterior lens cuboidal cells become the lens epithelial cells. A layer of lens epithelium exists on the anterior and just posterior to the equator. Normally, there are no epithelial cells present on the posterior of the lens.

¹ The inner open space or cavity of an organ.

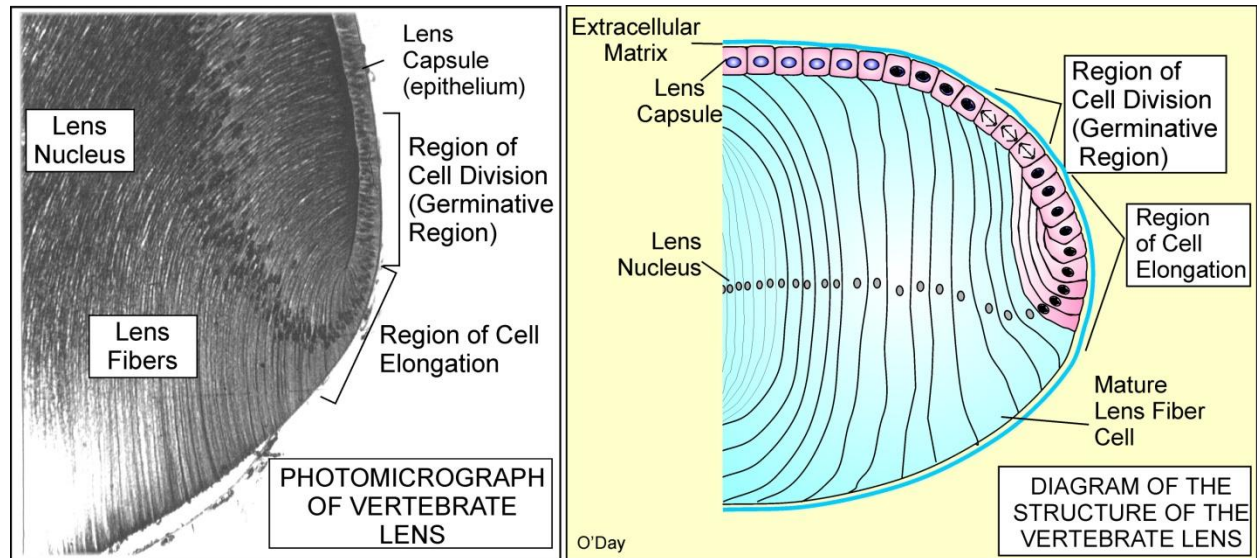


Figure 6 Photomicrograph and diagram of the vertebrate lens.

Image courtesy of Dr. Danton O'Day, University of Toronto Mississauga, Canada.

Described simply, lenses are stratified epithelia. [17] Epithelial cells multiply and elongate toward the anterior under the lens epithelium and toward the posterior only under the lens capsule. These form the secondary lens fibers that, during fetal growth (gestation), form the fetal nucleus. New lens fibers are overlain onto the fibers that preceded it in development and results in the growth of new layers. Unlike other stratified epithelia, these layers are never removed but are further internalized by the creation of newer layers.

At birth, the lens is approximately 6 mm in diameter. [18] In childhood and early adolescence, lens fibers further surround the fetal nucleus to become the juvenile nucleus. Eventually, continued growth of the lens fibers forms the adult nucleus. The most peripheral lens fibers between the nucleus and capsule make up the cortex.

Lens fibers are arranged in ordered radial cell columns that emanate from the lens center. When lens fibers meet on the anterior and posterior, the abutting ends form what are called sutures, which are Y-shaped. The asymmetrical oblate spheroidal shape comes from the end-to-end arrangement of crescent-shaped lens fiber cells into concentric shells, much like that of an onion [18]. Lens crystallins, which are specialized crystalline proteins, are in high concentrations in the cytoplasm of lens fiber cells. As the lens grows, a gradient of refractive index occurs from the center because of a variation in protein content. [16]

To further understand the structure, scientists have used scanning microscopy, such as scanning electron microscopy (SEM) and atomic force microscopy (AFM). These types of measurement technology not only allow scientists to see the lens in more detail but also allow for more accurate measurement of the structures. In addition to human lenses [19], a healthy rabbit lens has been measured and characterized. As shown in Figure 8, the lens fibers of a rabbit were found to have a mean diameter of 200 nm by AFM. The distance between the shells was determined as 4 mm. In the cortex, hexagonal structures measured with widths between 5.0 and 3.0 mm. [20]

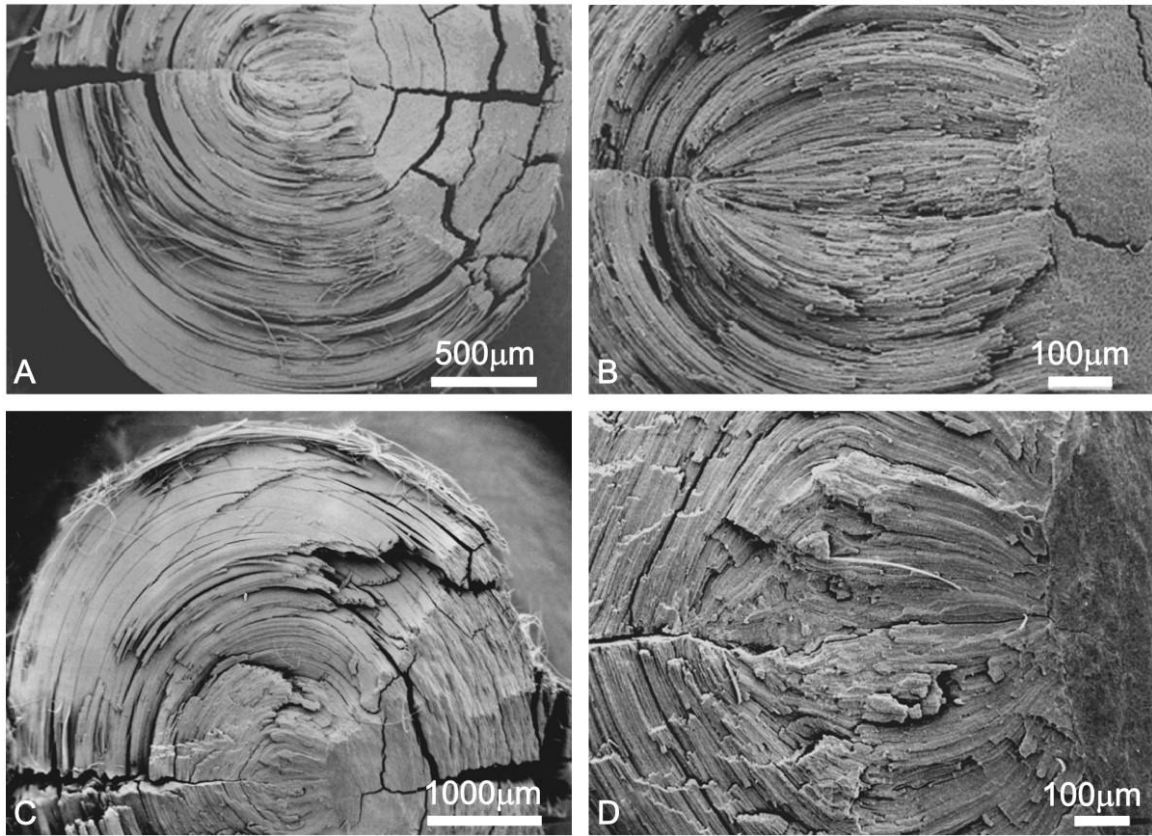


Figure 7 SEM images of a rabbit lens.

Included with permission from Dr. Bruce Gaynes, Loyola Univeristy.

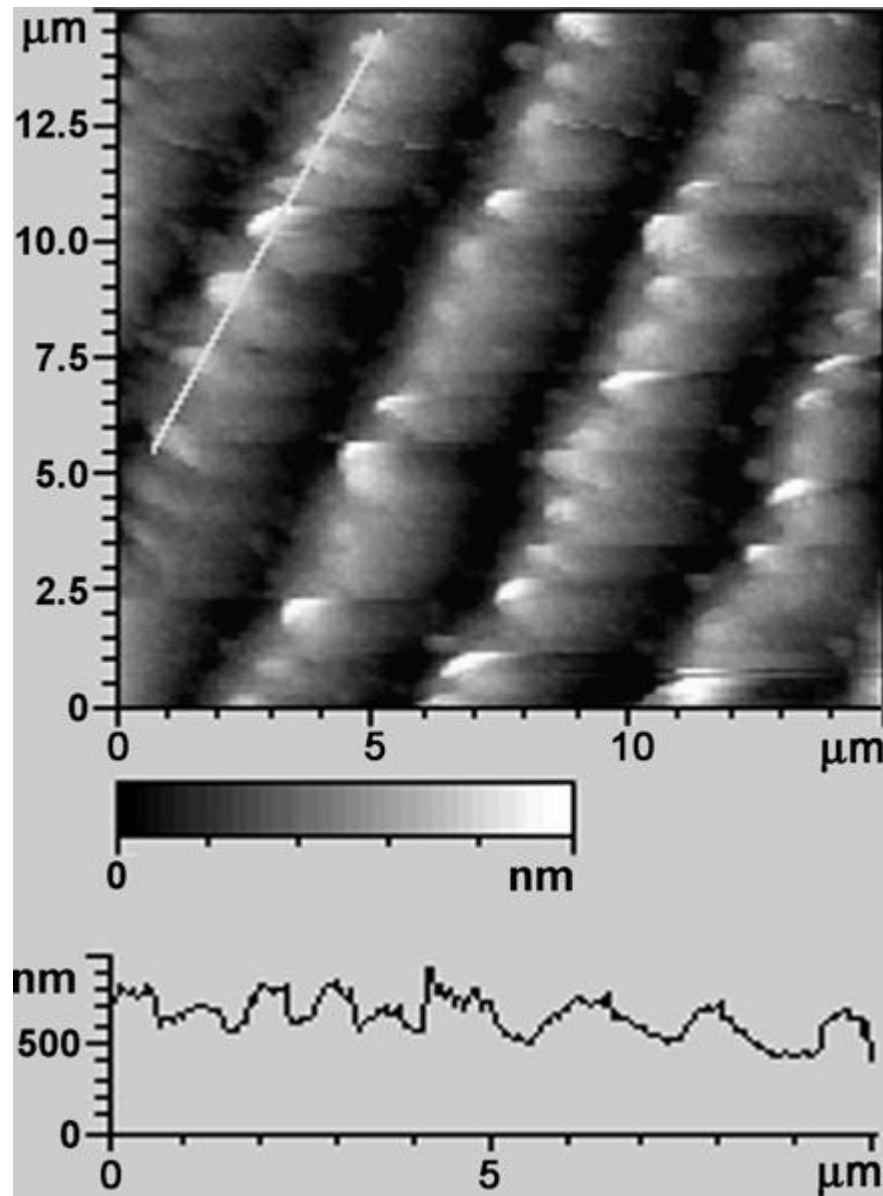


Figure 8 AFM image of the healthy rabbit lens for a longitudinal section in the nucleus area, 15 mm 15 mm.

Figure from [20]; printed with permission by Andrea Antunes, Universidade Federal de Uberlândia.

In summary, the basic lens structure consists of a capsule lined with the epithelium and a peripheral cortex filled with lens fibers that make up the inner nuclear core. The nuclear core is made up of several concentric layers: (1) 4 % the embryonic nucleus, which is the inner most core; (2) 49 % the fetal nucleus; (3) 30% the juvenile/adult nucleus; and (4) 21 %the epinucleus, which is the innermost (supranuclear) cortex. [19] The cortex and nucleus, and therefore lens fibers, form the bulk of the interior of the lens. Evaluation of the morphology of lens fibers by scanning electron microscopy (SEM) showed that the cells in embryonic and fetal nucleuses were rounded, while in the adult nucleus, they were flattened. [15]

1.4 Accommodation

The crystalline lens grows throughout life. Starting as round in childhood, it flattens out in old age. This accounts for some of the loss of accommodation that comes with age. The rest can be attributed to elasticity. The lens retains all of the cells that it has formed since embryogenesis. As the nucleus compresses during growth, it becomes less pliable. The nucleus also increases rigidity, a condition known as sclerosis, due to the incorporation of cholesterol with phospholipids in the lens membranes. The cholesterol-to-phospholipid ratio, a measure of capsular rigidity, also increases with age. A more rigid lens causes the loss of accommodation and is known as presbyopia.

The lens capsule is responsible for the elasticity of the lens and allows the lens to accommodate; however, this is not the whole story. For more than a century, it was assumed that accommodative changes in the lens were due to the relaxation of the lens zonules and the elasticity of the capsule. More modern techniques have shown that forces on the lens, such as from the ciliary body deform the lens back, and the capsule distribute these forces. [15]

1.5 Cataract

Because the primary function of the crystalline lens is to dynamically focus light entering through the iris onto the retina, it must be transparent. The transparency is due to extraordinarily regular fiber arrangement and cell shape, regular cell volume, minimal extracellular space, minimal scatter elements, as well as minimal spatial variation in the index of refraction relative to the wavelength of incident light. [15] The preservation of this unique structure allows the lens to maintain its transparency through its development. [17]

A cataract is a clouding of the lens (see Figure 9). Besides lessening visual acuity (VA), cataracts can cause aberrations such as monocular double or triple vision. There are many causes of cataracts: exposure to radiation, long-term exposure to ultraviolet light, diseases such as diabetes, the natural aging process and trauma. Nuclear sclerosis, mentioned before for affecting accommodation, deforms the cells, increases scattering and contributes to the formation of cataract. The natural suture planes also detract from the optical quality of the lens.

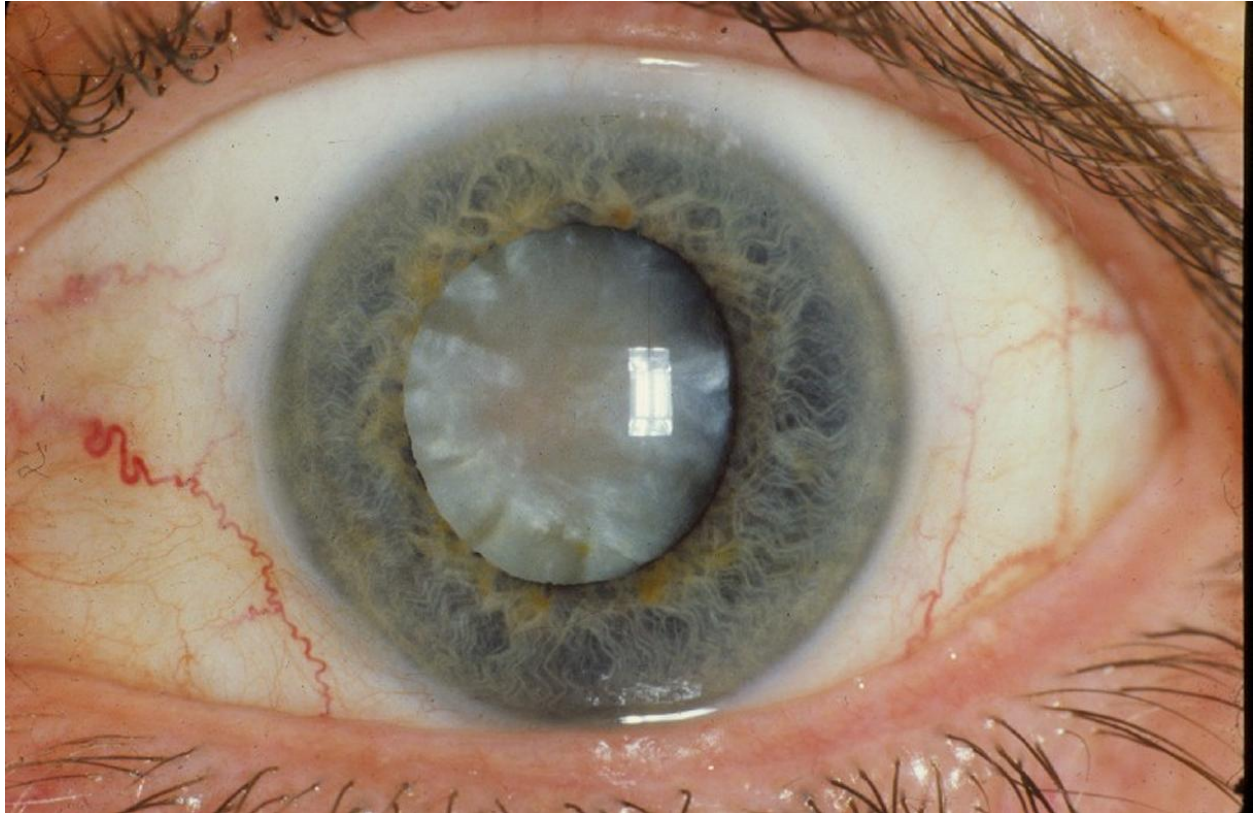


Figure 9 A hypermature age-related cortico-nuclear cataract with a brunescent nucleus.

Image from the National Eye Institute.

Although the lens is thought to be mostly clear, the fetal lens actually is a faint yellow color, and an older lens may be golden yellow, orange, reddish brown or even black. This change in color is called brunescence, and is an age-related accumulation of chromophores, such as oxidized tryptophan (N-formylkynurenine) non-enzymatically glycosylated protein. Some amount of brunescence is beneficial because it reduces glare. However, advanced cases cause reduction in high-contrast acuity and sensitivity. There is good clinical correlation between light scattering, the intensity of brunescence and the hardness of the posterior nucleus [15], and it may contribute to cataract.

Transparency in the nucleus can also be lost through opacification (opalescence) when light-scattering foci in the nuclear fiber cytoplasm or nuclear plasma membrane are formed. These foci contain either huge protein aggregates from sulfhydryl (-SH) groups oxidized to form protein-protein disulfide (-SS-) bonds or by larger molecules that have higher refractive indices. Elevated concentrations of the oxidant hydrogen peroxide (H₂O₂), which allow oxidation of nuclear components, were found in patients with maturity-onset cataracts.

1.6 Cataract Surgery

Removal of visually significant cataracts reduces the risk of injury to and improves the quality of life for a patient. Cataract extraction surgery has proven to be generally safe and highly successful. [21] The modern combination of cataract removal and refractive surgery has created an ophthalmologic subspecialty of technology and surgeons: refractive cataract surgery (RCS). [22] RCS encompasses not only IOL but breakthrough surgical technology as well.

From 1960 to 1970, intra-capsular cataract extraction (ICCE)¹ became the method of choice because extra-capsular cataract extraction² (ECCE) had major complications. However, ICCE has its own

¹ Removal of the lens and capsule in one piece.

² Removal of the lens while leaving the back of the capsule in place.

complications because it leaves the eye without any barrier between the AC and PC and, as a result, disturbance and stress affected the iris, vitreous, retina, and choroid. ECCE became a popular method again because of phacoemulsification (PE). Invented in 1969 by Dr. Charles D. Kelman, the PE procedure is a method for using ultrasound to emulsify the lens and performing ECCE through a small incision, as shown in Figure 10. PE is a relatively safe procedure due to the equipment used. [23] PE surgery, along with foldable IOL implanted into the eye, provides less corneal distortion, less postoperative inflammation, lower surgically-induced astigmatism¹ (SIA), and therefore speeds up recovery time for patients. The degree of SIA varies according to the size of incision made, presence of sutures and number of sutures used. Today, PE is used completely for the removal of the lens. [24]

Cataract surgery has become quite routine, and there are some essentials to the process that are relevant for future discussion in this paper. Heavy medical detail will be omitted in order to focus on how the IOL fits into the picture. As with most surgeries, the process is preceded by preoperative consultation and examination. Specifically, the patient's eye must be measured to determine the power of IOL to implant as discussed in greater detail in Section 2.8.

The actual surgery begins by putting the patient under general anesthesia. Then, the eyelid is kept open by using a lid speculum, while the eyeball, or globe, is stabilized by a rod. A small, clear incision is made into the cornea, and viscoelastic gel is injected into the eye in order to stabilize the pressure and the internal structure. The cataract lens is then chopped into pieces and one-by-one brought into the anterior chamber, emulsified and then removed. Finally, once the nucleus and cortex are removed, a foldable IOL is implanted behind or in front of the iris. Because PE requires minimal incision, it allows for wound closure without sutures.

¹ Astigmatism makes it difficult to see fine details, either close up or from a distance.

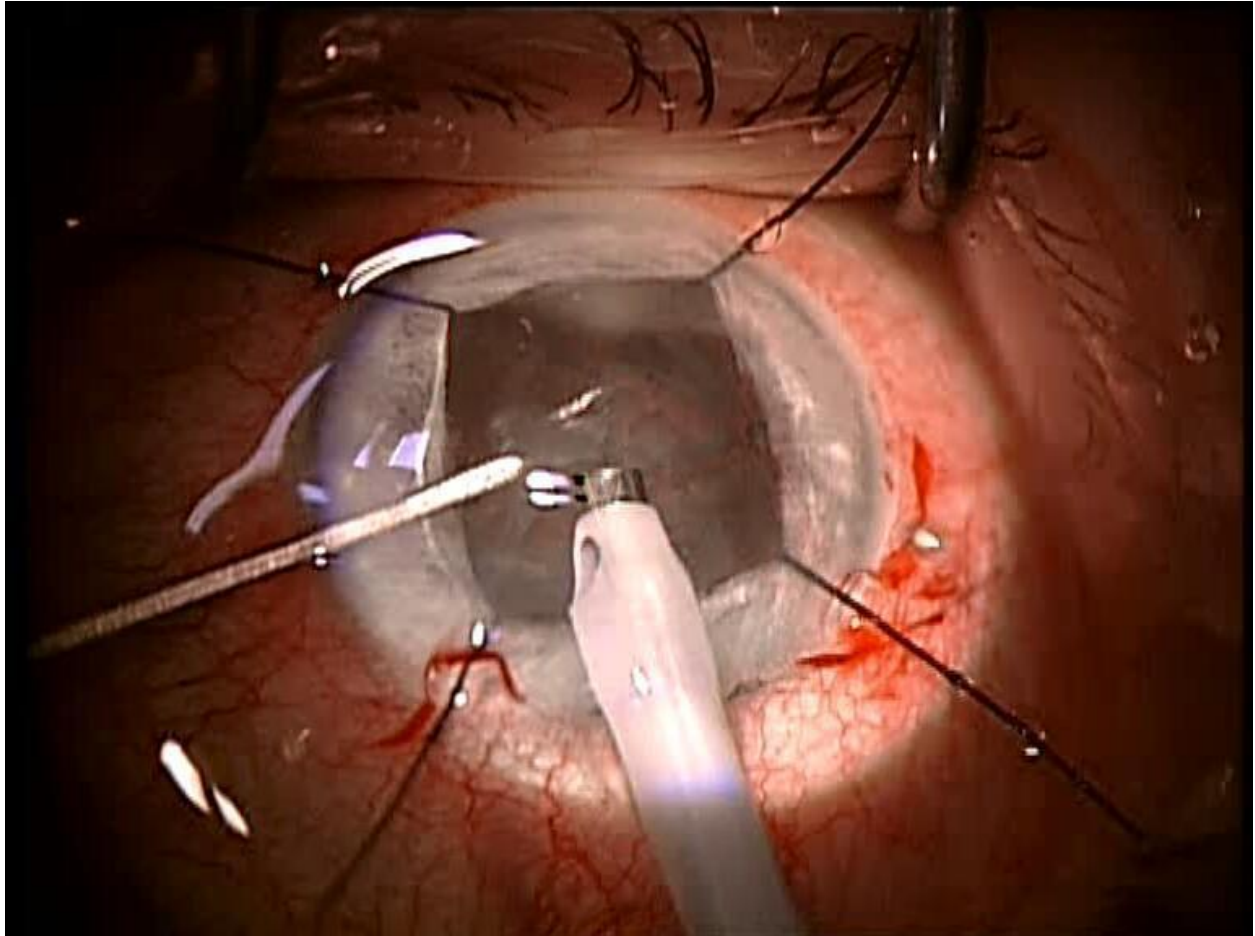


Figure 10 Phacoemulsification of cataract.

Copyright Online Journal of Ophthalmology. [<http://onjoph.com>] Juenemann, Anselm, Prof. Dr. med., Augenklinik mit Poliklinik, Universität Erlangen, Deutschland¹, 5, Erlangen, Deutschland.

It is possible for complications after cataract surgery. Posterior capsule opacification (PCO), also known as aftercataract, is opacity of the natural lens capsule following surgery. PCO can occur several months or years after cataract surgery and cause as much or more vision loss as the original cataract. There is a simple procedure called neodymium:yttrium-aluminum-garnet (Nd:YAG) laser capsulotomy¹ that can correct the issue. This is an outpatient procedure in which a laser is used to cut a hole in the back lining of the lens capsule. Without the opaque capsule disrupting light, vision is then restored.

The practice of RCS encompasses not simply the surgical methods and refractive IOL implantation, it also involves refining the procedures to improve post-surgery effects. Because of the improvements in RCS, cataract patients are having surgery at earlier ages, and they are also seeking solutions that not only correct their cataract but improve the quality of life after surgery. [22] With all of the technical advances in RCS, the future seems to lie with more sophisticated IOL. [25]

1.7 Objective

The research described in this paper focuses on a future design of the IOL. The overall purpose of this research is two-fold. First, it is to revolutionize the design of the IOL. The ultimate IOL should restore vision and accommodation entirely like the original lens of the eye. Second, it is to lower the overall production cost of IOL. Lowering cost and improving the production of IOL is fundamental in serving the 90 % of patients living in low-income countries.

The ideas proposed in this paper build upon those of Nithya Jayapratha, whose work at the Nanotechnology Core Facility at the University of Illinois at Chicago (UIC) was the first to propose using micro-fabrication techniques in the creation of IOLs. In her thesis [26], a novel spiral design composed of micro channels that mimics the natural repeating patterns in the lens fibers was introduced. An optimal design was chosen by calculating the power of the lens taking into account the compression and

¹ An incision into the capsule, such as in an operation to remove a cataract.

elongation of the lens. Micro-fabrication techniques, such as deep ultra-violet (DUV) and X-ray lithography, were explored to fabricate better lenses that are also less expensive to fabricate. Finally, there was an investigation on various materials used in the process.

Jayapratha's research was not able to produce prototype IOLs with the required focal power for a fully accommodative eye. The micro-channels composing the IOL were too wide; especially compared to the fiber thickness of a natural lens. The width of the channels caused the lens to be too inflexible. Flexibility is especially important in older eyes and eyes post surgery. This was a limit imposed by the micro-fabrication technology used. The design was also very complex; it involved several layers of spirals connected by an interlocking mechanism, which was never discussed. However, the general concept of fabricating IOLs using micro-fabrication techniques remains to be novel, and the process shows great potential. This research further expands the fabrication of IOLs into the nano-manufacturing regime.

The research will act as a proof-of-concept of the new design and fabrication of IOL. Fabrication of molds of the spiral pattern will be done by electron beam lithography (EBL), and soft lithography will be used to create the actual lens using flexible polymer materials. The flexibility is necessary for accommodation and should match that of the eye. This project will act as an initial proof of concept. In this research, test patterns of an accommodative IOL will be fabricated using electron beam lithography in order to test the feasibility of the design and explore the techniques used. Eventually, the lens could be implanted and tested in a rabbit models.

2 INTRAOCULAR LENSES

2.1 Basic Optics

There are several terms that will be referenced in order to measure and compare any lens, such as refractive index, focal distance, and power. Each will be introduced separately.

Refractive index is a measure of the speed at which light travels through a material. Light travels at a constant speed in vacuum but at different speeds through various materials. The ratio of the speed of light travelling through a particular material (v) and the constant speed of light through vacuum (c_0) is the refractive index (n).

$$n = \frac{c_0}{v}$$

Sometimes called the mean refractive index, it is measured in the middle of the visible spectrum (yellow-green). Specifically, the index can be measured at 587.56 nm wavelength for the helium 'd' line (n_d) or 546.07 nm for the mercury 'e' line (n_e).

The refractive index of materials is not constant for all wavelengths of light. Constringence (Abbe number) relates the mean refractive index of the blue and red ends of the visible spectrum. Constringence can be calculated as

$$V_d = \frac{n_d - 1}{n_F - n_C}$$

where n_F and n_C represent the F- and C- spectral lines (486.1 nm and 656.3 nm), respectively. The effect of constringence is most observable in the spreading of different colors of light by a prism. If this occurred in IOL, the color fringing would be very disabling. Therefore, constringence must be kept to a minimum in the materials used to fabricate IOLs. Luckily, constringence tends to decrease as the

refractive index increases. Poly(methyl metacrylate) PMMA, a popular material in IOL fabrication, has a measured value of 58 for constringence, which is the same as the high-index crown glass used in the early production of glasses. The reciprocal of constringence is dispersive power, which is more commonly used for measurement.

Refraction is the very reason that lenses function as they do. Refraction happens when light transfers from one medium with a certain refractive index to another material with a different refractive index. Due to the changing of speed, a light ray incident on the interface, for every angle other than directly normal (90°), will leave the interface at a different angle; as shown in Figure 11.

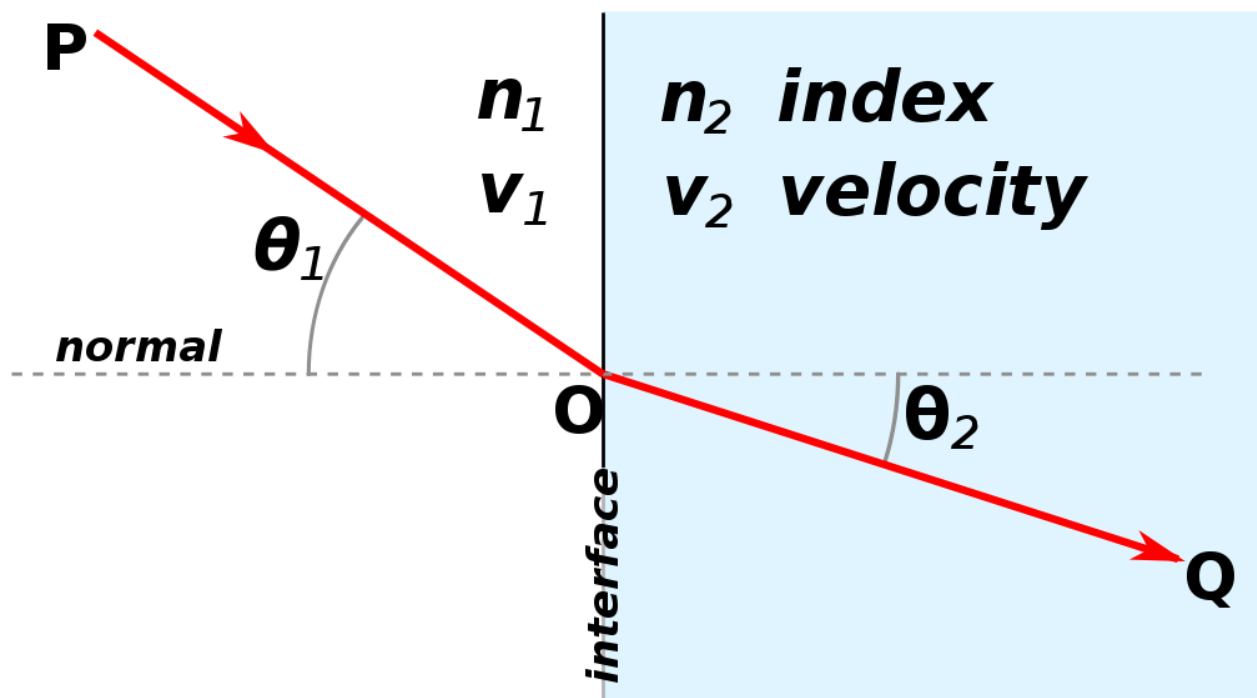


Figure 11 Diagram of a refracted light ray.

The relation between these angles is dependent on the refractive index and is represented by Snell's Law:

$$n_1 \sin \theta_1 = n_2 \sin \theta_2$$

Refractive index is then an indication of how much the angle changes when travelling between two materials. The higher the refractive index, the more a lens bends light, and the thinner a lens can be. The change in angle along a non-planar surface, such as a sphere, results in a converging or diverging effect that causes magnification. Fundamentally, a lens is simply an object that converges or focuses light to a certain point, i.e., the retina.

Refraction is apparent in the way objects appear to be bent underwater. The interface is made up of water with a n of 1.333 and air with a n close to 1, and light rays bend when they exit (and enter) the water. Refraction is also the reason that objects look distorted when we see under water. The cornea and aqueous humor have a refractive index of 1.376 and 1.336, respectively, and are very close to that of water. The lens, however, has a higher index of refraction: 1.41. [27] Therefore, when we see under water, most of the light is bent only by the lens and not the cornea or aqueous humor.

The terms power and focal distance are used to describe the focusing ability of a lens system. Focal length of a lens is the distance (f) from a lens that collimated rays converge, as shown in Figure 12. Focal length can be measured using any unit of length, yet is usually given in meters (m) for theoretical calculations and millimeters (mm) for camera lenses used in photography.

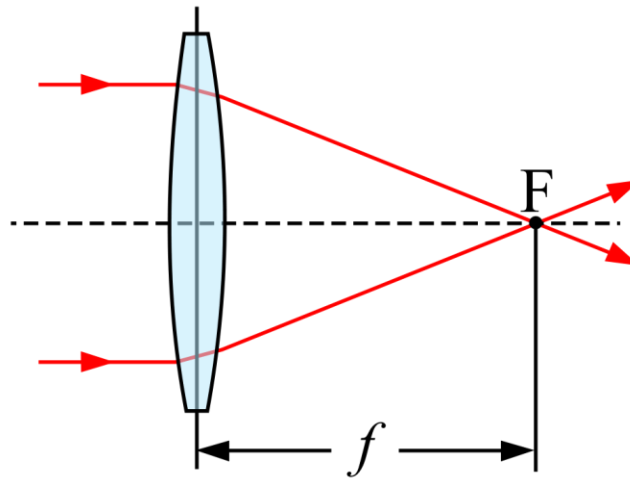


Figure 12 Parallel light rays converge after passing through lens.

The thin lens formula shows how focal length relates to the focusing of an image, specifically, the distance to an object, S_o , and the distance to the image in focus, S_i :

$$\frac{1}{f} = \frac{1}{S_i} + \frac{1}{S_o}$$

At a very large distance – for example, looking at an object across a field – S_o approaches infinity. The equation then results in the image being in focus at the focal distance of the lens system:

$$\frac{1}{f} = \frac{1}{S_i} + \frac{1}{\infty} \rightarrow \frac{1}{f} = \frac{1}{S_i} \rightarrow S_i = f$$

Because images must be in focus on the retina and the size of the eye is fixed, the focal distance of the eye must change in order to accommodate for objects at different distances.

Power is also a measure of focus and is equal to the reciprocal of focal distance. The unit for power is diopter (D), which is equal to an inverse meter (m^{-1}). Using power (P), or vergence, V_o and V_i of the object and image, respectively, simplifies the lens equation by removing the reciprocal terms and making them directly additive.

$$V_o + V_i = P$$

Using the measurement of power is especially useful in dual lens systems as it allows the lens' powers to add directly.

For a thin lens the focal distance can be calculated as

$$\frac{1}{f} = \frac{n_2 - n_1}{n_1} \left(\frac{1}{R_1} - \frac{1}{R_2} \right)$$

where n_2 is the refractive index of the lens material; n_1 is the refractive index of medium surrounding the lens, such as air or water; R_1 is the radius of curvature of the front of the lens; and R_2 is radius of curvature for the back of the lens.

However, in practice, the thick lens equation is a better approximation for realistic lenses. The thick lens equation takes into account the thickness between the front and back surfaces of the lens. The thick lens equation is also known as the lens maker equation and is represented as follows:

$$\frac{1}{f} = (n - 1) \left[\frac{1}{R_1} - \frac{1}{R_2} + \frac{(n - 1)d}{nR_1R_2} \right]$$

Because it is assumed that an external lens, such as in eyeglasses, is surrounded by air (i.e., $n_1 = 1.000$), n represents the refractive index of the lens material. The thickness of the lens is represented by d .

The optical system of the eye can be modeled by several lenses and the spacing between them as shown in Figure 13. First, there are glasses or spectacles that many people wear, and they are a certain distance

away from the cornea (t_s). The distance between the cornea and the retina (t_{al}), also referred to as axial length, is fixed. Therefore, the focal power of the cornea are fixed. Eyeglasses, which many people wear, are a certain distance from the cornea (t_s) and the focal power is specified by the prescription using the same properties of lenses described above. Lastly, the lens of the eye does the final focusing. As explained in Section 1.2, the lens actually changes shape and therefore, focal power as necessary. Alternatively, the same effect can be achieved by shifting the lens forward. This process is used with some IOLs, which will be seen later. At a relaxed state (emmetropia), the eye is focused on objects more than 20 feet (6 m) away. This distance is represented by the solid lined lens as designated t_{emm} . The fully accommodated lens is shifted forward as designated by the distance t_{acc} and the dotted line lens.

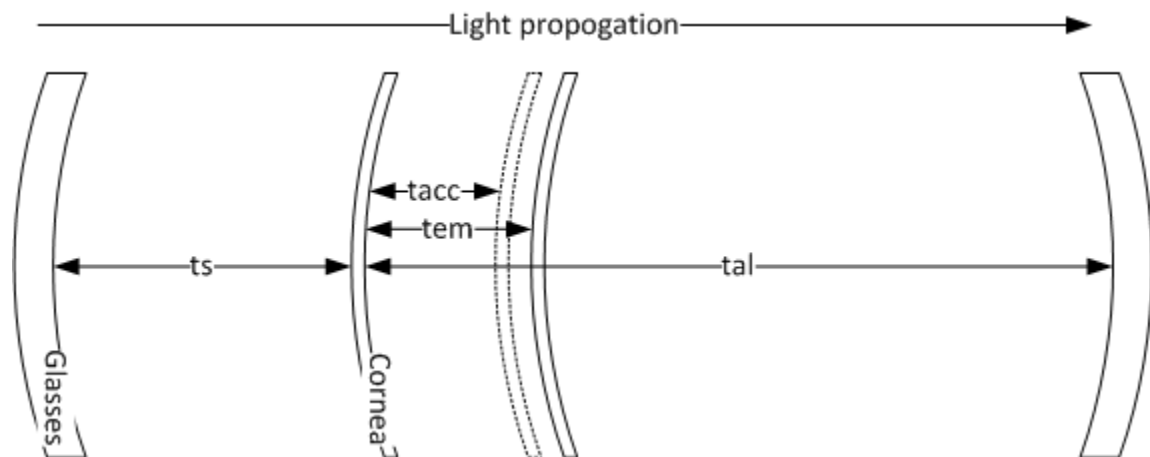


Figure 13 Model of the optical system of the eye.

2.2 Fresnel Lens

In general, increased radius of curvature (R) will physically increase the thickness of the lens (d). This is why higher refractive index materials will allow for higher power lenses without increasing the thickness of the lenses. Another way to avoid a thicker lens and get the desired power is to use a Fresnel lens.

Due to the fact refraction is the only reason lens work, the curvature of the interface between the medium (air) and the lens material (glass) is the only functional part of the lens. The thickness of the lens is only due to the physical construction of the lens and does not serve any optical function; therefore, it can be removed. The Fresnel achieves just this by approximating the curvature of the lens in certain zones. This thought process is shown in

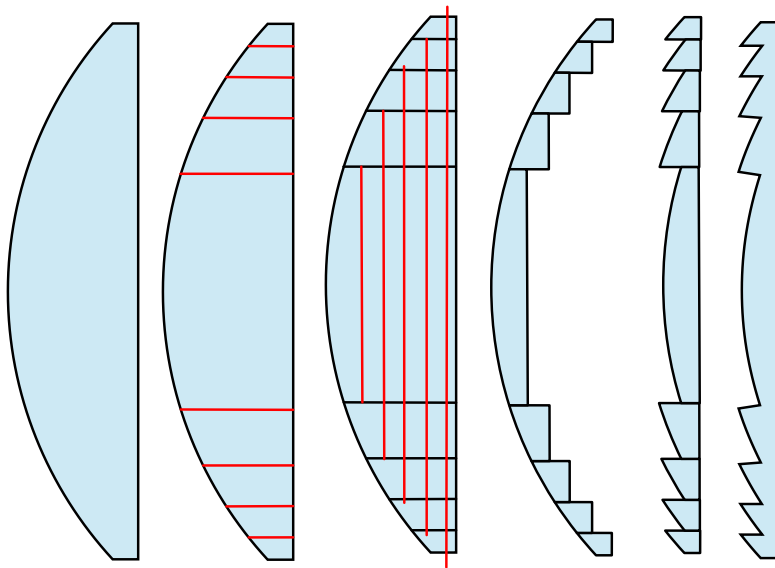


Figure 14.

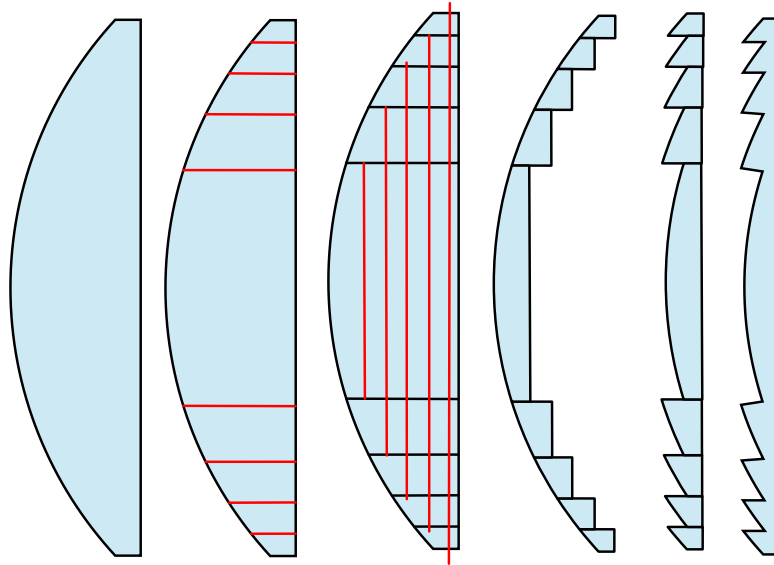


Figure 14 Approximation of a normal lens (first on left) by a Fresnel lens (farthest right).

Because Fresnel lenses can be made thinner, they can also be made larger than normal lenses, which increase the amount of light they can capture, or the aperture. Though it may have the same focal distance, the Fresnel lens does not have as good of image quality as compared to the traditional thick lens. This is due to the discontinuities between the zones, which cause scattering at those points. Despite their decreased image quality, Fresnel lenses are good enough for use in inexpensive portable book-reading aids. Other applications include collimating light sources for lighthouses, automobile lights, projectors, etc. Image quality can be improved by increasing the number of Fresnel zones. In theory, an infinite number of zones would have equivalent image quality as the thick lens structure.

Fresnel lenses are important to use in this application because they can be fabricated in a single layer of PR. The thickness of the PR layer in this research is limited to around 500 nm because of electron

scattering. There are quality concerns, which were mentioned just previously, but when these are made on the nano-scale, they have promise. When the discontinuities become several times less than the wavelength of visible light, then the visual quality will be maintained.

2.3 History

The first IOL implantation was performed on November 29, 1949 in London by Sir Harold Ridley. In his documentation, he only noted “extra-capsular ext.” for extracting the cataract, not implanting the IOL. [28] For 2 years he observed the patient before reporting his case to the Oxford Ophthalmological Congress in July 1951. The work was published in Trans Ophthalmol Soc UK 1951, 71; 617-621, and it is widely accepted as the first IOL implantation performed. [24]

Ridley’s IOL itself was a circular biconvex disc much like the shape of the natural lens with extensions from the optic component, known as haptics, to fix and stabilize it in the eye. It was made of the transparent thermoplastic PMMA, also known as acrylic glass, which was the same basic material used to manufacture cockpit canopies in airplanes of the time period. A large part of the success was due to the impeccable manufacture of the IOL by Rayner & Keeler, Ltd, UK, which is a prominent optical company in the United Kingdom. Some of these original IOLs were in eyes of patients for over 40 years. [28]

Despite being greatly innovative, there were some disadvantages with the early IOLs: AC collapse, glaucoma, uvetis and iris atrophy. The first generation lenses were much heavier due to the PMMA material and had poor fixation to the lens capsule allowed dislocation into the vitreous cavity. In addition, the natural healing process caused clouding over of the lens capsule membrane that held the IOL – a condition known as capsular fibrosis.

In the 1950s, the second generation lens was developed: the anterior chamber lens (ACL), which is shown in Figure 15. As can be deduced from the name, the IOL was placed in the AC instead of the PC, where the first generation IOLs were implanted. The ACL procedure was easier, because the implantation was in front of the iris. Multiple haptics allowed for angle fixation and prevented dislocation and loss into the vitreous cavity. [BU] Even so, there were complications: (1) the rigid haptic structure damaged the adjoining tissue; (2) rotation of undersized IOLs or excessive vaulting caused contact to the cornea, or corneal endothelial, and led to opacification of the cornea, or endothelial corneal dystrophy; (3) oversized IOLs caused chronic pain and inflammation; and (4) in the early 1950s, impurity [BU] and initial poor quality finish of the PMMA led to uvetis, glaucoma, and hypema, known as UGH Syndrome. [21] UGH Syndrome was still a problem into the 1970s due to deformation of lens haptics.

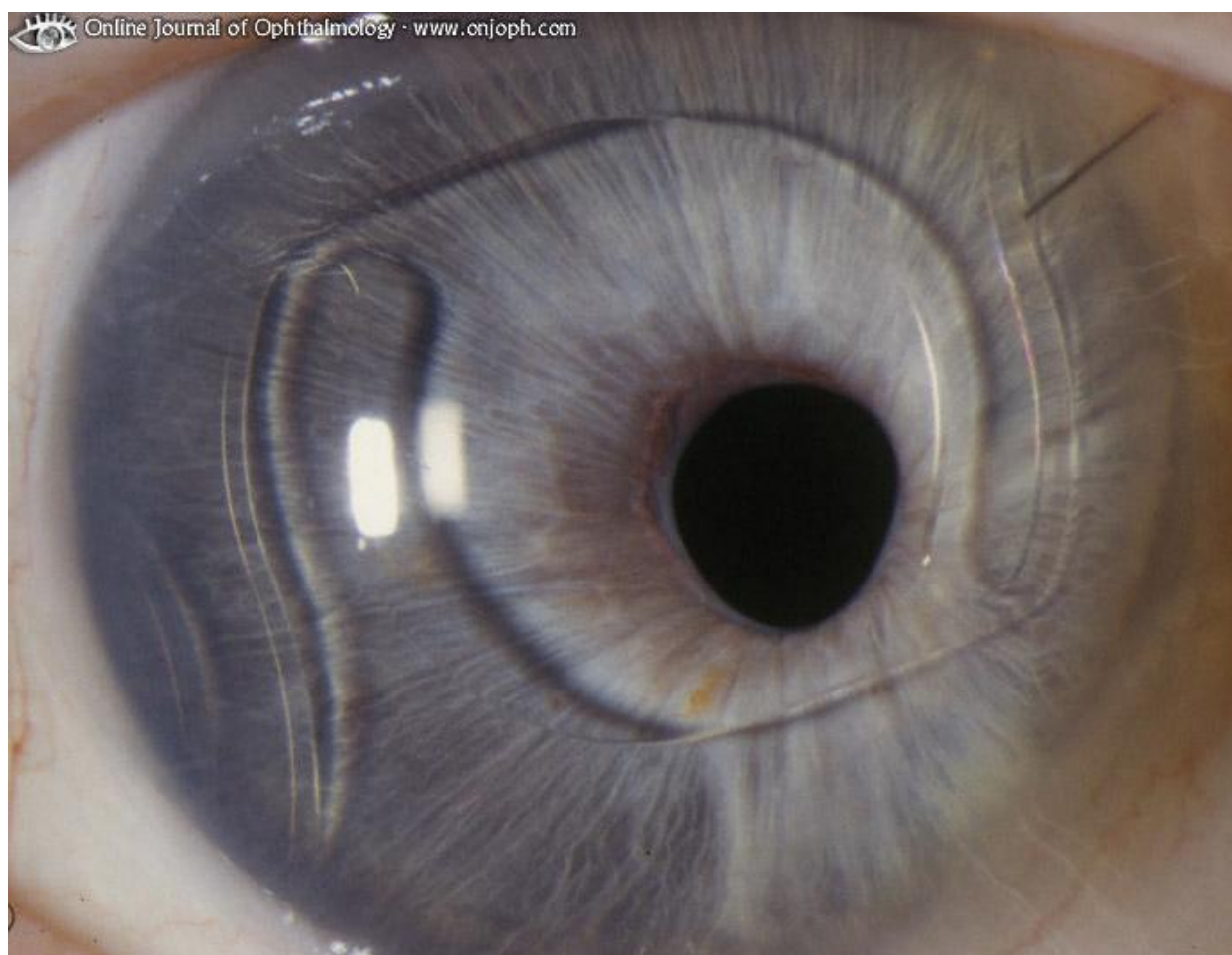


Figure 15 Anterior chamber lens

Copyright Online Journal of Ophthalmology. [<http://onjoph.com>]

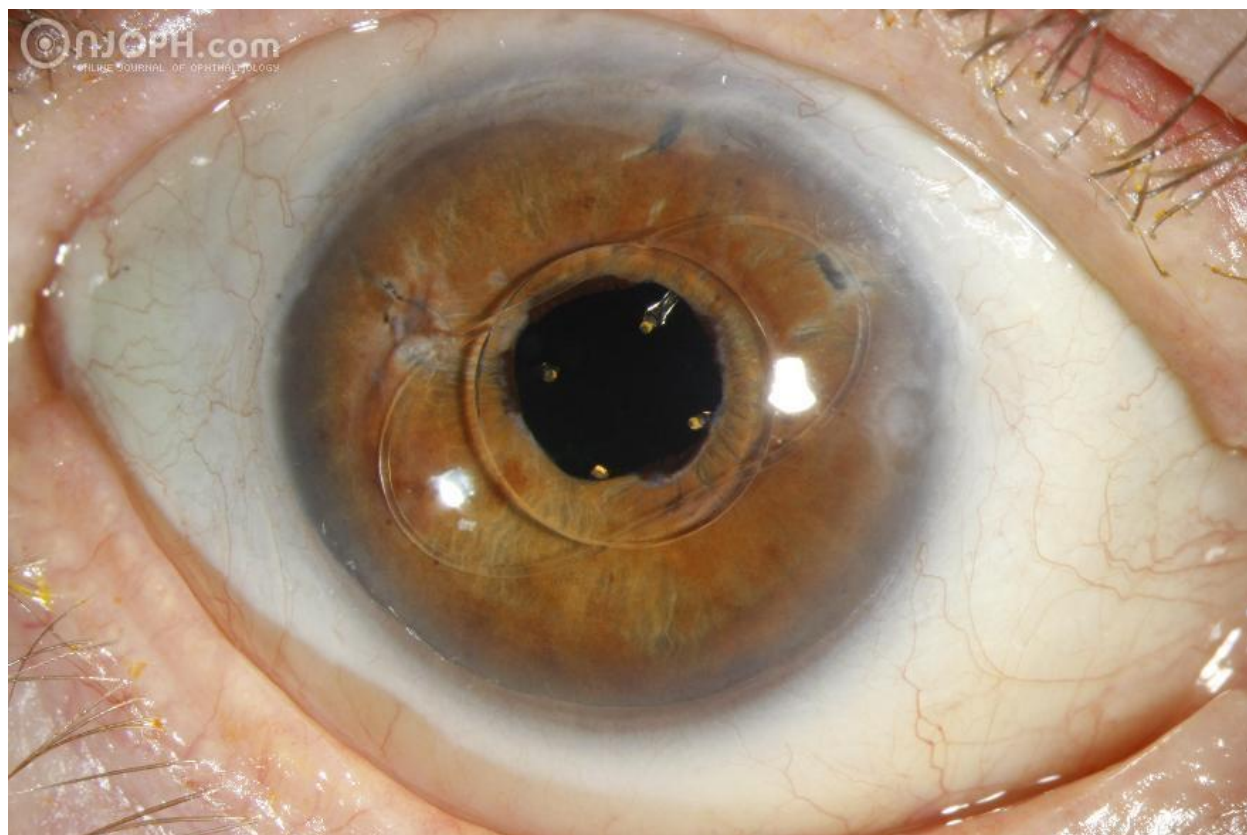


Figure 16 Iris-supported IOL.

Copyright Online Journal of Ophthalmology. [<http://onjoph.com>]

In the late 1950s, the third generation lens was developed: the iris-supported IOL, shown in Figure 16. These IOLs were still implanted in the AC but were affixed to the iris with sutures, metal clips, and haptics through the pupil. The advantage of iris-supported IOLs was that they avoided contact with the cornea and the chamber angle by being fixed to the iris. However, the procedure was complicated by the difficulty placing the lens; and there were still problems with dislocation. Other disadvantages included dehydration of the cornea, or corneal decompensation, and adhesion between the iris and the vitreous causing papillary block. Some of the complications with ACL were further addressed with the fourth generation IOLs: (1) the flexibility of haptics was increased; (2) the polish was improved to decrease irritation; and (3) there were multiple haptic diameters available to improve sizing.

2.4 Modern-Day

IOLs are currently of the fifth generation design [BU]. They are either 1-piece or 3-piece in structure and are considered posterior chamber lenses (PCLs) (shown in Figure 17), because they are placed where the natural lens was originally located. The optical component is made of PMMA, acrylic, silicone, or other innovative viscoelastic materials. In the 3-piece design, the haptics, of which there are two, are either flexible PMMA or polypropylene.

The introduction of continuous circular capsulorhexis (CCC) allows for several fixation options. Small compressible haptics are compatible with either the capsular bag or the sulcus, with or without iris sutures. Normally, the PCL is fixed in the capsular bag, which is the best location, but this requires an intact posterior capsule. It can also be fixed to the sulcus in the case of a large 1-piece PMMA, 3-piece silicone foldable or 3-piece acrylic foldable IOL. Of course, if there is no capsular support, ACLs can still be implanted or you can use iris-fixed IOL that use a McCannel suture instead of an iris claw. However, the PCL has the least amount of tissue damage. The PCL vaults towards the posterior and as such, avoids contact with the iris and prevents pupil capture.



Figure 17 Posterior chamber lens

Copyright Online Journal of Ophthalmology. [<http://onjoph.com>]

2.5 Types

2.5.1 Mono-focal

All of the early IOLs were of the mono-focal type; lenses had only a single focal distance and either provided excellent distance or close-up vision. In 1962, Dr. Warren Reese and Dr. Turgut Hamdi suggested a bifocal IOL, the first of multi-focal type IOLs. The idea was to have an IOL that had sections with different focal distances, specifically 2 in the case of the bifocal lens, that provide focus at far, near and possibly even intermediate distances. These were intended to overcome the lack of accommodation experienced by IOL (pseudophakic) patients. However, it was not until 1980 that Mr. John Pearce, protégé of Ridley's in England, made the early prototype bifocal IOL. [28] The quality of vision was not satisfactory for widespread use. Although there have since been improvements in the design of multi-focal IOLs, even today they have side effects, such as decreased contrast sensitivity, glare disability and halos. [29, 30]

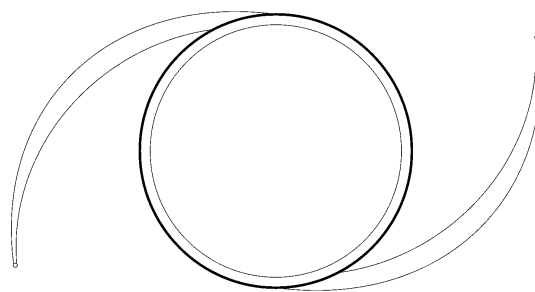


Figure 18 Representation of a mono-focal IOL.

2.5.2 Toric

Even the best fabricated IOLs have some level of positive spherical aberration. This increases the total ocular spherical aberration and degrades visual quality. Astigmatism can be a disabling refractive error. Astigmatism can be natural or caused by surgical trauma. Even though astigmatism post-cataract surgery is minimized through new surgical techniques, at least 15 to 20 % of cataract patients have 1.5 D of astigmatism. [31] Toric IOLs, such as Acri.Comfort 646 TLC IOL (Acri.Tec/Carl Zeiss Meditec), have been reported to be an effective method of reducing astigmatism [32] and are a good solution for patients who desire independence from glasses [33].

2.5.3 Multi-focal

Several companies are now manufacturing multi-focal IOLs. There are 3 types of multi-focal IOLs: multi-zone refractive, diffractive and hybrid refractive-diffractive. [29, 30] Refractive IOLs are based on Fresnel lens and have different powers in zones that are usually in concentric rings that form 2 primary focal points. [28, 30] One example of the refractive IOL is the bifocal Lentis Mplus (Oculentis GmbH). It is a single piece with 2 sectors: the main yielding 2.50 D and a lower one for near vision of 3.00 D. Another example is the Array (Advanced Medical Optics; Santa Ana, CA), and it has five concentric zones that are staggered between distant and near vision. A small study showed that excellent results were achieved. [25] An example of an IOL of the diffractive type is the CreeOn 811 E (AMO, Groningen, the Netherlands) that has wavefront-adjusted optics to improve the quality of vision. Current multi-focal IOLs are of the hybrid type – a combination of refractive-diffractive.

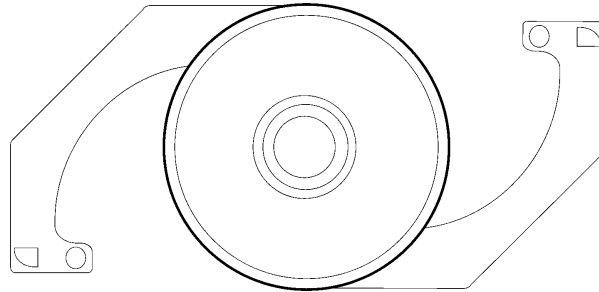


Figure 19 Representation of a multi-focal IOL.

2.5.4 Accommodative IOL

The ultimate goal of an IOL is not to give partial vision and be a mediocre improvement compared to a cataract eye but rather to restore vision and accommodation back to the level of a healthy, natural lens. An accommodative IOL (AccIOL) must be optimized to act much like the natural lens, including the full range of accommodation. For comparison, a healthy, youthful human eye has approximately 12 D of accommodative power, of which the amplitude needed for reading purposes is 3 to 4 D. [34] It is also necessary that AccIOLs have stable accommodation and the same focusing ability for the same amount of muscle force from the ciliary muscles. Also, the flexibility of the lens could compensate for some changes in growth of the eye during development thus providing clear vision without glasses at both near and distance for one's lifetime. [35]

Even with mono-focal IOLs, there might be some apparent accommodation (i.e., pseudo-accommodation) [36] due to the positional movement of the IOL. Multi-focal IOLs may also appear accommodative, but in reality, they only have a fixed set of focal distances defined by physical structures in the IOL. True accommodation requires continuous variance of focal distances. This could be done through axial shifts that move the lens forward and backward (focus-shift) or by changing of the curvature of the IOL with the contraction and relaxation of the ciliary muscles, much like the actual lens does.

As of 2006, AcclIOLs, such as the Model AT-45 crystalens (Eyeonics, Aliso Viejo, CA) and the 1 CU (HumanOptics, Mannheim, Germany), showed potential but had limited and inconsistent accommodation. The 1 CU, for instance, has shown a shift of 0.75 – 2.00 D [37], but more recently less than 0.5 D [36]. Both of these AcclIOLs were designed using the passive focus-shift approach -- i.e., when the ciliary muscles contracted, they moved forward, and when they relaxed, their natural tension restored them. Some focus-shift IOLs contain two optics separated with springs to increase the power during the shift. These dual-element IOLs have been able to reach an accommodation range up to 2.2 D. [38] Active focus-shift IOLs use a driving force, such as repulsing mini-magnets. Currently marketed AcclIOL are passive focus-shift IOL only.

2.6 Future

There is progress with AcclIOLs on the market and in clinical trials that are more and more accommodative, but they have not yet matched that of the natural human lens. There have been several active focus-shift IOLs patented. One [39] includes an annular Fresnel lens constructed of a material, such as PMMA, that changes the index of refraction based on radiant or electrical energy applied. The design involves introducing electrical power via the glasses of the patient. Two other designs [40, 41] are very similar and involve electro-optic crystals that change depending on the applied

voltage field. Another two [42, 43] involve micro-motors that variably adjust a lens system. Despite these solutions being straight-forward conceptually, they are rather complex when put into practice. Motors and related components have to be powered and microprocessors must be able determine the adjustment needed and control the motors. Due to these challenges and lack of technology at the time, the designs have never been physically realized.

One promising design is a fluidic AccIOL that was inspired by the natural human lens. The design involves a support ring surrounded by two chambers that are filled with an optical fluid. The membrane and support ring are constructed of polydimethylsiloxane (PDMS) because of the desired optical/mechanical properties and its biocompatibility. Because of the thickened capsular bag, the optical fluid must have a higher refractive index than the natural crystalline lens in order to achieve the desired amount of accommodation. A total tuning range as large as 200 D was demonstrated. In addition, this AccIOL design was able to achieve 12 D of accommodation in the same amount of movement (0.286 mm) that a focus-shift IOL achieved 2.5 D.

Introduced in 2003 [44], light-adjustable lenses (LAL) developed by Calhoun Vision offer the ability to fine tune the IOL after implantation. The material, which constructs the IOL, is embedded with a photosensitive macromer that polymerizes when exposed to certain forms of light. This allows for precise changes to the lens thickness and shape in order to correct hyperopia, myopia and astigmatism without invasive adjustment. These IOLs are not available in the United States and have been under US Federal Drug Administration (FDA) review since 2009 [45], but they are starting to be available in the European Union (EU). Several studies have found that LALs are safe and some results have shown that the technology gives better than 20/20 vision. Technologies similar to LALs will most likely be used in future AccIOLs in order to precisely tune the vision and make necessary adjustments throughout a patient's life.

There are even methods that attempt to “repair” the lens in place, instead of fully replacing it. In lens refilling, the capsular bag is evacuated and then injected with elastic polymer solutions, such as silicone, silicone oil or poloxamer hydrogel. The pressure of the fluid restores some of the shape of the lens and, due to the flexibility of the injected solutions, the lens is able to change curvatures responding to varying zonular tension. Lens refilling has been tested in pig [46] and primate [34, 47] models.

Studies involving lens filling have been able to achieve a maximum of 6.7 D accommodation; however, there are still limitations with this approach. Even though the refilled lens does accommodate, the amount of accommodation decreases over time and is not stable between 1.0 to 4.5 D [47]. It is also important that there be adequate response to zonular relaxation. In the relaxed state (emmetropia), the focus should be at 20 feet. In order for this technology to be applied in human cases, the level of accommodation also needs to be higher. Lower levels of accommodation are mostly due to the lower refractive index of the injected material. Another challenge is improving the image quality during accommodation. In one study [46], there was increased spherical aberration.

Besides basic problems with accommodation, lens filling has several other unremedied problems. Because silicone has a lower specific gravity than water, it is extremely difficult to use in the filling application. It is difficult to create a silicone gel with viscosity that is low enough for injection and high enough to prevent leakage. Silicone has a long setting time, up to 12 hours, so there is an increased risk of leakage during and immediately following the surgery. [48] One study showed that it was feasible, yet difficult, to use a silicone plug to seal the capsular opening and prevent leakage. [47] In addition, injected silicone also is associated with severe PCO. In all of the related studies referenced here, the lenses were useless after 3 months. [46-49] PCO is caused by leftover lens epithelial cells (LECs) from surgery. The usual treatment for this condition – Nd:YAG laser capsulotomy – can change the

accommodation of the silicone filled lens. There has been mild effectiveness in reducing the development of PCO by treatment with actinomycin D and cycloheximid. [49]

Lens filling may carry the potential to fully restore accommodation, but many improvements have yet to be made. The ideal material has several attributes. First of all, it must be non-toxic because it is being implanted inside the body (in vivo) for long periods of time. Next, it must be transparent and have good optical properties. Third, it must be easily injectable into the lens capsular bag without leaking. It must form a solid yet elastic physical gel inside the capsular bag. Preferably, this would be done rapidly and on demand from an external source. Once the material is hardened, it must have modulus and relaxation times that are constant, so that it will have a stable reaction during accommodation. The material (and procedure) must also prevent PCO; otherwise, the lens filling procedure will be useless. Lastly, it must be inexpensive and sustain functionality. With all of these problems left to answer, IOLs, although not perfect, are still preferred and already offer stable accommodative ability.

2.7 Materials

Material plays a crucial role in quality and performance of IOL design. First of all, the material must be bio-compatible. Second, the material must be of certain quality with the desirable refractive properties. Lastly, the material must also be flexible. Each of these requirements is discussed in further detail below.

Biocompatibility is the ability of a material to maintain mechanical, chemical and structural integrity in order to exhibit safe and effective performance within the body of a living creature. In general, biocompatible materials should not contain impurities, initiators, additives, stabilizers, emulsifiers or coloring-leachables that cause in vivo reactions. The surface characteristics are especially important: smoothness/roughness, wet-ability, charge, polarity, etc. A material's biocompatibility and performance are also dependent on the specific application for which they are used. For example, a material

appropriate for orthopedic surgery could be disastrous in cardiovascular application because of a tendency to create blood clots (thrombogenic properties).

Biocompatibility is difficult to measure, and is determined by comparing laboratory tests with standardized experimental conditions. Adsorption of proteins and other bio-molecules is a major factor in biocompatibility. These can trigger inflammatory responses such as blood clotting, foreign body reactions and fibrous encapsulation. The more biocompatible a material, the less response the host should exhibit and the more favorable the material for applications such as IOLs.

PMMA has a long and proven history of biocompatibility. Ridley noticed the compatibility of the material with the eyes when working with injured pilots whose canopies had shattered. [50] The shards of PMMA were not rejected from their eyes. PMMA is also easy to manipulate and was used in the first IOL. Modern-day PMMA demonstrates even greater biocompatibility because of its higher quality. It can be manufactured in a variety of different molecular weights, and the optical quality of the IOL can be highly variable when mixed with different materials. Each manufacturer has a special formulation for different PMMA compounds. Of all of the materials used for IOLs, PMMA remains the most popular among ophthalmic surgeons. [51]

The need for flexibility was the main reason other materials were considered. Solid PMMA IOLs require that the incision size be as large as the minimum IOL dimension, which is generally 5.5 mm. IOLs composed of flexible polymers, such as hydrophobic acrylics, hydrophilic hydro gels, silicone elastomers and porcine collagen [52], are able to fold and be implanted through much smaller incisions. In addition, zonules and the capsular bag become brittle following the RCS procedure, so there is less muscle force to control the IOL. [38] AccuIOLs must be flexible enough to move under these forces.

Pure PMMA, made of polymerized methyl methacrylate (MMA), is rigid. Foldable IOLs use a variety of materials, such as 2-phenethyl acrylate (PEA), 2-phenethyl methacrylate (PEMA), ethyl acrylate (EA), ethyl methacrylate (EMA), 2,2,2-trifluoroethyl methacrylate (TFEMA), 6-hydroxyhexyl methacrylate (HEXMA), 2-hydroxyethyl methacrylate (HEMA), poly(dimethylsiloxane) (PDMS) and poly(dimethyldipheylsiloxane) (PDMDMS). Some common IOLs are described in Table I.

Table I Common IOL materials

Lens	Material	Refractive index	Water content	Flexibility
PMMA	MMA	1.49	< 1%	Rigid
Alcon Acrylsof	PEA/PEMA	1.55	< 1%	Foldable
Allergan Clariflex	EA/EMA/TFEMA	1.47	< 1%	Foldable
ORC Memory Lens	HEMA/MMA	1.47	20%	Foldable
Storz Hydroview	HEXMA/HEMA	1.47	18%	Foldable
Chiron C10UB	HEMA	1.44	38%	Foldable
Iolab Soflex	PDMS	1.41	< 1%	Foldable
Allergan SI-30NB	PDMDPS	1.43/1.46	< 1%	Foldable

Of special note is PDMS. It is a chemically inert, non-flammable and biocompatible material that is widely used as a biomedical implant material. [53] It has favorable optical properties, such as

transparency above 230 nm and very low auto-fluorescence [54], and has been used for a long time in ophthalmology for IOL. PDMS is also extremely flexible due to its very low Young's modulus. As such, it has become the preferred soft substrate due to its ease of processing. [55]

One major complication that arises with IOLs is opacification. It is caused by calcium phosphate hydroxide granular deposits under the surface of the IOL. Opacification has been linked to local agents, such as viscoelastic devices and the antibiotic mitomycin C; systemic conditions, such as diabetes mellitus, hypertension, ischemic heart disease and uveitis; and even the migration of silicone from the packaging of an IOL. Opacification also happens primarily to IOL made of hydrophilic material. [56] Exchanging opaque IOLs is challenging and can undo the advantages of the otherwise low-impact RCS procedure.

PMMA can be designed with an affinity to water (hydrophilic) or not (hydrophobic), with varying degrees in between. IOLs made from hydrophobic PMMA have more glistening, which effects visual quality, but hydrophilic PMMA has poor PCO performance. Hydration of PMMA to make it hydrophilic may cause opalescence or change the refractive index of the material. In the hydrophilic IOL, visual acuity decreased 9 %, most likely due to the increased opalescence caused by greater water content. Overall, results show that hydrophobic PMMA has better optical quality than hydrophilic PMMA. [51] Silicone has been shown to be statistically superior to PMMA and equal to AcrySof for reducing PCO. [57]

Other material considerations include the index of refraction and its reaction to Nd:YAG. Finer details (higher spatial frequencies) were more viewable with PMMA IOLs as opposed to silicone IOLs. This can be attributed to the higher index of refraction of PMMA compared to silicone as well as the lower convexity that can be achieved by PMMA. [51] However, during Nd:YAG, PMMA with lower polymerization tend to crack and scar more easily than higher polymerization. [24]

2.8 Eye Biometry

Ridley experienced an error of 21 D with his first two implants in 1949 and 1950. Since then, not only have we been striving for better IOLs but also seeking ways to calculate IOL power with greater accuracy. The success of RCS is dependent on several factors: accurate measurement of the eye, use of the best formulas, and introduction of the correct clinical variables.

Biometry of the eye includes measurement of the pupil, axial length (AL), anterior chamber depth (ACD), effective lens position (ELP) and lens thickness (LT). Pupil measurement is important to correct glare, halo and night driving difficulties. In low light, the pupil diameter becomes larger than the functional zones of the IOL and light might be scattered from the cornea. [22] AL should be measured to the nearest hundredth of a millimeter. Errors are significant to around 2.5 D per mm in IOL power, but it can be as much as 3.75 D/mm in short eyes (20 mm). [15, 22] ACD is the distance between the lens and the vertex of the cornea and can account for 20 to 40 % of the total error. [22] Adjusted ACD is known as ELP. It allows physicians to personalize lens position based on their experience with certain types of IOLs. LT tends to be thicker and more optically powerful in hyperopic eyes, older patients and eyes with shorter AL. LT can be measured by immersion ultrasonography. The mean axial thickness of the human lens is 4.62 mm.

The above measurements are used in several calculations that help approximate the refractive power of the optical system. The optical system is a two-lens system composed of the cornea, the lens and the distances between these and the retina. Determination of corneal power, the distance from the lens and the distance to the retina allows the correct IOL power to be calculated. If there are refractive errors after RCS, it is often easier to implant a piggyback IOL in order to correct the residual errors instead of changing out the entire IOL. [25]

2.9 Traditional Fabrication and Cost

IOLs are fabricated much like regular optical lenses and newer ones are even more so like contact lenses. The first step is to reduce the raw material to a manageable size, referred to as a puck or blank. These can either be cut from the bulk material in the case of harder materials or, in the case of softer materials, extruded from the bulk material. The polymer pucks or blanks are available from distributors with consistent and precise dimensions. Companies like Benz Research and Development provide high quality raw materials, such as 2-HEMA, at 99.9% purity for the IOL industry. [58] This purity eliminates the possibility of opacification caused by the appearance of calcium phosphate particles.

The polymer blanks are then milled to the proper curvature. Unlike regular lenses, which are cut down in the lapping process by a crown tool with an industrial diamond [59], IOLs are precisely milled and turned by fully automated machinery. Lathes, like the one pictured in Figure 20, might be used for spherical, aspheric, toric, multi-focal and other irregular cornea fits. [60] Haptics are then drilled for 1-piece IOLs. Otherwise, they can be milled and attached later in 3-piece IOLs. Alternatively, IOLs can also be molded to the right curvature. Some IOLs are even molded on one side and milled on the other. [61]

Next the polishing and hydration steps are performed. Hydration makes the material soft and flexible. Much like contact lens that are milled while a hard material, they becomes flexible after soaking in a balanced pH saline solution for several hours. Most hydrophilic IOLs are tumble polished after hydration. [58] Other solid IOLs may be polished with a fine abrasive. Depending on the manufacture, once the lenses are fully machined and polished, the surface can be coated with chemicals for protection, to increase visual quality or to enhance biocompatibility. Finally, the lens is inspected, labeled and packaged. Current IOLs cost between \$1500 and \$3000. [62]

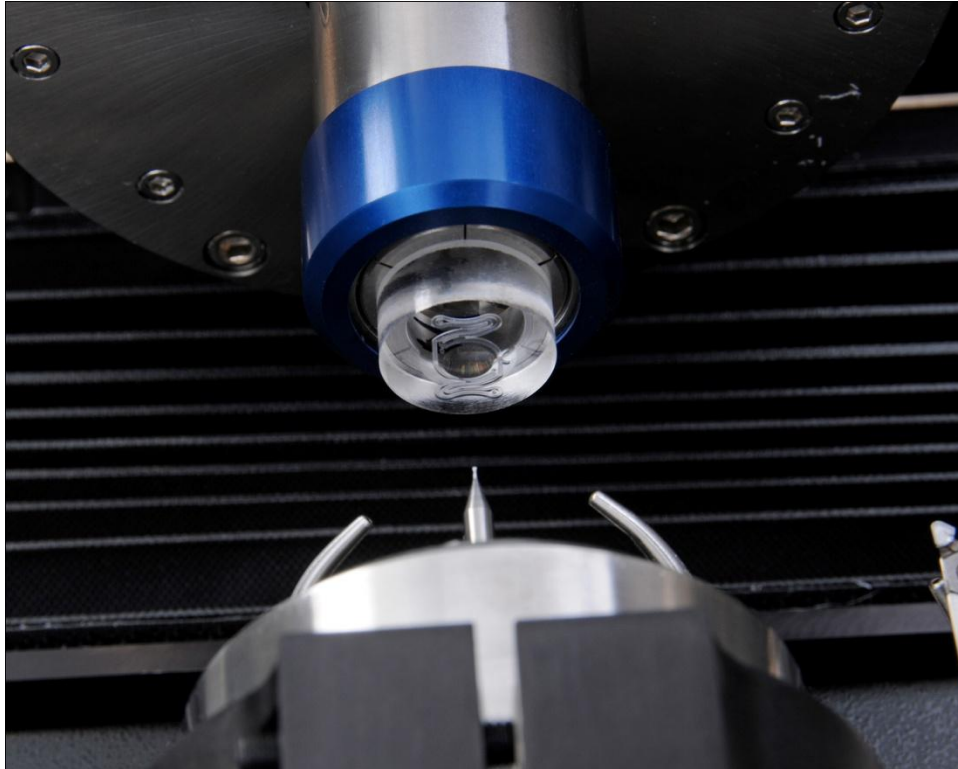


Figure 20 DAC International MLC Mill/Lathe Combination System

Printed with permission from DAC International (<http://www.dac-intl.com>).

3 MICRO- AND NANO-FABRICATION

3.1 Introduction

Micro-fabrication techniques emerged as the result of the increasing complexity and decreasing size of integrated circuits in very large scale integration (VLSI) technology. Although they are normally used in the manufacture of electronics, micro-fabrication processes and techniques have been adapted to mechanical systems since the 1970s [63]. In general, these devices are grouped into the category of micro-electro-mechanical systems (MEMS). Not only does micro-fabrication allow mechanical devices to be fabricated on the same chip as the electricity circuitry to which they are connected, but some devices, such as in micro-fluidics, might not have an electrical connection at all and rely on the mechanics of the device alone. Micro-fabrication has spurred several sub fields in different industries, such as BioMEMS.

There are two approaches to micro-fabrication: bottom-up and top-down. In the bottom-up approach, which is used less widely, the process starts with a blank substrate and the structures are grown or assembled from original “seeds”. A substrate might start at the atomic or molecular level with a seed crystal or single polymer. This is referred to as self-assembly, which is found in the natural world. The bottom-up approach allows for smaller geometries than what is currently available using the top-down approach, but it is limited by the growth rates and therefore, working devices are difficult to mass produce. Currently, many labs are researching the creation of nanodots, nanowires, nanotube transistors, and monolayers using bottom-up approaches. Specific techniques that are commonly used in this approach are molecular beam epitaxy (MBE) and molecular self-assembly.

The top-down approach represents the inverse idea and involves transforming bulk material into smaller devices. The first step is to create the bulk material that is going to be modified. Si wafers are common

substrates and are cut from a large ingot grown from a single Si crystal. Thin films are then deposited on the wafer through processes such as electron beam evaporation or chemical vapor deposition. The thin films are then shaped by either etching or lift off. Photolithography is the process by which patterns are created on the thin films. In photolithography a layer of photo resist (PR), which is a light-sensitive chemical, is spread on the wafer and/or thin film layer. The PR is then exposed to light and treated in a developer solution in order to reveal the pattern.

The PR can be either negative or positive. In positive PR, exposure to light breaks the bonds in the chemical and allows it to be removed in the developer. Negative PR performs in the opposite manner: exposure polymerizes the chemical, making it insolvent in the developer. The developer dissolves and removes the PR in the desired areas and a pattern is formed. The PR can protect portions of the metal from etching, or the PR can be dissolved to lift off the metal in certain sections.

There are two main parameters used to characterize PR: contrast and Critical Modulation Transfer Function (CMTF). Modulation transfer function is simply a measure of dark versus light intensity produced by an exposure system. CMTF is used to define the same quantity for the PR and is roughly the minimum optical transfer function needed to resolve a pattern in the PR. Contrast is an experimentally determined parameter for each PR, and its value is extracted from plots like that shown in Figure 21.

[64]

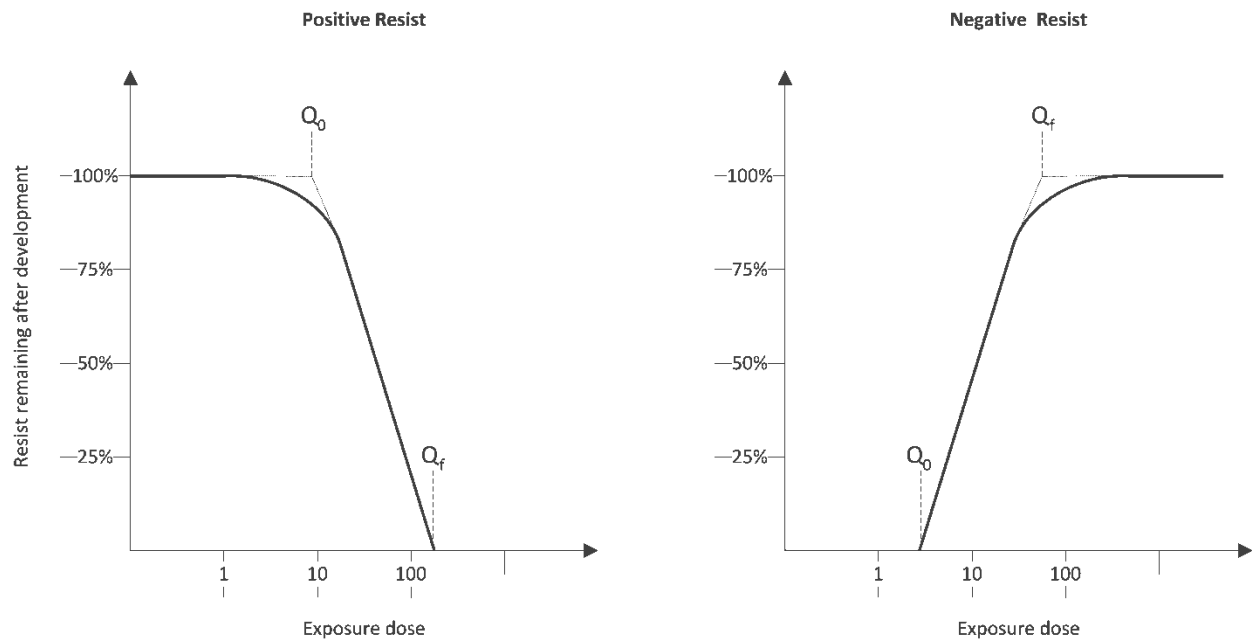


Figure 21 Examples of PR contrast curves

These plots are obtained by using different exposure doses, developing the PR and measuring the thickness that remains. For positive PR, which is shown on the left, less exposure leaves more PR. For negative PR, on the right, the opposite is true: higher exposure levels leave more PR. Contrast is the slope of the transition region in such curves. Mathematically, it is defined as

$$\gamma = \frac{1}{\log_{10} \frac{Q_f}{Q_0}}$$

where Q_0 is the exposure dose that starts the transition and Q_f is where it stops.

Photolithography is the main limitation in micro-fabrication. There are several different forms of photolithography as each one progressively decreases the wavelength of light used. The highest resolution that can be achieved with photolithography is $\lambda/4$, in which the λ is the wavelength of the light used. UV light is the source for the vast majority of photolithography techniques, but it has considerable drawbacks when narrowing down the length scale because it is not possible to reduce the size of the features below the diffraction limit of the UV light. Deep ultra-violet (DUV) decreases the wavelength further. Extreme UV (XUV) can get a resolution of around 11 to 14 nm. [65]

In addition to using different wavelengths of light, there are many other improvements, such as phase shift masks, optical proximity correction (OPC) and high refractive index imaging, which increase the quality of the photolithography and in particular, decrease diffraction effects. Diffraction causes the lines to be softer as they reach the surface, so edges become rounded and less clear. Phase shift masks use destructive interference to minimize diffraction effects. Parts of the masks that interfere with each other have a material added that gives a 90-degree phase shift to the incoming light. Then when the light rays meet, they will cancel and produce an area without light consistent with the intended design. [64] OPC estimates the error caused by diffraction and corrects for it by modifying the pattern structure. Diffraction effects are lessened in immersion lithography by performing lithography in a high refractive index material ($n \approx 1.7$). Both Intel and IBM implement immersion lithography in order to reach smaller resolution. Intel has already pushed the technology to producing 22 nm dimensions. However, all of these corrections and adaptations make the photolithography system more complex and therefore more expensive.

The LIGA (Lithography, Electroplating, and Molding) process is another approach to fabricate advanced 3D structures. In this process, synchrotron generated radiation (X-ray) is used to pattern the photo PR.

The process is capable of creating high aspect ratio structures (30 nm x 5 μm), but access to synchrotron radiation prohibits the widespread usage of the method.

Multi-photon Absorption Polymerization (MAP) is another advanced technique, which is used to create sophisticated 3D structures. The process utilizes a non-linear optical effect created using an ultra fast Titanium Sapphire laser. In this process, the PR is exposed to the laser and, by changing the focusing point inside the polymer, polymerization can be done according to the desired pattern. After developing the PR, un-polymerized areas can be washed away. Laser excitation can generate features with transverse dimensions as small as 80 nm².

Even without the limits of resolution, photolithography is not the best candidate for advanced 3D micro-fabrication. Direct write methods allow you to create structures without the use of masks, which can decrease cost and increase the complexity (layers) in the structures. They also allow for exposure of non-planar substrates. [65] In Scanning Probe Lithography (SPL), scanning probe microscopes (SPMs) have been used to draw lines and construct nano-scale features. [66] SPL methods include Dip Pen Lithography (DPL) and Nano-imprint Lithography (NIL). DPL, which is able to pattern in the sub-100-nm scale, involves depositing an “ink” chemical depending on the application to the substrate via the probe. NIL mechanically imprints patterns and has demonstrated a 25-nm resolution by displacing atoms from the substrate surface.

Heated tips have shown sufficient energy to break chemical bonds of a material and decompose it into volatile monomer units, but this process was slow. Most recently, heated scanning probes have been used to write in PR. Using self-amplified de-polymerization (SAD) polymers, structures were written at less than 2 μs per pixel and resulted in a total write time of 143 s for an image comprising 5×10^5 pixels. The tip was heated to 700 °C and could create 40 nm lateral and 1 nm vertical resolution. In another

study using a similar technique, resolution down to 15 nm and a writing rate of $5 \times 10^4 \mu\text{m}^2/\text{hour}$ was achieved.

These SPL methods can be massively parallelized. Around the world, there are attempts to develop integrations of hundreds and even thousands of tips. Future densities could increase to the millions. Each tip can be either active (lowered and drawing) or passive (raised and inactive). As the head scans the substrate, basic algorithms control the tips mode in order to write the pattern. There have been several improvements to the writing speeds of these devices. [66] Although a writing time on the order of hundreds of seconds is attractive, electron beam lithography (EBL) has the best advantage in resolution.

3.2 Electron Beam Lithography

In EBL an electron beam is used to directly write on the surface of a sample, so it is a direct write method and does not involve masks. In the regular EBL patterning process, an electron beam is scanned across the surface, exposing the PR to enough energy to break the polymer chains throughout the entire thickness of the PR down to the substrate. Even though photolithography has been improved through enhancements such as liquid immersion, phase-shift masks and optical proximity correction, the next-generation lithography technique of EBL offers better resolution. Early on, it was common to convert electron microscopes to EBL using accessories, but more modern, dedicated systems have produced resolutions of less than 10 nm.

An EBL system is rather complex. Figure 22 diagrams an EBL system based on the one used in this project. Each component will be developed in the following sub sections.

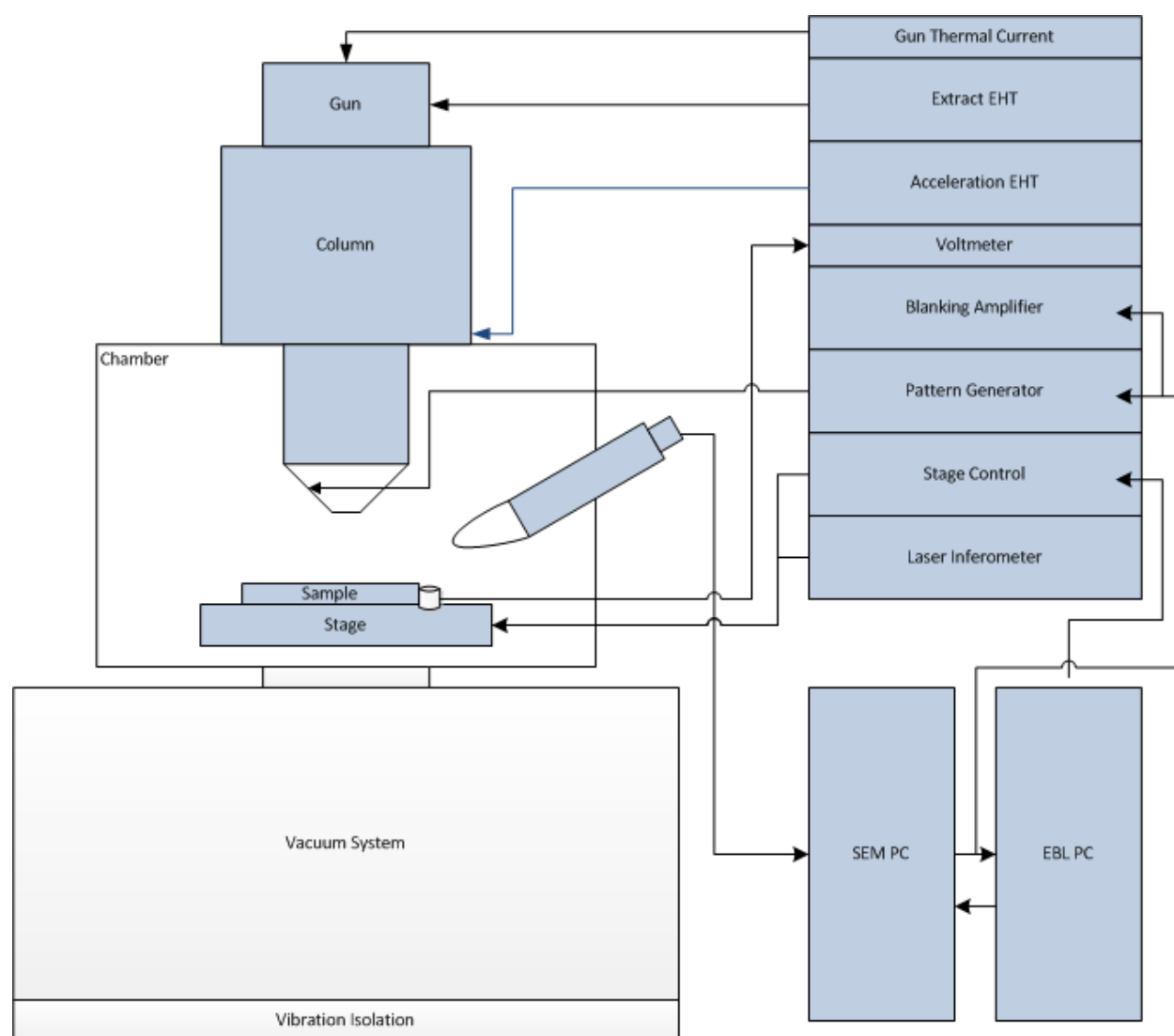


Figure 22 Schematic of a EBL system

3.2.1 Electron Theory

Electrons can either act as a wave or as a particle. This wave-particle duality is routinely encountered in SEM and EBL. In both the photoelectric effect and scattering, electrons behave like particles, but electrons are still affected by diffraction, which is a wave phenomenon. In general, electrons have lower wavelength than UV, deep UV and even XUV light. The wavelength of an electron is calculated by the de Broglie equation.

$$\lambda = \frac{h}{p}$$

Planck's constant (h) is $6.626 \times 10^{-34} \text{ kg}\cdot\text{m}^2/\text{s}$, and p is the momentum of the electron. The momentum of an electron can be related to electron volts (eV), which is the amount of energy that an electron gains in the presence of an electric field of 1 V. For example, electrons in an SEM could be accelerated by 10 kV.

$$p = \frac{\mathcal{E} \cdot e}{c} = \frac{10\,000 \text{ V} \cdot 1.602 \times 10^{-19} \text{ C}}{2.9979 \times 10^8 \text{ m/s}} = 5.344 \times 10^{-24} \text{ kg} \frac{\text{m}}{\text{s}} \rightarrow \lambda = 0.124 \text{ nm}$$

With such a low wavelength, much lower than even XUV (124 nm), the theoretical resolution of EBL is much better than other lithography techniques.

3.2.2 Vacuum Systems

One of the reasons EBL is more expensive than other lithography methods is that it requires the use of vacuum systems. A practical electron gun must operate in a vacuum. An electron is a small particle with a mass of $9.109 \times 10^{-31} \text{ kg}$ and can be thrown off course very easily if it were to encounter, for example, an oxygen molecule of mass of $5.3 \times 10^{-26} \text{ kg}$. There are also electron clouds surrounding each air molecule that would deflect the stream of electrons from the gun. At atmospheric pressure (760 Torr), there are about 2.4811×10^{25} molecules in 1 m^3 . In a typical vacuum of a chamber for EBL with a pressure of 1×10^{-5} Torr, there are 3.260×10^{17} molecules. This is a difference of 8 orders of magnitude,

and makes a significant difference. It is easier to see and more fitting to put it in terms of mean free path (l):

$$l = \frac{RT}{\sqrt{2}\pi d^2 N_A P}$$

where R is the universal gas constant, T is the temperature, d is the diameter of the gas molecule, N_A is Avogadro's number, and P is the pressure. Estimation is done assuming a pure nitrogen (N_2) environment, yet normal air contains 78% N_2 . This estimation also assumes the electron to be the same size as every other gas molecule. At atmosphere, the mean path is only around 0.1 nm (10^{-7} m). At the high vacuum level (10^{-5}), it is estimated around 7 m. [67] This difference is substantial, and allows for the vast majority of electrons to make it through the electron gun unobstructed. Vacuum in the electron gun itself may be under 10^{-7} , which further increases the benefits.

Vacuum plays another role. Due to the high potentials used in the electron gun, there needs to be an insulating medium (such as vacuum) to prevent arcing. The electrical breakdown of air is about 3 kV/mm. [68] In high vacuum, it can be raised 10 times to 30 kV/mm. [69] This is more important in higher power (potential) equipment.

With vacuum chambers and systems, comes bake-out. This is a maintenance step where the chamber is put under vacuum and heated. The walls of the chamber heat to help vaporize materials and release gases that remain in the system. For this bake-out procedure to work, all equipment inside the chamber needs to be compatible with the temperatures used in the process.

For the levels and ranges required, multiple stage vacuum systems are necessary. Multiple stages are used because of the different efficiencies of specific vacuum pumps. This is often the case with other fabrication equipment that require vacuum chambers such as e-beam deposition, reactive ion etching (RIE) and chemical vapor deposition (CVD) tools. For example, roughing pumps, which are usually piston

type, are used to pump down to 10^{-3} Torr, and pumps such as turbo-molecular ones are used to pump down to higher vacuum: 10^{-5} - 10^{-7} .

3.2.3 Electron Sources

The electron gun in an EBL or SEM system needs to have a source of electrons. Electron emission involves giving enough energy to an electron so that it can overcome the binding potential, or work function, and escape from the surface of a material. An example of an energy band diagram for a material, such as a metal, is represented in Figure 23. The area below E_v is the valence band, where most of the electrons are in a material. The conduction band at energy E_c is the place electrons conduct in a material. The Fermi energy level, E_f , is the level at which 50% of the electrons will be found. The vacuum level, or free energy state, is that above E_0 . At this energy level, the electron is no longer bound by the material. The work function is the energy needed to reach that level. Electron sources must provide a simple and consistent source of these electrons. These can be either thermionic or field emission sources.

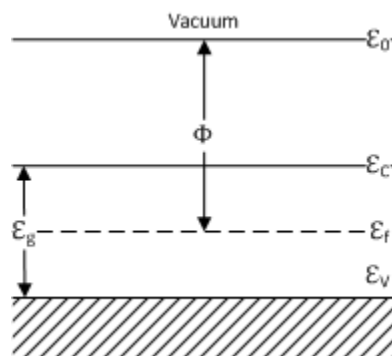


Figure 23 Generic electron band diagram

Thermionic emission involves introducing enough energy to electrons through heat. Electrons have an energy related to temperature by the Boltzmann constant ($k = 8.617398 \times 10^{-5} \text{ eV/K}$).

$$E = kT$$

Temperature (T) is in Kelvin (K). For example, at 2700 K, electrons will have energies of about 0.23 eV.
[70]

Early on, a thermionic source could simply be a thin (0.1 mm) wire of tungsten (W). Tungsten can operate at very high temperatures without melting or evaporating. Current is run through the wire and it heats up much like a filament in a light bulb. Running this process in a vacuum helps in multiple ways. It allows the element to heat up with less energy, because there are fewer molecules to allow for heat dissipation, and less air molecules to prevent the filament from oxidizing. This is also why a light bulb is a vacuum. Thermionic sources are quite simple in construction and are used on various equipment such as electron beam evaporation systems.

The amount of electrons emitted from a thermionic source, known as emission flux, can be expressed by the Richardson-Dushman equation:

$$J = AT^2 e^{-\frac{\Phi}{kT}}$$

where A is a material and J is the current density emitted. For tungsten, A equals $60 \text{ A/cm}^2\text{K}^2$ and the work function (Φ) is 4.5 eV. From this equation, theory shows that electron current will increase exponentially with temperature. For tungsten, this relationship is true from 2500 K to when it melts at 3100 K. Current is increased until the emission of electrons saturates. Higher temperatures do provide more electrons, but they also sacrifice filament lifetime. At 3 to 4 A, tungsten runs at 2500 to 2700 K.
[70]

The size of emission is important because it has an effect on the overall beam size. Finer focused emission needs less area for condensing lenses, maintains a higher current density, and ultimately requires less demagnification by the column. Narrower light will also result in less energy spread, which is comparable to monochromatic light. Because of this size requirement, the shape of the source is important. Newer thermionic sources use a crystal of lanthanum hexaboride (LaB_6). The tip shape then directs emission to a narrow column. The material, also known as only lanthanum boride (LaB), is a ceramic material that has a very low work function that allows it to have one of the highest electron emissivities.

A Wehnelt cup helps collect electrons that are emitted from the electron source. The cup encompasses the source. It is kept at a negative potential around -300 V in order to confine electrons. A small hole at the bottom of the cup allows for the electrons to be pulled toward the anode part of the electron gun.

Field emission (FE) sources involve using an electric field that is sufficiently strong to tunnel electrons through the barrier. The sources are usually tungsten tips sharpened to a needle point. Tungsten can also be shaped to very sharp points – possibly the tip of a single atom. The sharp point allows for a higher field to be active, which increases electron emission and allows for tighter control of the emission location. The cathode of the source, comparative to the Wehnelt cup, is referred to as the suppressor. The anode is simply the extractor.

Cold FE sources only use the voltage as an extraction force. These sources are used primarily in electron microscopes rather than EBL because of their instability, including long term drift. Newer equipment uses Mueller-emitter-based sources that are a combination of both types. These are known as thermal field emission (TFE) sources. These operate at high temperature and employ an extraction voltage. Heated sources are more stable because they drive off gases that might interfere with a cold source and

can be stable for months at a time. [FD] Often TFE sources are tungsten tips coated with zirconium dioxide, which lowers the work function of the material. Table II compares several electron sources.

Table II Various electron sources and their parameters

Type	Brightness (A/cm ² /sr)	Size (nm)	Energy Spread (eV)	Vacuum required (Torr)
Thermionic – W	$\sim 10^5$	2500	2-3	10^{-5}
Thermionic – LaB ₆	$\sim 10^6$	1000	2-3	10^{-8}
TFE	$\sim 10^8$	20	0.9	10^{-9}
FE	$\sim 10^9$	5	0.22	10^{-10}

[71]

There are other electron sources being researched, such as carbon nano-tubes (CNTs). These sources offer the possibility of thermionic and photoemission. For thermionic emission, single- and multi-walled CNTs intercalated with potassium, a temperature-independent work function below 600 K with a minimum of 2.0 eV has been observed. Also, Nd:YAG lasers can be used to illuminate the same CNTs causing an increase in electron energy distribution. [72] High brightness has been found in multi-walled CNTs [73], and they may prove to be a future replacement for electron sources.

3.2.4 Acceleration Potential

Once you have electrons emanating from the source, they need to be accelerated down the column towards the substrate. This is done by extra-high tension (EHT) through the electron gun: the source is the cathode, and at the end is the aperture, which is the anode. EHT can range from 0 to 100 kV in EBL and even 200 kV in tunneling electron microscopes (TEM). Higher energy electrons allow for examination of a thicker sample, but they might also cause damage to the sample. Not only does higher energy pierce deep into the PR and substrate, but the beam diameter also decreases. The EHT should not only be high voltage, but it must also be stable. Any change in the acceleration potential changes the energy with which the electron hits the substrate.

3.2.5 Beam Blanker

In lithography, the pattern being written is not always made up of continuous lines. In order to accommodate this, the beam must be stopped and started. Both the electron source and the acceleration voltage cannot be cycled off quickly. Instead, it is easier to turn the beam off and on by deflecting it from the substrate. This can be accomplished by a simple electrostatic deflector, which is a pair of plates. A blanking amplifier with fast response time is connected to the plates. When the plates are energized, the beam is deflected off its perpendicular path down the column. If the blanker is not positioned close to a focal point of the beam, streaks can occur on the sample when the beam is deflected off axis. Higher energy systems might require elaborate blanking systems with multiple plates and delay lines in order to prevent motion of the beam during the blanking process. [71]

3.2.6 Lenses

The Wehnelt cup and the acceleration potential help to confine the beam and provide a coarse amount of focusing. However, the stream of electron emission is still quite divergent and requires further focusing by lenses. The goal of the lenses is to condense the electron emission into a relatively parallel,

or collimated, beam. In principle, lenses in electron columns behave the same as lenses in optical systems. To understand lenses in an electron column, electron trajectories can be considered like light rays, and the ideas of converging and focal points are the same.

Though electron lenses might be similar to optical lenses, the quality of focusing in terms of aberrations is not nearly as good as with optical lenses. Spherical and chromatic aberrations are two types that are critical to EBL. Spherical aberrations are caused by a difference in power between the inner and outer areas of the lens. Chromatic aberrations occur because electrons of different energies (i.e., wavelengths/color) are focused to different points. There is currently no mechanism to correct for chromatic aberrations, so narrow dispersions of the electron beam from the source are needed. Both of these aberrations can be minimized by confining the electrons to the center of the lenses, but this greatly reduces beam current by limiting electrons.

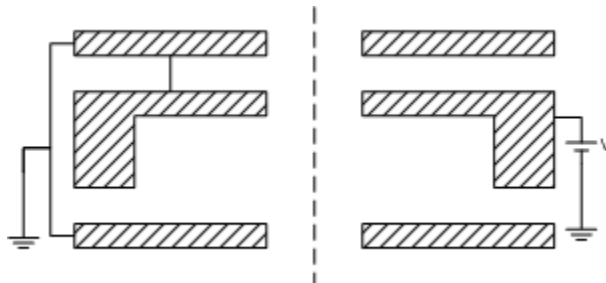


Figure 24 Cross-section of an Einzel electrostatic lens.

Lenses in electron columns can either use electrostatic or magnetic forces. Electrostatic lenses are not used for fine focusing, because they cause more serious aberrations than magnetic ones. When they are used, however, they are often found at the beginning of the gun region because they can be combined with the extractor anode. A simple electrostatic lens, known as an Einzel lens, is diagramed in Figure 24. In the Einzel lens, there are 3 apertures in series. The outer two have no potential (i.e., they are grounded), and the inner one has a voltage that can be varied. The focusing comes from drawing electrons back to the center of the column with positive potential. Lens power is controlled by changing the voltage.

A magnetic field can be used to bend electrons inward and converge them to a focal point. This force is represented by the law of magnetic (Lorentz) force:

$$\vec{F} = q(\vec{v} \times \vec{B})$$

where q is the charge of an electron, \vec{v} is the velocity vector of the electron and \vec{B} is the magnetic field from the lens. The power of a magnetic lens, shown in Figure 25, can be created using electromagnets. Electromagnets are coils of wire, usually copper, encased in a highly permeable material, such as iron, to concentrate the magnetic field. An opening in the casing focuses the field toward the center of the column.

Multiple lenses may be used to further increase the focus of the beam. The purpose of first condenser lens is to collect the electrons from the source. The second lens converges the beam at the specimen. The sharper the focus of the beam, the fewer electrons are intercepted by the apertures, which results in higher beam current.

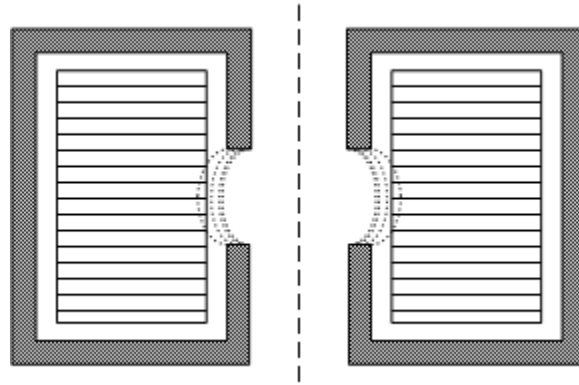


Figure 25 Cross-section of an electro-magnetic lens.

3.2.7 Stigmators

Because the construction and operation of the lenses are not perfect, there will be errors in the circular beam shape. Astigmatism is an elliptical distortion of the beam caused by differences around the circumference of the lenses. Stigmators are special lenses that are used to compensate for these imperfections by adjusting X and Y directions independently. Like lenses, stigmators can be either electrostatic or magnetic. They may have 4 or more poles (8 is typical) arranged around the optical axis. [FD] There may even be two stigmators to make the beam its optimum shape.

3.2.8 Apertures

The main purpose of the aperture is to filter out electrons that were not tightly focused into the beam. This ensures that the electrons are normally incident to the sample. The aperture also intercepts the

beam when it is deflected and is used to shape the beam. Earlier beams were Gaussian in shape, but to create continuous patterns, it is useful to force the beam into a shape such as a square. Creating an area of known exposure dose makes patterning more continuous. The areas can then be treated as pixels and exposed individually to create patterns. Overall, different sized apertures vary the beam current.

3.2.9 Scanning

Once the beam is formed, it must be scanned across the surface of the sample in order to render an image in an SEM or write an image in an EBL. This is done by deflecting the beam to different parts of the sample. One scanner, or deflector, tilts the beam towards another part of the sample. Alone, this would introduce an angle between the beam and the sample. As such, translating is done with 2 deflectors: one to tilt the beam to a new position, and the second to correct it back to being perpendicular to the sample. Deflecting the beam causes aberrations and enlarges the beam diameter. The maximum extent of the deflectors creates the area known as the write-field.

Like lenses, beam deflectors can be either electrostatic plates or magnetic coils. Again, electromagnetic coils provide fewer distortions than the electrostatic ones; however, electrostatic deflection can perform at much higher speeds. Electromagnetic coils cannot respond to the higher frequencies of charging and discharging. A compromise between both electrostatic and magnetic is used in some systems: magnetic deflectors are used for long-range deflection and electrostatic deflectors are used for short-range and high-speed. Deflection systems are frequently placed inside the final lens; therefore, ferrite is used to cover the final lens to minimize field interactions from the scanners.

3.2.10 Stitching

Beam translation only allows for a certain size of write-field that is determined by the range of deflection and the acceptance of aberrations and distortion. In order to write patterns larger than the write-field, the sample and the stage on which it sits must be moved. When this process is used to

continue a pattern, it is called stitching. Stage movement is done through 2 different methods. Coarse movement is done using servomechanisms (servos), while fine movement is done using piezoelectric motors (piezo-motors). Servos are electric motors that involve error-feedback via encoders to allow for precise position control. Due to the mechanical nature of the servos, they are not accurate enough to move the stage alone. Piezo-motors rely on the change in shape of materials when voltage is applied. The deformation of these piezoelectric materials is precisely known and allows for very fine movements. Confirmation of the movement is done on both axis (X and Y) by an interferometer. An interferometer involves using a laser to measure the distance traveled in both directions. Laser interferometers are highly accurate and allow for stitching errors to be in the range of single nanometers.

3.2.11 Substrates

There may be some limitation on what substrates are compatible with EBL. Electrons, being charged particles, tend to charge substrates negatively, unless they can quickly gain a path to ground. If they are not dissipated quickly enough or become trapped, the substrate becomes charged. When a substrate is charged, it will deflect further electrons. This is known as charging effect and will disrupt further exposure of the substrate. The charging effect creates the same limitation in SEM imaging that requires non-conductive samples to be coated with metal.

Especially in high-energy EBL, it is important to have paths assisting the electrons to ground. On Si wafers virtually all electrons stop at the wafer where they can follow a path to ground; however, masks, which are made of insulating materials such as quartz, often have embedded electrons that will take much longer to move to ground. For low energy exposures, negative charge can be controlled by adding a conductive layer to insulating surfaces. For high energy exposures (> 10 keV), electrons can pass through the PR and conductive compensation layers and end up in the substrate.

3.2.12 Photo resists

SU-8 is an epoxy-based, negative UV-PR originally developed by IBM. It has shown continued use in lithography from photolithography to X-ray lithography before being used in EBL. Due to its capability for high-aspect ratio structures as a result of a low absorption coefficient at wavelengths above 360 nm, it has been widely used in MEMS fabrication [AM]. SU-8 is chemically amplified and exposure creates an acid that initiates cross-linking. The post-exposure bake is very critical and provides the thermal energy needed to complete the polymerization of SU-8 monomers. Overall, SU-8 seems to be the most popular PR used according to several articles, such as [74]. SU-8 is developed in a propylene Glycol Methyl Ether Acetate (PGMEA) bath. [75] It is also durable and resistant to most chemicals and solvents, which can be beneficial in processing.

PMMA is plastic that can act as a negative PR for EBL. Although it requires a larger exposure (50-500 $\mu\text{C}/\text{cm}^2$) dose than SU-8 (3 $\mu\text{C}/\text{cm}^2$) [76], PMMA has a higher resolution [77]. It is a transparent PR that lends itself to being used for optical devices. It is also easy to apply and develop. PMMA avoids charging during EBL and exposes well. PMMA has demonstrated a 20 nm resolution [78], while another popular PR, ZEP-520, has only demonstrated 60 nm [79]. If PMMA is used on insulating substrates, a thin coating of metal, such as aluminum, chrome or copper, may be used to help dissipate the charge accumulation. [80]

Chalcogenide glass (ChG) can be used by multiple sources: UV, X-ray, and e-beam. ChG offers many benefits over polymer PRs, especially for optical device fabrication because it is transparent in the visible and infrared regions of light. This proves important to the device considered in this paper. For EBL, ChG exhibits near linear height dependence with electron irradiation dose. This makes it clearer to create images from an actual structure and no correction is needed. Additional simplicity comes with the elimination of pre- and post- bake procedures that are required by polymer-based PR.

Hydrogen silsequioxane (HSQ) has been shown to be an excellent tone PR in high resolution, high aspect ratio EBL. It has been demonstrated in multiple-step 100 keV EBL that lateral dimensions down to 30 nm in thickness up to 1 μm was possible. In these experiments, silicon nitride (Si_3N_4) was used because of the optical characteristics of X-ray lenses to reduce photon beam absorption. Also, it allowed for the use of high energy EBL by sparing proximity correction. There is negligible backscattering in the thin nitride membrane.

3.2.13 Resolution

The diameter of the beam changes along its path through the column. First, there is the size of the virtual source

$$d_v = \frac{1}{\pi} \sqrt{\frac{i}{\beta}}$$

where i is the beam current and β is the brightness of the beam. [81] The virtual source is then multiplied by the magnification of the column (M) resulting in the diameter of the beam leaving the gun.

$$d_g = d_v M = \frac{1}{\pi} \sqrt{\frac{i}{\beta}} \frac{2}{\alpha}$$

The convergence angle is represented by α . Apertures are used to limit convergence angles. Second, because the lenses of the system are not perfect, the diameter caused by spherical aberration needs to be taken into account. It can be calculated as

$$d_s = \frac{1}{2} C_s \alpha^3$$

where C_s is the spherical aberration coefficient. Third, there are also chromatic aberrations from the column lenses. Different energies of electrons result in different wavelengths. At present,

electromagnetic lenses cannot adjust for this. The diameter due to these aberrations can be calculated as

$$d_c = C_c \alpha \frac{DV}{V_b}$$

where C_c is the chromatic coefficient, DV is the energy spread of the electrons and V_b is the beam voltage. Last, as mentioned before, electrons are affected by diffraction. Diameter due to the diffraction at the apertures is calculated as

$$d_d = 0.6 \frac{\lambda}{\alpha}$$

where λ is the wavelength of the electrons.

$$\lambda = \frac{1.22}{\sqrt{V_b}}$$

The total beam diameter is shown to be a combination of these effects:

$$d_t = \sqrt{d_g^2 + d_s^2 + d_d^2} [71]$$

The effect is graphed in Figure 26. The beam diameter of standard EBL systems ranges in the single nm levels. State-of-the-art SEM can produce beams of 10 to 100 Angstroms in width. [82] Although beam diameter is critical in resolution, there are other effects, such as the proximity effect, that limit it.

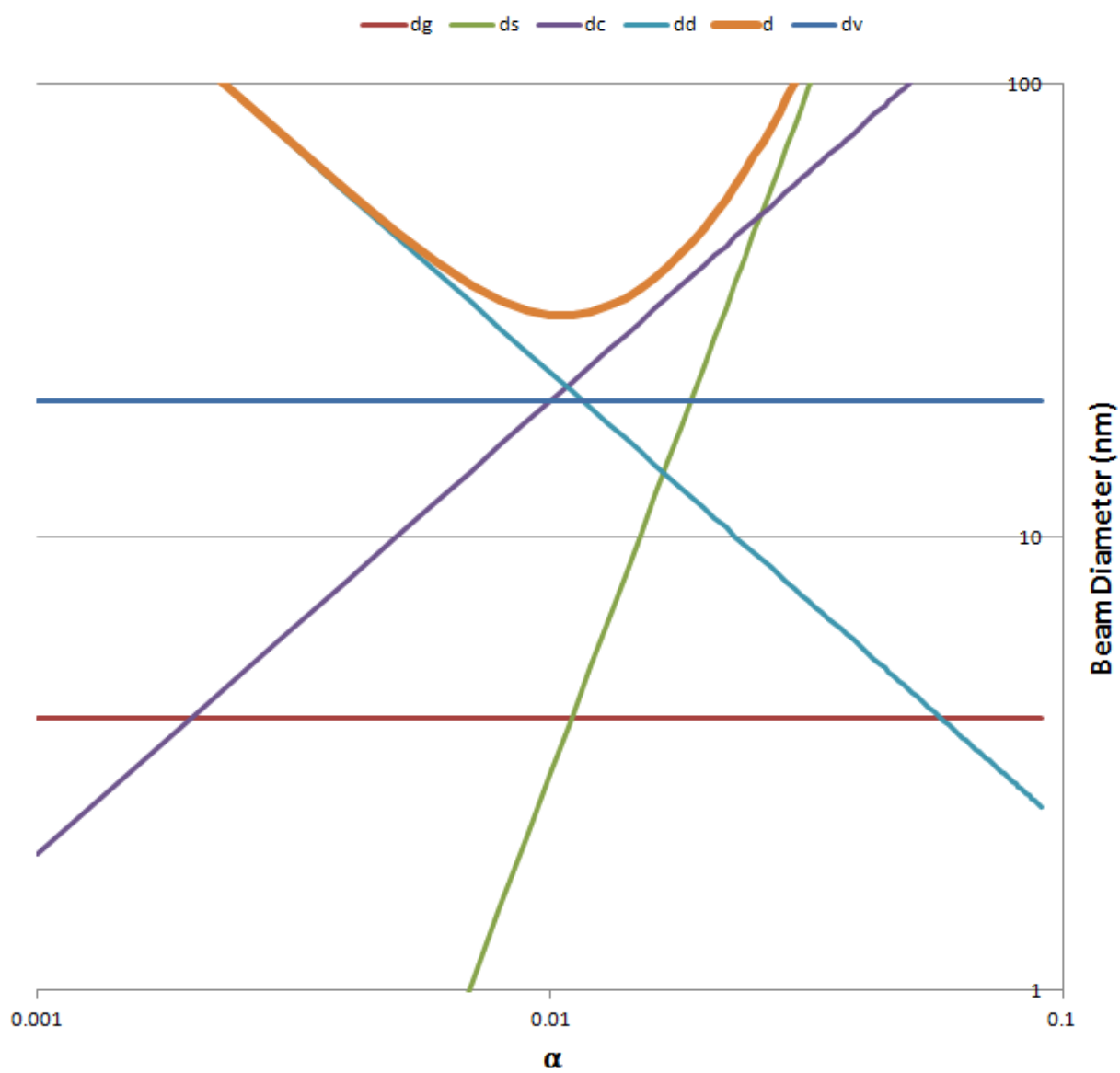


Figure 26 Beam diameter vs. convergence angle

3.2.14 Scattering and Proximity Effect

The path of the electrons is not perfect. Though they are largely unaffected by interactions while traversing down the column, when electrons hit the solid PR layer, the story is different. Upon impact, the electrons experience a larger frequency of scattering events due to the interactions with the dense molecules in the PR. Scattering is a particle interaction and can be either forward or back scattering.

Forward scattering is a small angle interaction in which the majority of the electron trajectory maintains its continued forward movement into the PR. These small angle scattering events are due to the inelastic collisions or deflection by electrons in the PR. Overall, forward scattering results in a widening of the effective beam diameter in the PR. The increase in diameter is given by

$$d_i = 0.9 \left(\frac{R_t}{V_b} \right)^{1.5}$$

where R_t is the PR thickness and V_b is the beam voltage in kilovolts. [71] From the equation, it can be seen that using higher acceleration voltage and thinner PR results in less beam diameter increase.

Backscattering is a large angle scattering event, which results in the electron reflecting backwards through the PR. The returning electrons cause additional exposure around the incident beam. This is called the proximity effect. The additional exposure results in errors in the surrounding profile. The amount of electrons that are backscattered is mostly independent of beam energy; however, the spread is increased by it. The substrate material has the greatest effect on the amount of backscattering. Low atomic number materials give less backscatter. For example, typical ratios of backscatter in Si is 0.17 and 0.50 for tungsten and gold. [71] Electron acceleration voltage is a key parameter to control forward and back scattering. Increasing the acceleration voltage intensifies the back scattering, while simultaneously inhibiting the forward scattering and vice versa. Monte Carlo simulations show the combination of both forward and backscattering, for example in Figure 27.

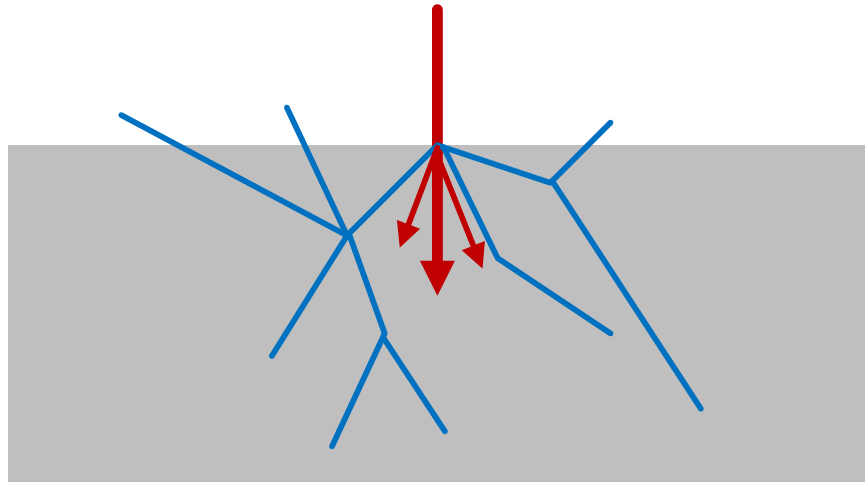


Figure 27 Example of forward and back scattering

3.2.15 Environment

Overall, EBL systems are precise yet sensitive equipment. The systems should be installed in clean environments to minimize contamination of the samples, chamber, optics and vacuum systems. Temperature and humidity should be well controlled, preferably to a tenth of a degree [71]. Any fluctuation can adjust the physical size and thickness of many pieces of the equipment. Vibration isolation is usually recommended. The environment should also be electrically and magnetically quiet. Noise from transformers, power panels, and stray magnetic fields can have an unwanted effect on the

entire system and ultimately the electron path. Commonly, great care is needed on the analog and digital grounds to minimize high frequency noise from entering the system.

3.3 Gray-scale Lithography

Normal, or binary, lithography involves, in theory, either complete exposure of the PR down to the substrate or no exposure at all. This creates a binary profile composed of substrate level and the PR level, as shown in Figure 28.

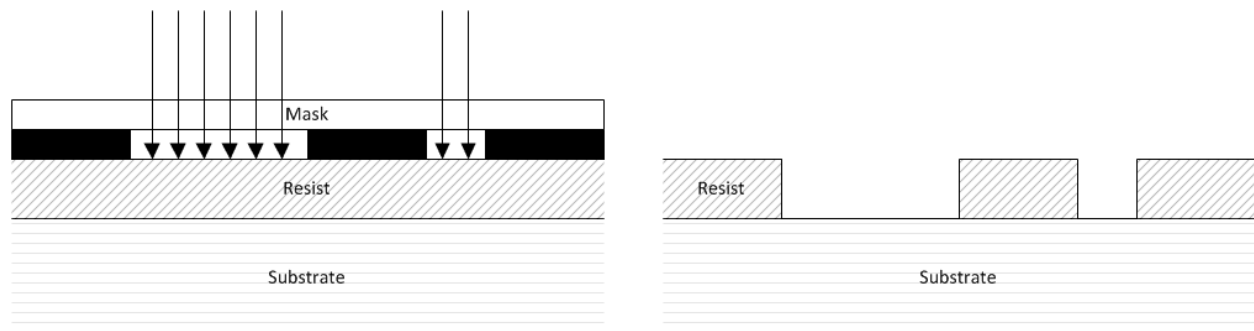


Figure 28 Binary lithography exposure via mask and resulting PR profile.

To achieve this, there must be a sharp difference between light and dark areas. This is where diffraction becomes a problem. Diffraction spreads the light out, so by the time it hits the PR, there may be less distinction between dark and light areas. If the defraction is too great, you will have incomplete exposure. To help compensate for this, PRs with higher contrasts are used. Ideally, the contrast curve of

a PR used in binary lithography would be a step function; there would be an immediate cut off between the energy needed for complete development and the amount needed for no development, or infinite contrast. This is diagramed in Figure 29.

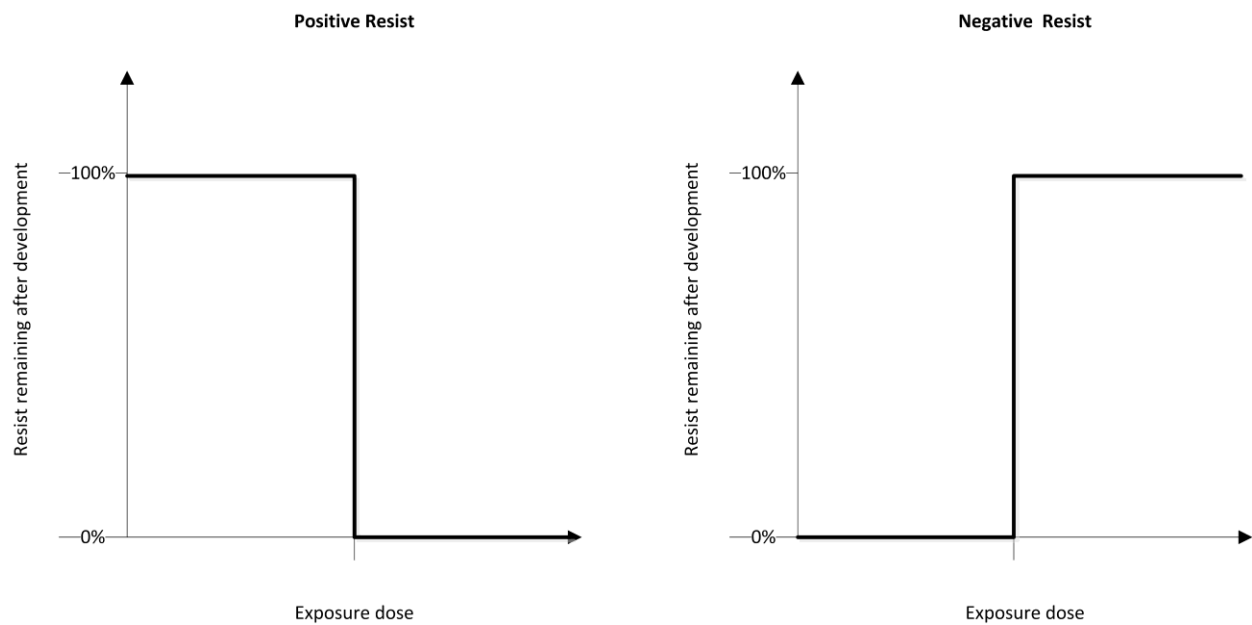


Figure 29 Idealized PR contrast curve.

Exposure dose is given by

$$E = I_0 t$$

where I_0 is the electromagnetic flux (mW/cm^2) present at the surface of the PR and t is the time in seconds. The amount of energy absorbed at a depth z in the PR is

$$W(z) = \alpha I(z)t$$

where α is the absorption coefficient (cm^{-1}) and the electromagnetic intensity

$$I(z) = (1 - R)I_0 e^{-\alpha z}$$

where R is the reflectivity of the PR. Together the equations give

$$W(z) = \alpha(1 - R)I_0 t e^{-\alpha z}$$

which is graphically represented in Figure 30.

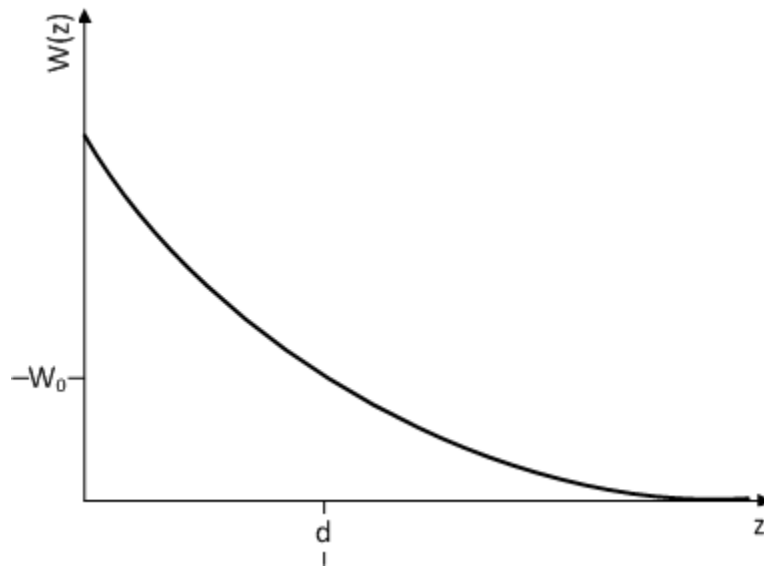


Figure 30 Energy absorbed at depth z .

PR at z will clear where $W(z) > W_0$, so the maximum depth that will clear is d . Using d in the W function will then provide the direct relation between energy input and the cleared depth.

$$W(d) = W_0 = \alpha(1 - R)I_0 t e^{-\alpha z}$$

$$d = -\frac{1}{\alpha} \ln \left(\frac{W_0}{\alpha} (1 - R) I_0 t \right) = \frac{1}{\alpha} \left[\ln \left(\frac{\alpha(1 - R)}{W_0} \right) + \ln(I_0 t) \right]$$

$$d = A + B \log E$$

$$A = \frac{1}{\alpha} \ln \left(\frac{\alpha(1 - R)}{W_0} \right)$$

$$B = \frac{2.303}{\alpha}$$

The dose depth relationship can then be represented by the following equation:

$$z = A \left(e^{\frac{D}{B}} - 1 \right)$$

where D is the dosing. It can now be seen that varying the dose will clear different depths of PR, as further shown in Figure 31.

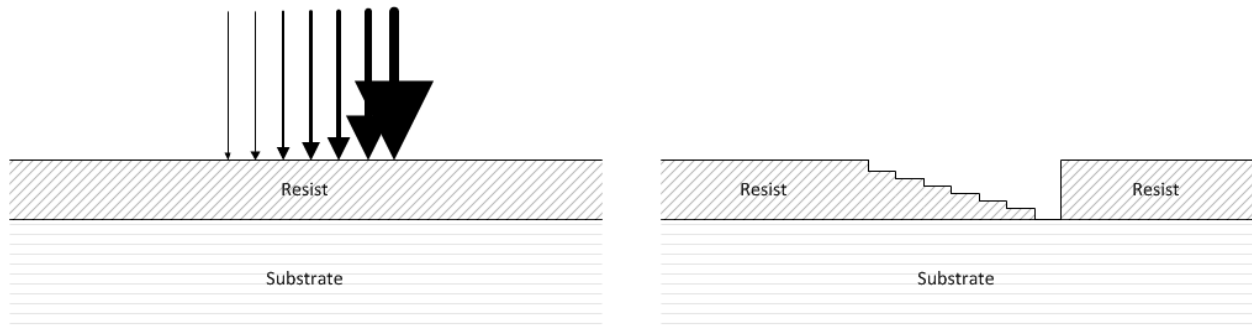


Figure 31 Varied dosing across the PR and its ideal development.

In reality, doses between Q_0 and Q_f will result in partial development and make up the “gray” region of the PR. Gray-scale lithography uses this region to its advantage. Many 3D structures and topographies can be fabricated in a single exposure step. Accurate 3D structures are useful in creating integrated micro optics, such as Fresnel lenses [77], micro-opto-electro-mechanical systems (MOEMS), micro-fluidics (“lab-on-a-chip”) and MEMS. [65] For conventional photolithography to produce a stair-stepped shape like the one above or any 3D structure, it would require multiple applications of PR and multiple masks.

Because gray-scale lithography (GSL) involves varying degrees of exposure, CMTF is less meaningful, and the performance of PRs is primarily characterized by contrast. The gray-scale contrast can be defined as

$$\gamma = 2.3 \left(1 + \frac{A}{z}\right) \left(1 + \frac{z}{B}\right)$$

and evaluated at the depth z . It is very important to understand this intermediate dosing region along the slope of the contrast curve. In fact, it is beneficial to have a large gray region. A shallower slope gives more increments of dosing and allows increased control over levels of exposure. Unlike in binary photolithography where resolution is given by the smallest feature size you can properly image, in gray-scale photolithography, it represents the control over exposure levels. In this case, higher resolution means it is easier to write varying heights, or different levels of gray. PMMA is preferred because it has a very low contrast [83], so it exhibits very high resolution, which is beneficial to fabricating 3D structures.

There are several forms of lithography and irradiation that have been adapted to perform GSL. The first is an adaptation of photolithography methods involving gray-tone masks (GTMs). A binary approximation of GTMs, known as half-tone, were used first. Examples of the shading can be seen in Figure 32. These masks involved using a varying density of dots or other amounts of coverage to partially shade sections of the mask. This technique can be seen on early dot-matrix printers. In fact, these have

even been fabricated by ink jet printers. [84] The limitation of this technique is based on the resolution of the image. The dots used for shading must be much smaller than the minimum feature size. Otherwise, the dots themselves will be imaged instead of simply regulating the amount of transmitted light. This was usually accomplished by using the masks in 5:1 projection photolithography. [85]



Figure 32 Shades of gray approximated by half-tone in monochrome and continuous tone in true gray-scale.

True gray-tone, or continuous tone, masks have been fabricated using high-energy-beam-sensitive (HEBS) glass. Commercially available from Canyon Materials, Inc., the glass has silver alkali-halide complex crystals diffused into the surface about 3 μm . [65] HEBS does not require etching. [86] When exposed to different amounts of energy (UV or e-beam), the crystals become metallic silver and optical opaqueness changes. [87] The fabrication of continuous tone masks requires a GSL method itself. Color has also been used to vary the intensity of light in a mask by using the ink-jet method mentioned above. [84] Again, the benefit of using a mask is that a large area can be written in a single shot. Although parallel processing might be faster, direct write options are much more flexible.

Continuous profile writing can be done with a shaped light beam. [85] A homogeneous light illuminates an aperture that changes the shape of the light beam. The light dose distribution is related to the shape of the beam. The light beam's shape can be modulated by a LCD device. Similar, laser direct-write (LDW) or laser-beam writing can be used. [77, 88] In LDW, an acousto-optic modulator regulates the intensity of the laser beam. In the first example UV light is used, and in the second a helium-cadmium (HeCd) laser was used.

Parallel direct-write or mask-less systems take advantage of both photolithography and direct write lithography methods. It is not only possible to do binary writing with digital micro-mirror devices (DMDs) but to also perform gray-scale exposure. The SF-100 Maskless Lithography system from Intelligent Micropatterning LLC contains a UV lamp, shutter timer and smart filter that controls the DMDs from a PC. Each DMD images one pixel, and the "software mask" orients these appropriately in order to produce a pattern. By varying the time, or duty cycle, each mirror exposes a pixel and a differing dose level is obtained. A field exposure of 16 x 11 mm has been done with 256 levels of dosing. [AM]

3.3.1 3D Electron Beam Lithography

Another direct-write method capable of utilizing the gray-scale lithography method is EBL. Gray-scale EBL, or 3D-EBL, utilizes dose modulation to create a state-of-the-art fabrication technique that is capable of producing sophisticated high aspect ratio 3D structures. In this more advanced technique, a dose matrix is used. With a dose matrix, different areas of the PR are exposed to varying levels of energy, which results in the break of polymer chains throughout part of the PR. Development then leads to varying depths depending on the dosing of the regions, which generates 3D structures.

Dose, as described before, is the amount of energy per area:

$$D = \frac{I \times T}{A}$$

where I is the beam current, T is the exposure time, and A is the area. The key is to have control over the incident energy. The area is effectively fixed by the focus of the electron gun, and beam current is difficult to change without changing the area. These parameters also cannot be changed very quickly. Therefore, time is the most obvious parameter to adjust dose. If the area and beam current are maintained relatively steady, time can be varied and therefore dose will also be varied. The area of exposure, which is usually thought of as a pixel, is the step size squared. The time that the area is exposed is referred to as the dwell time. The current of the beam is measured, and then dose for each pixel can be calculated. This is known as shot modulation. 3D-EBL offers freedom to pattern with a combination of widths and depths. Unlike RIE, which is limited by the lag effect, the shrinking effect that is present in EBL can be compensated. [89]

Some of the PR suitable for EBL can be utilized in 3D lithography. SU-8 does have a small contrast, so it can be used for 3D-EBL [75], but it may otherwise be difficult to deal with. SU-8 is a negative PR, so hardening occurs from the top down. In gray-scale exposure, hardening is done incompletely, so the base may not be fully hardened, and the pattern can lift off of the surface. Transparent substrates can be used in order to expose the PR at the bottom, but this changes the standard flow considerably. [65] ChG has also been shown to make gray-scale patterns but only to 600 nm resolution. [90] PMMA offers lower contrast than SU-8 and higher resolution than ChG.

Although the speed of EBL is a drawback, 3D-EBL has the added benefit of single pass patterning. Not only does the direct write method of EBL not require a mask, but 3D-EBL does not require the multiple masks that would be needed to realize these 3D structures normally. Due to the ability to vary levels, a single scan exposes the 3D pattern in entirety. There is no need for multiple steps, which eliminates the risk of alignment issues. Furthermore, with thermal reflow post-treatment, these stair-stepped patterns can be averaged, or smoothed, to create continuous patterns [91]. The EBL system is a flexible and an

ideal solution for a wide range of applications in engineering, biology, medicine and micro-fluidics, which require a resolution under 50nm. 3D-EBL is good for machining MEMS devices, such as optical elements (coupling for optical fibers, tilted mirrors, compound micro-prisms), [92, 93] and especially necessary for high-frequency gratings, photonic band-gap crystals, magneto-resistive random access memory (MRAM) and other nano-electro-mechanical systems (NEMS). [94] 3D-EBL has also been demonstrated on functionalized SU-8 PR to fabricate single-model solid state dye laser devices. [88] The high resolution is a major attractor to EBL, but due to the speed limitation, 3D-EBL is primarily used for mask making and nano-imprint lithography (NIL) utilizing the soft lithography process explained in the next section.

3.3.2 Soft Lithography

Soft lithography is an extension of molding techniques into the world of micro- and even nano-fabrication technologies. The technique is not used to produce an original pattern itself but merely to replicate a micro or nano pattern that has been already created through another process. The materials are poured onto molds that were fabricated with a pattern. They are then peeled away and left with an imprint of the pattern. The resolution has been demonstrated down to less than 20 nm. [95]

The term “soft” refers to the use of elastomeric materials in the process. The use of these materials allows for the conformal contact of the surface, even at the sub micrometer level. Flexible materials are also easier to remove from the molds, because they PR breaking when peeled from the template. Soft materials can also be imprinted through thermoplastic or photo methods, such as in NIL.

In general, the soft lithography process also allows patterning of materials that are not photosensitive or cannot be patterned directly through other lithography processes. This expands the application of micro-fabrication from electronics to the fields of bioengineering and other medical technology, such as

cardiac stents. Different materials, which are biocompatible, can be micro patterned. Drug-embedded polymers have been used, and research is even being done to directly shape drugs to improve delivery.

The molding process in soft lithography can also be used to increase the mass production ability and lower the cost. Expensive lithography equipment only needs to be used for making the molds and not for each pattern after that. Soft lithography can also be performed in normal laboratory settings, further opening the door to widespread application. The imprint process has been adapted to other forms of mass production, much like that of a printing press.

4 PROCESS

4.1 Design

The ultimate goal of this project is to create an IOL that has adjustable power, which is precisely tunable by design, producible in fabrication and accurately repeatable during normal functioning. Instead of creating original and artificial designs to obtain the goal, the plan is to mimic the design concepts shown in nature. This process is known as bio-mimicry and is an ever more popular idea being utilized in biology, medicine and several other engineering fields. A lot has been learned and improved upon by looking closer at how nature creates structures and runs processes.

The general idea of bio-mimicry is that nature has already tested out various design possibilities, sometimes over the course of millions of years, and, for the most part, found a better and possibly the best way to do something. One example is the waterproof fibers manufactured by spiders, which are five times as strong as steel. [96] Even though advances in technology and engineering have created ideas and devices that have no comparison to nature, there are plenty of cases where the man-made option is less fitting than its natural counterpart. However, it is not only a question of which one is better, man-made or natural, but also that we should first understand nature and build from that solid foundation. The method of bio-mimicry especially makes sense when designing an artificial, direct replacement for a natural object, such as the lens of the eye.

It was shown earlier that the lens is a collection of small elongated lens fibers. The lens fibers remain transparent due to their internal construction, their regular order and size. To match their natural size, any structure designed to allow for the adjustment of focal distances would need to be at least on the micro scale in order to not degrade optical quality. It was shown by earlier research [26] that micro-meter spacing in an IOL is not small enough. In this project, the spacing is shrunk into the nano scale and

curvature is added to the overall topography of the IOL design. Advanced photolithography systems can fabricate sub 200-nm features. In fact, Intel produces 32-nm resolution for use in processors every day. These processes cannot realize the detailed 3D structures used in this project; therefore 3D-EBL is the method used. Like the natural lens, the replacement IOL will also need to be flexible in order to accommodate. 3D-EBL can create the structure, but it cannot be done on such flexible materials. Soft lithography will be used to transfer the pattern to a flexible material that will allow for accommodation.

4.1.1 Channels

Besides using micro-fabrication techniques in the production of the lens, the major improvement in this design from normal IOL is the introduction of channels. As demonstrated in Figure 33, the channels allow for the compression of the lens structure and an overall change in curvature or focal power. Their size and spacing will also change the flexibility of the lens. There must also be a balance in the size, because it is critical in reducing both spherical and chromatic aberration.

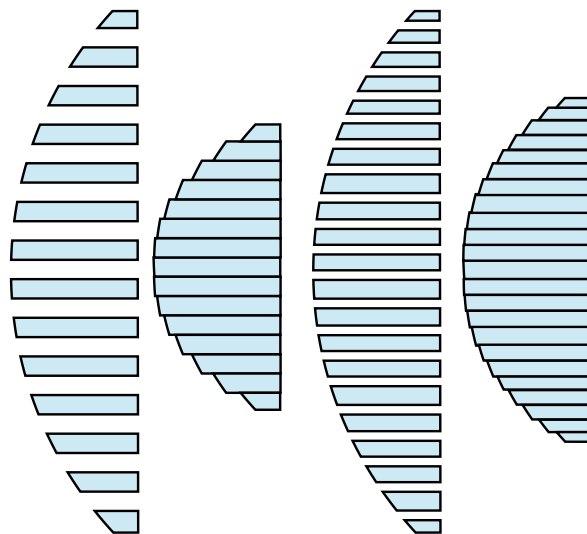


Figure 33 Varying channel size and resulting curvature change.

4.1.2 Spiral

Use of the spiral pattern, which was introduced in previous UIC/NCF research [26], continues in this project's design. The spiral is a shape that is present throughout nature: spiral formations in shells, such as those of mollusks; curves of a wave peak; the draining of a sink; the funnel of a tornado and hurricanes. The spiral is a progression of material organized through symmetry in transformations of growth and rotation in the natural world. They are also evident on a much larger scale: magnetic forces emanating from the sun in the Parker spiral [97] and even spiral galaxies.

One benefit to a spiral is that it allows for compaction of a relatively long continuous path [98], for example: the groove on a vinyl record, the data on a CD or hard drive, or the bulb of a compact fluorescent. Another benefit is that they maintain physical strength while increasing surface area, such as in the logarithmic spirals in nautilus shells. Spirals have benefits in other ways. The cochlea, an inner organ of the ear that forms a spiral, not only saves space but also improves hearing by enhancing vibration and directing different frequencies to different places in the cochlea in order to distinguish them. The concept of the spiral has also been applied in the electrical engineering world: spiral inductors [99], ferroelectrics of spiral magnetic [100] and broadband antennas for terahertz radiation [101, 102], which have been fabricated by EBL [103].

The general definition of a spiral is the path of a point in a plane moving around a central point while continuously receding from or approaching it. Geometrically, the shape of the spiral can be represented many different ways. The logarithmic spiral is more representative of what is seen in nature; while the Archimedean spiral is the human simplification. A log spiral not only has an increasing distance from its center but it is logarithmically increasing as well. A special type of log spiral known as the golden spiral, has a growth factor equivalent to the golden ratio, which seems to be found everywhere in nature (and has been obsessed about throughout human history, such as in the movie *Pi*). The golden spiral is often

approximated with a Fibonacci spiral. The Archimedean spiral has a linear increase in distance from its center, so each arm is a set distance apart. These types of spirals can be seen in the real world on scroll compressors.

Mathematically, it is easy to see the increasing radial of the spiral. Because a spiral is a non-unique¹ curve, it is best described using polar coordinates or a set of parametric equations. A log spiral is described by

$$r = ae^{b\theta}$$

while a Archimedean spiral is described by

$$r = a + b\theta$$

where a and b are arbitrary coefficients that change size and ratio of growth. The Archimedean spiral is also represented by a set of parametric equations

$$\begin{cases} x = at \sin bt \\ y = at \cos bt \end{cases}$$

with the parameter t.

Although the log spiral might be seen more in nature, the Archimedean spiral's regular distribution closely resembles that of the regular structure of the eye and is the choice for this project. The equal spacing between each arm of the spiral should provide uniform movement and deformation when the lens is stretched and compressed. The proposed IOL design is not just a 2D spiral; overall the spiral shape will be domed (or convex) to match the curvature seen in a natural lens. The shape then, more appropriately, is that of a conic helix in which the depth (z) also varies with radius.

$$z = ct$$

¹ A function that has multiple solutions for one value, for example: a unit circle, where for x=0, y = +1 and -1.

4.2 Substrate

Because this work focuses on the structures made in the PR alone, the substrate is merely a carrier for the PR. Therefore, there are not many important properties to note. One requirement was stated earlier in the section on EBL: the substrate must be conductive. Another is that the substrate must be compatible with the PR and the processes that it is taken through. And last, it must be easy to cut and deal with in sample form. Si is a substrate that is readily available because of its use in other semiconductor fabrication. It is easy to deal with in the lab, easily cut and the proper material for PR application. Also, it is conductive enough to shunt electrons to ground in order to avoid charging effects. The substrates used in this project were 2-inch Si wafers (110) from Wacker.

4.3 Photo resist

Although there are several other PRs capable of being utilized in EBL, such as SU-8, ChG and HSQ, they did not meet the requirements of this project. PMMA was the choice because of its bio-compatibility, contrast, and processing ease. One of the reasons PMMA is easy to process is due to its application; it is applied similarly to other standard PRs in a process called spin coating. Spin coating involves rotating the wafer at a set speed while applying the PR to the top of the wafer. The spinning action forces the liquid PR to the edges. As the PR spreads to the edges, it leaves a film due to surface adhesion to the wafer. The film's thickness is determined by utilizing spin curves from the supplier. Spin curves are charts where thickness is plotted as a function of the spin speed in RPM. For each different type of PR, there is a spin curve. The curve depends on many factors, but molecular weight (MW) is a key one.

In general, PMMA adheres well to most materials and normal cleaning of the wafers is the only surface preparation needed. In highly critical applications and to help materials that may have trouble adhering to Si normally, the wafer goes through a set of cleaning procedures: solvent clean, de-ionized water (DI) rinse, and possibly a hydrofluoric acid (HF) dip in order to get rid of a native silicon dioxide layer. If the

wafer was used for electrical properties or was going into high-temperature processing steps, it might need an RCA clean¹ in between, which is a standard set of cleaning steps. For all the tests performed as part of this project, the Si wafer was only cleaned with DI because the adhesion of PMMA was satisfactory. No adhesion promoters, such as HDMS (hexamethyldisilazane or bis(trimethylsilyl)amine), which is used even with standard PR (i.e. Shipley MICROPOSIT™ S1818™), are used. There are also no shelf life or film life issues with PMMA, and it is not sensitive to white light. [104]

There are several dilutions of PMMA available that allow for a wide range of thicknesses. A depth of 250 nm was chosen because any greater thickness would result in unacceptable electron scattering. Specifically, MicroChem 495PMMA A4 (MW of 495 kg/mol, 6% solids in Anisole) was used for this project. In order to obtain a depth of 250 nm, the PR and wafer were spun for 45 seconds at 1500 RPM. Immediately following this step, the wafer was placed on a hot plate, which was at 180 °C, for 60 seconds. This pre-exposure bake or “soft bake” is critical, because it removes most of the solvents from the PR. [104]

4.4 Samples

Samples are cut after the application of PR. This increases throughput by allowing multiple samples to come from a single wafer. Spreading the PR over the entire wafer also makes for a smoother PR layer. PRs tend to bead up at the edge of the wafer, so samples close to the edge might have thicker PR. A larger area minimizes this effect. The radial variation of thickness is usually around 16 nm [AW], or only about 3 %² of the total PR height.

A sample size of 10 by 10 mm was chosen. The sample size is compatible with the sample holder used in the EBL system. This size allows for easy handling and plenty of writing room for several patterns. The

¹ Cleaning process developed by the Radio Corporation of America involving a 3-step process to (1) remove organic contaminants, (2) remove the thin oxide layer and (3) remove ionic contamination.

² Considering a 2-inch wafer can get about 5 samples in width: $16 \text{ nm} / 2.5 / 250 \text{ nm}$.

sample also would be able to fit a full scale model of the lens. The wafer was cut using a Micro Automation 1006A Wafer Dicing Saw.

One holder for the EBL system is designed for smaller samples and has 6 individual clips for holding them. Each square sample is placed flat against the right side of the holder, and one clip holds it in place. The lower-left corner is scribed to mark the origin. The samples and holder are dusted off with argon (Ar) gas and loaded directly into the chamber of the EBL, because there is no airlock and loading mechanism installed.

The chamber is then closed and pumped down to operating pressure. First, a piston-type roughing pump takes down the pressure from atmosphere, which is 1013 mbar, to about 50 mbar. In the range of 50 to 1 mbar, the roughing pump lowers its speed as the turbo-pump increases speed and takes over. At 1 mbar, the turbo-pump is at its minimum speed. In total, this process takes only about 30 minutes to achieve the operating pressure of 2×10^{-5} mbar.

4.5 Electron Beam Lithography System

At UIC, the Nanotechnology Core facility (NCF) houses a 100 e_LiNE (electron beam Lithography and Nano Engineering workstation) EBL/SEM system from Raith GmbH, as pictured in Figure 34. Simply referred to as “the Raith”, this system is turn-key including all electronics, PC, software and vacuum systems. Only utilities, such as cooling water, nitrogen, environmental control, and electricity, are required externally for service.

At the heart of the Raith is a thermal-assisted field emission source, which utilizes a Schottky filament of zirconium oxide-coated tungsten. Maintenance is only required once a year with a TFE element as opposed to a plain tungsten filament, which requires monthly maintenance. A current of around 2 A runs through the filament to heat it up, and an extraction voltage of around 5 kV is used for field

emission. Beam current from the gun itself is around 160 μA . Vacuum is always maintained on the gun, and the pressure is much lower than that of the chamber: around 1×10^{-9} mbar. Due to the separation, loading times can be minimized to about 30 minutes, even though there is no airlock on this configuration of the Raith.

The column is of unique design; in the Raith there is no beam crossover due to the lenses, so the column is able to maintain extremely high beam current density. This allows for low voltage inspection and metrology below 1 keV. The column also features a compound objective lens that lowers aberrations. [105] All of the optics are digitally controlled and allow for precision adjustment for focus and astigmatism correction. Acceleration high voltage (AHV) in the column can be changed from 0.200 to 30 kV.

The sample stage has a travel range of 100 x 100 x 30 mm. The last distance, z, is referred to as the working distance and is the height of the end of the gun from the sample stage. Movement of the stage is done in combination with DC motors for coarse or fast adjustment of 0.2 microns and piezos, with closed loop control for fine movement in the nm resolution. A laser interferometer controls the position to 2 nm precision over a distance of 5 cm. Overall, this makes it possible to perform stitching with around 60 nm precision. [106] Multiple pattern overlay accuracy is 40 nm.

The Raith features 6 different sized apertures with which the beam can be steered through: 7.5, 10, 20, 30, and 120 μm . With the aperture size and acceleration voltage, beam current ranges from 5 pA to 20 nA and results in a current density greater than 7.5 A/cm^2 . The stability of this current is guaranteed to be less than 0.5 % per hour. Some researchers have measured the stability to be as low as 0.8 % for 36 hours [105]. The high-speed deflection controller runs at 10 MHz and allows for a minimum dwell time of 100 ns. The maximum dwell time is 500 ms, and it can be incremented by 1 ns. The maximum beam

speed is about 15 mm/s. A write-field can range from 0.5 μm to 2 mm. As an example, the step sizes result for a 100 μm area is 1.6 nm using 16-bit addressing.

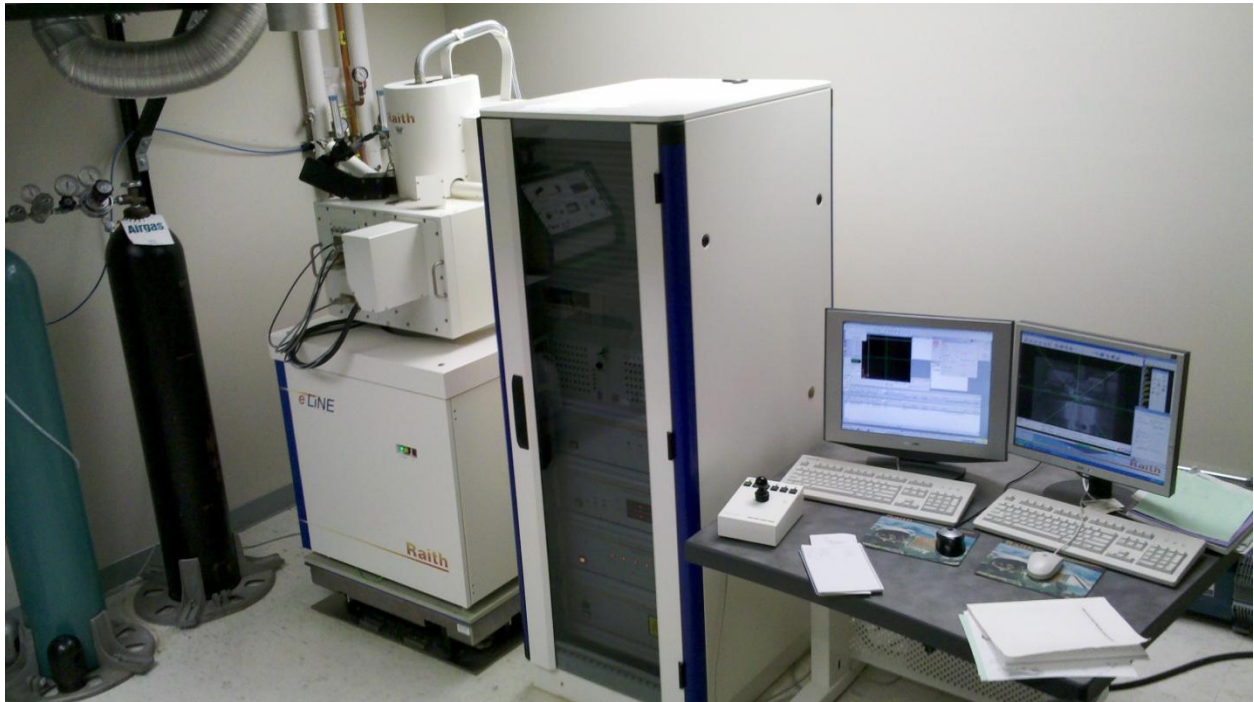


Figure 34 Raith 100 e_LiNE in NCF at UIC

4.6 Pattern

The Raith includes a full-featured pattern design tool within its software package. The software utilizes the Graphic Database System II (GDSII) format, which is also known as “Calma Stream” and currently

owned by Cadence Design Systems. GDSII is a format used in most lithography software. [71] Besides the Calma Stream File (CSF) or GDSII file (GDS), other files such as Drawing Exchange Format (DXF), Caltech Intermediate Form (CIF), and American Standard Code for Information Interchange (ASCII) can be loaded as well.

Within a GDSII database file (CSF/GDS), there can be many structures, which are referred to as cells in other software. A structure is composed of various shaped objects. Like in CAD programs, each object is a connection of points that comprise a polygon. These can either be drawn by dot, line, rectangles, etc., or each polygon can be created by drawing it and connecting lines. Using Calma Stream, each polygon can be composed of a maximum of 1024 points. As such, very complex shapes can be created. Not only can letters and numbers be well defined, but curves, such as circles and arcs, can be estimated¹ well too.

This maximum number of points also gives Raith the freedom to introduce the “group of curves” function. This function allows a user to draw a curve or set of curves based upon an equation or incrementing set of equations. Several different sets of curves are preinstalled: cardioids, strophoids, zykloids and stars. The objects provided may not be directly applicable to a circuit or structure fabrication, but they demonstrate the flexibility of the software. As mentioned before, similar curves have been used for spiral terahertz broadband antennas that have been fabricated by EBL.

Each structure inside of the GDS can have multiple layers containing different arrangements of polygons. This is exactly like the layout of a CAD file. Multiple layers can be used to either separate polygons for simplicity, or to lay out multiple layer devices, such as in the construction of an actual electronic or MEMS device. Each layer can be exposed separately, as will be presented later in this paper.

¹ Curves are estimated by points and straight lines. The more points that are included and the smaller the object, the better the approximation.

Structures can also reference other structures. This hierarchical system is much like that of other VLSI design software where circuit patterns, or cells, are repeated multiple times. For example, a negated-and (NAND) gate is a fundamental building block for digital circuits from which many other gates are made. The NAND could be built as one structure. Then, 4 of the NANDs could be referenced and connected in order to build an exclusive-or (XOR) gate. This can be cascaded multiple times to create larger and more complex circuitry.

The polygons are layered in 2D; however, 3D structures are handled directly by the software. Each polygon can be assigned a dose, which is a positive number with up to 3 decimal places. The dose relates to the depth of the exposure for that polygon. Several actions such as scaling and incrementing allow for the dosing of multiple polygons to be varied. A bitmap (BMP) can also be imported¹ directly, which allows different shaded areas in 8-bit gray-scale to become polygons of different dosing.

4.7 Image Generation and Conversion

There is also a software utility available² from Raith that expands the 3D functionality of the software package. The utility, known as 3-dimensional E-beam Lithography Software (3Lith), is a universal calculation software that renders GDSII patterns. 3Lith involves scripts with several functions. First, it calculates diffractive optical elements, such as Fresnel lenses and phase holograms. Next, it simulates reconstruction of the hologram with any wave length of light and calculates the patterns resulting after development. Last, it transfers diffractive optical elements (DOE) patterns or other images into exposure patterns considering proximity effects.

Holograms and Fresnel patterns can be generated by single commands and parameters. Other elements can be generated via equations. The image is treated like a pixel matrix with the origin (1,1) being at the

¹ This function did not import 8-bit per pixel images when it was used.

² Additional license required.

bottom-left and every pixel being incremented by 1 from that point for columns and rows. The equation then performs like any other in an x-y coordinate system. The resultant value $f(x,y)$ when entering the pixel (x,y) in the equation is the depth/height.

The most utilized function of the software utility in this project is the image-to-pattern conversion. Using external images made it easier to design patterns that were otherwise too difficult or impossible to construct in the GDS directly. Any 8-bit grayscale Tagged Image File Format (TIFF) image can be converted into a GDS pattern. Depending on the settings, each pixel is converted into a rectangular object and then the 256 shades of gray are converted into 100 levels of height. Each pixel then can be adjusted to a dose level, because the dose-to-height contrast is not linear.

Original image patterns were generated by the GNU Image Manipulation Program (GIMP). These files contained any amount of drawing or colors. Eventually, the images were exported as 8-bit grayscale TIFF images, with no alpha channel or compression, in order for 3Lith to process it. The image-to-pattern conversion function allows for any digital image to be converted to a pattern, such as a picture of Albert Einstein, which is featured in the Raith 3Lith manuals. [107, 108].

4.8 Proximity Correction

Different models allow for estimation of the proximity effect. A double Gaussian function is used to approximate the point-spread function

$$f(r) = \frac{1}{\pi(1 + \eta)} \left(\frac{1}{\alpha^2} e^{-\frac{r^2}{\alpha^2}} + \frac{\eta}{\beta^2} e^{-\frac{r^2}{\beta^2}} \right)$$

where α is the forward scattering parameter, β is the back-scattering parameter, η is the ratio of the backscattered to forward scattered energies, and r is the radial distance given by

$$r = \sqrt{x^2 + y^2}$$

This function is only a 2D approximation of the phenomenon. In order to give better estimation for certain substrates, multiple layers, and very small feature sizes, triple or multiple Gaussian equations are used in approximation. For example, the Raith's software utilizes an extra term in the approximation, and the equation is

$$f = \frac{1}{\pi(1 + \eta + v)} \left(\frac{1}{\alpha^2} e^{-\frac{r^2}{\alpha^2}} + \frac{\eta}{\beta^2} e^{-\frac{r^2}{\beta^2}} + \frac{v}{2\gamma^2} e^{-\frac{r}{\gamma}} \right)$$

where the additional terms γ and v take into account the depth dependence of scattering. All of these parameters are determined by acceleration voltage, substrate and PR parameters. At 10 kV, the beam diameter is estimated to be 10 nm. Because α is the forward scattering parameter, it is determined by the PR parameters. PMMA has a scattering coefficient of $7.5 \text{ kV}^2/\mu\text{m}$ and, in these samples, has a thickness of 250 nm. The forward scattering parameter is estimated to be $0.3566 \mu\text{m}$. Most of the back-scattering is due to the substrate, so β is estimated from Si values: $\beta = 0.6 \mu\text{m}$, $\eta = 0.75$ and two other relevant constants are $0.01656 \mu\text{m}$ and 1.55908 .

The software that comes with the Raith has built-in support for correcting patterns based on these estimations. Several parameters determine the practical side of the estimation calculations and corrections. Partitioning for calculation involves the maximum interaction distance (default is 7000 nm), which is the radial distance from which to account for the effect of a scattered electron, and the maximum number of elements to calculate (default is 5000). Fracturing is the correction of the pattern and involves two parameters: raster size (200 nm) and atomic size (100 nm). The proximity effect correction module was developed in collaboration with the Zurich Electronics Laboratory's Communication Photonics Group.

4.9 Exposure

After loading a sample, the first step is to set up the e-beam column. An acceleration voltage of 10 kV was used with a 30 μm aperture at a working distance of 10 mm. The parameters selected for this project, x1000 magnification, resulted in a write-field of 100 μm . The beam size is less than 2 nm and minimum line width of 20 nm is guaranteed at 20 kV with a 30 μm aperture. The column is capable with up to 30 kV, but 10 kV at 10 mm working distance (WD) is recommended as a good starting point for general patterns [106]. Because the goal of this research is not only fine lines and 250 nm structures, the beam size at lower acceleration voltage is not detrimental to the patterning. The aperture size of 30 μm is also recommended for general patterns. Smaller sizes of 7.5, 10 or 20 μm offer finer beams, but they also limit beam current and subsequently increase writing time.

The next step is to measure the beam current in order to calculate beam speeds. This is done by using a Faraday cup. In its simplest form, a Faraday cup is a conducting chamber that intercepts charged particles from the beam and from which current is measured. Improvements, such as a bias grid, may be added to reduce secondary emission that distorts the measurement. Even though the pressure only 30 minutes after loading allows for exposure, the current is much less stable at that time. During this research it was discovered that allowing the vacuum to pump down for over 4 hours reduced the current fluctuation to around 1% per second.

4.10 Development

For the development of PMMA, a methyl isobutyl ketone (MIBK) 1:3 isopropyl alcohol (IPA) mix was used. Individual samples were dipped into the mixture and lightly agitated for 60 seconds. Immediately after the sample was removed and submersed in pure IPA for 30 seconds to stop the development and prevent “scumming” [104]. The sample was then blow dried with N_2 . Hard-bake was not implemented,

because there was no further processing steps which would require this. These steps followed the manufacturer's [104, 109] processing guidelines.

Some articles reviewed by this author discussed different developers to provide the best contrast. One article claimed a MIBK diluted 1:2 with water had the best performance. [88] Another used undiluted MIBK to optimize sensitivity and contrast characteristics of PMMA. [93] In a production cycle, for the best performance, development may be performed in an ultrasonic bath at room temperature. [94] PMMA does exhibit shrinkage after e-beam exposure [88], and dry development may be an option to help this [110].

4.11 Post Processing

The most popular form of post processing is thermal reflow, which is sometimes called thermal annealing. Thermal reflow is a well established and simple method for modifying the shape in PR, and is used widely on spherical or cylindrical lenses [111]. The glass transition temperature (T_g) is where the PR changes to a viscous state, and surface tension causes the PR to flow to areas with least energy, i.e., minimum height. T_g depends on the MW [93] of the material. Higher e-beam exposure, or dosing, reduces MW, which lowers T_g and in turn, the viscosity (η) of the material at that temperature. Unexposed PR shows less effect from the heat; therefore, well-defined high-aspect ratio devices are still maintained, while slopes and bumps are smoothed out. For PMMA, T_g can range from 85 to 165 °C depending on the composition available commercially. [111] Temperatures above T_g lead to reflow and deformation of non-exposed areas, but lower temperatures cause incomplete reflow. [91] Instead of heating the entire sample, localized heating by laser also has been used. [111]

The pattern formed in the PMMA can also be transferred into the substrate itself. This has been done for SU-8 micro structures to form negative replicas. [74] Reactive ion etch (RIE) has been used to transfer PMMA proportionally to the substrate in order to form stamps [111] for nano-imprinting,

injection molding or roll-to-roll processing. [93] Proportionally refers to the fact that the established height differences are maintained, while the exposed PR thickness is reduced all the way to the substrate. Cryo-etch can maintain the height difference the best. [110] MW variation does not affect the etching rate, so density, not length, of PMMA changes the etch time. [93] For a close 1:1 etch rate (i.e., 8.97 nm/s for Si and 8.72 nm/s for PMMA), RIE was used with the following parameters: RF power of 200 W, pressure of 100 mTorr and oxygen flow rate of 2 SCCM. [86] The pattern can also be transferred by a process of casting in order to fabricate stamps

4.12 Soft-lithography

PDMS was used for the soft-lithography process in this project, because of its biocompatibility, transparency, flexibility and ease of processing. Specifically, Dow Corning Sylgard® 184 Silicone Elastomer Base and Curing Agent were used. A mixture of 1:10 was used, which was usually 0.5 g and 5 g, of the curing agent and base, respectively. It was measured and mixed in aluminum foil. The sample was placed in a 2-inch plastic dish and then the mixture was poured on the sample. The dish was placed in a desiccator and put under vacuum in order to release the air bubbles from the mixture. The PDMS was set to cure over 24 hours.

The PDMS was then carefully peeled off of the sample. The total diameter of the PDMS was 2 inches, due to the size of the container that it was cured in. The excess was cut from the sample imprint, so that it would be the same size as the original PMMA sample. The size is an essential consideration when working with the AFM. In most cases, the origin scribe mark was transferred to the PDMS surface to allow for orientation, identification and correlation of the patterns in the PDMS with the original PMMA mold.

4.13 Measurement

Normal optical microscopy is not very useful in the measurement and analysis of samples used in this project. Optical microscopy is limited by the diffraction of visible light. The average wavelength of the visible spectrum is 550 nm, so the theoretical resolution limit is around 200 nm. Due to this limitation, optical microscopes were only used for identification purposes and measurements of large features, such as total pattern size. After development, the sample was verified under a Nikon microscope.

Additionally, optical microscopy does not have the ability to give measurements that would fully characterize the surface of the sample. For this, scanning probe microscopy (SPM) is needed. SPM does exactly what the name implies: a physical probe is used to scan the surface of a sample. SPM was first used in the invention of the scanning tunneling microscope (STM). The tip of the STM utilizes quantum tunneling to sense the surface of the sample. STM is very expensive and is used for samples that need tenths and hundredths of nm resolution.

Atomic force microscopy (AFM) is another SPM method that can be used to scan larger areas and greater depths. The tip of the AFM is scanned across the surface of a sample, while it interacts with the atomic force of the surface. The deflection of the cantilever, which holds the tip, is measured by a laser and then determines the differing heights of the sample. This is diagramed in Figure 35.

The tip is usually comprised of Si or silicon nitride and has a minimum radius on the order of several nm. Smaller tips allow for finer resolution, because the force can be measured from a smaller area. The cantilevers of the probes may be coated in different materials to increase reflectivity for the laser. Different materials can be used in substrate of the probe, which holds the cantilevers and tips, to increase durability and precision. For example, NaDiaProbes™ from Advanced Diamond Technologies are AFM probes made entirely out of diamond. [112]

There are also several modes of AFM: contact, non-contact and tapping. Contact mode is the most basic form. As the name suggests, in this mode, the tip is in physical contact with the surface. The tip is lowered or the sample is raised slowly until the atomic force deflects the tip and is sensed. The probe is then scanned across the sample, usually by a piezoelectric scanner that moves the sample in relation to the probe. Feedback from the deflection of the cantilever moves the scanner up and down. By adjusting the z motion, force on the probe remains constant. The z distance of the scanner is measured and recorded. There are several advantages to contact mode AFM, including overall simplicity, high scan speeds, potential to obtain atomic resolution images, and ease of scanning rough samples; however, there are also some disadvantages. Specifically, lateral forces can distort sample features and other forces can damage the sample or the AFM tip. [113]

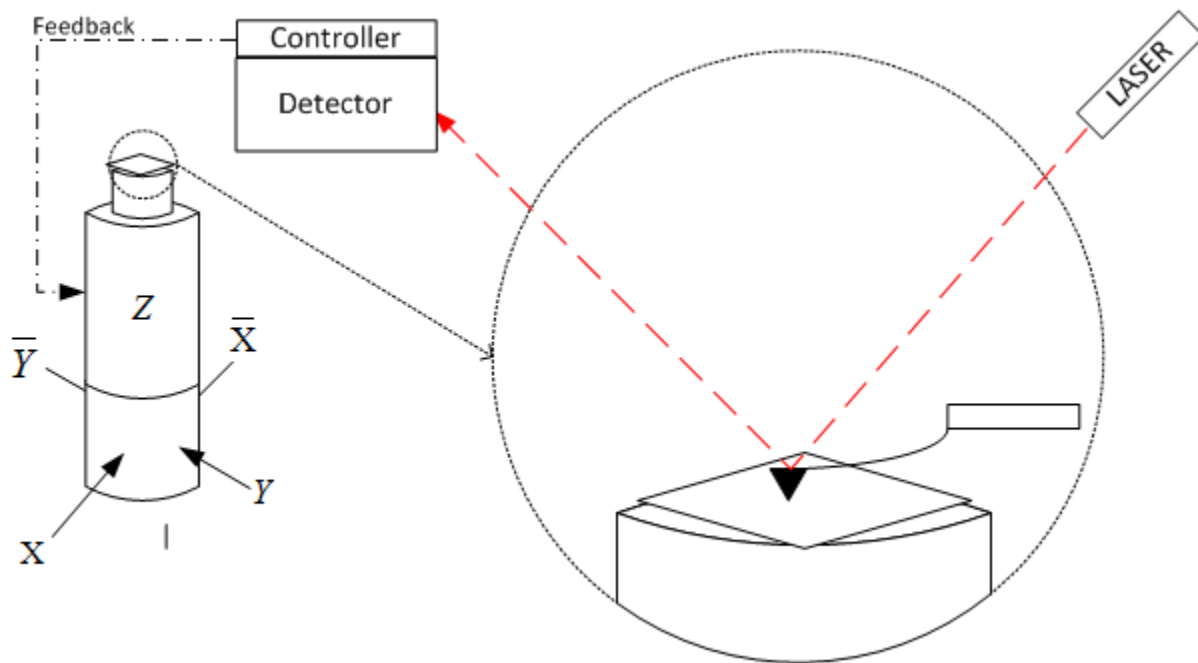


Figure 35 Diagram of AFM operation

Non-contact mode exerts no force on the sample's surface, because the tip is oscillated about the surface. The cantilever is oscillated at a frequency slightly higher than its natural resonance. The amplitude is usually a few nanometers (<10 nm) [113]. The vibration of the cantilever is reduced by the van der Waals forces, which are around 1 to 10 nm above the sample surface. Again, the feedback, which is frequency in this case, is held constant and adjusts the height of the scanner. The changes are recorded. Non-contact mode has a lower lateral resolution and a slower scan speed. It also only works well with extremely hydrophobic samples in order to avoid trapping the tip on the sample.

Tapping mode is a combination of both contact and non-contact modes. The cantilever is oscillated at its resonance frequency. However, compared to non-contact mode, the oscillation amplitude is much greater: 20 to 100 nm. [GF] Due to the greater amplitude, the tip lightly taps on the surface of the sample during the scanning. The feedback loop maintains constant amplitude, and the change in z direction is recorded. Tapping mode has a slower scan speed than contact mode, but it offers high lateral resolution (1 to 5 nm) and lessens damage to the sample. [113]

The AFM used on this project is the Nanoscope III from Digital Instruments (Veeco Metrology Group). The AFM uses a scanned sample method, where the scanner moves the stage and the probe is stationary. All scans were done with a scanner capable of ranges in x and y of 1 - 118 μm (d-type). Oxide sharpened silicon nitride probes from Advanced Surface Microscopy are used, with a nominal tip radius of 5 to 40 nm. [114] Each probe, measuring 3.6 x 1.7 x 0.5 mm, contains 4 cantilevers. These consist of narrow and wide legged small (100 μm) and large (200 μm) cantilevers with differing force constants: 0.58, 0.38, 0.12 and 0.06 N/m. [114] Overall, the tip shape is a pyramid with a square base and an angle between the face and axis of 35° [114], as shown in Figure 36.

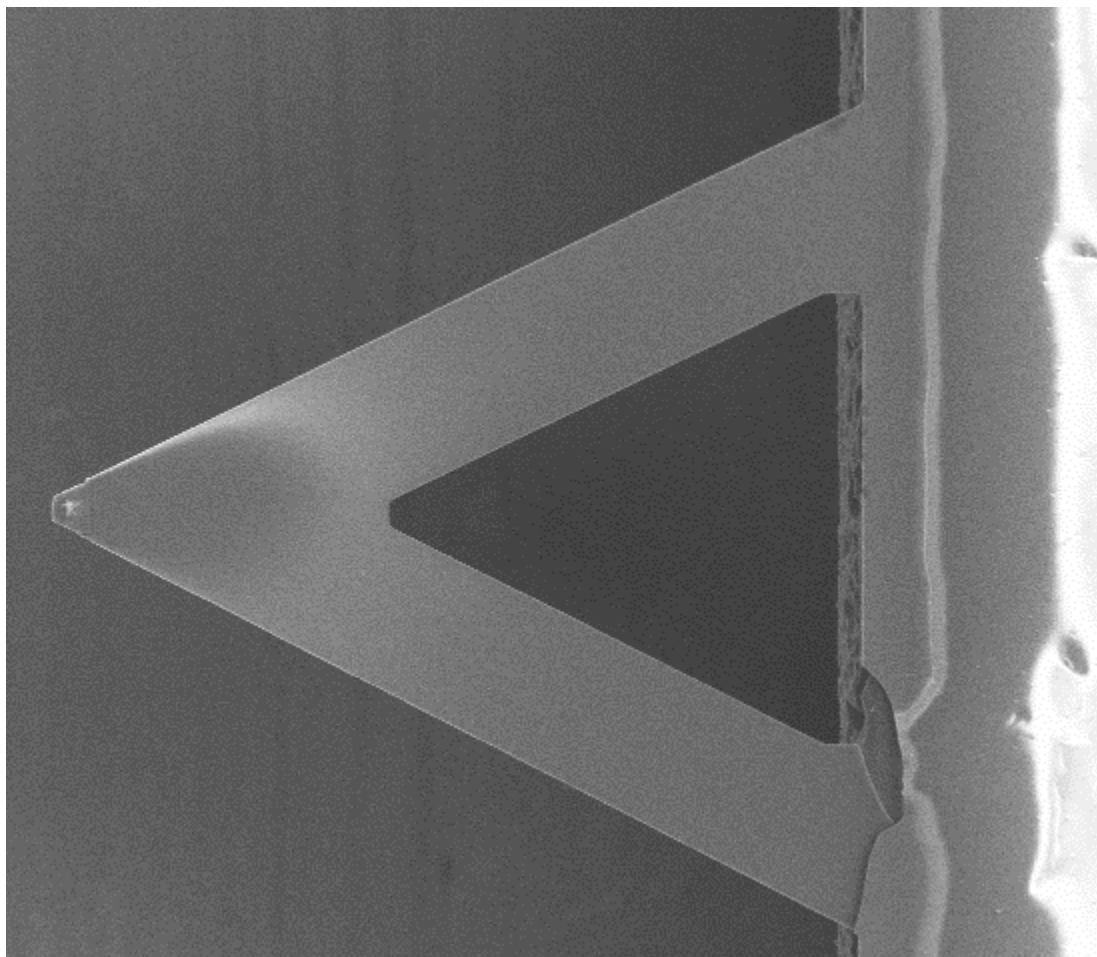


Figure 36 SEM of an AFM cantilever with tip

5 RESULTS

The individual sample creations are presented in this section, and they are analyzed for results. Not all of the sample runs are mentioned. In particular, samples that were “wrong” due to technical issues or human error are omitted. Only samples that have successes or failures that can be learned from are mentioned in this section. The default settings for each run are assumed to be the ones mentioned in Section 4 and Table III below, unless otherwise noted in the description of the run or test.

Table III Default values for process

Filament current	2.390 A
Extraction potential	4.80 kV
Gun current	163.40 μ A
Aperture size	30 μ m
Acceleration potential	10 kV
Magnification / write field	x 1000 / 100 μ m x 100 μ m

5.1 Binary Spirals

The first step for this project was to create a 2D proof of concept. In previous work, deep UV was used to create a spiral lens structure in SU-8. The structure was a 2D spiral with spacing around 100 μ m and arm widths of about 75 μ m, as shown in Figure 37.

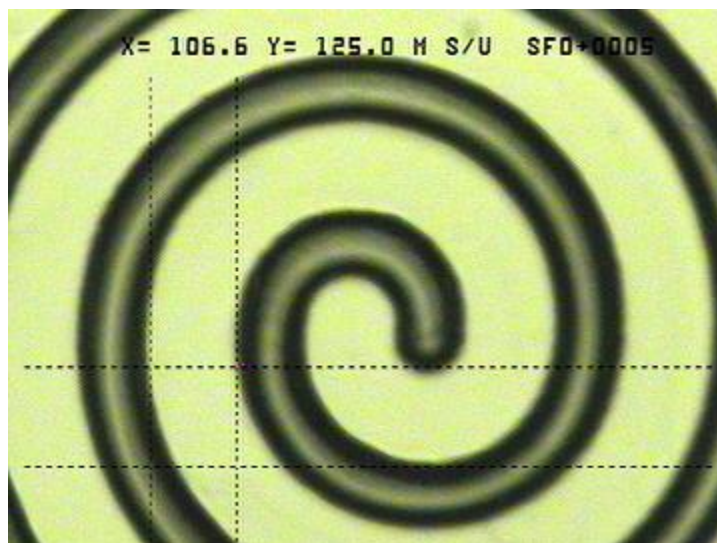


Figure 37 Microscopic image of SU-8 2150 structure with thickness of 600 μm .

[26]

5.1.1 Micro-spiral

The first test fabricated in the EBL was a spiral with 0.5 μm arms with 1.0 μm spacing. The initial tests of EBL (see Figure 38) show several orders of magnitude improvement from the previous research (Figure 37).

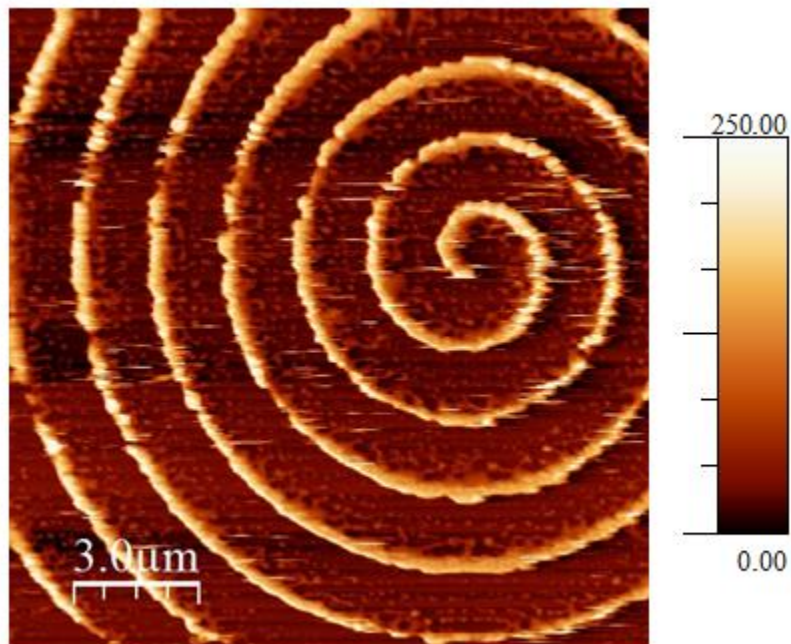


Figure 38 AFM scan of micro-spiral

The structure turned out well with sharp peaks and 250-nm deep trenches in between. The profile of the structure is shown in Figure 39.

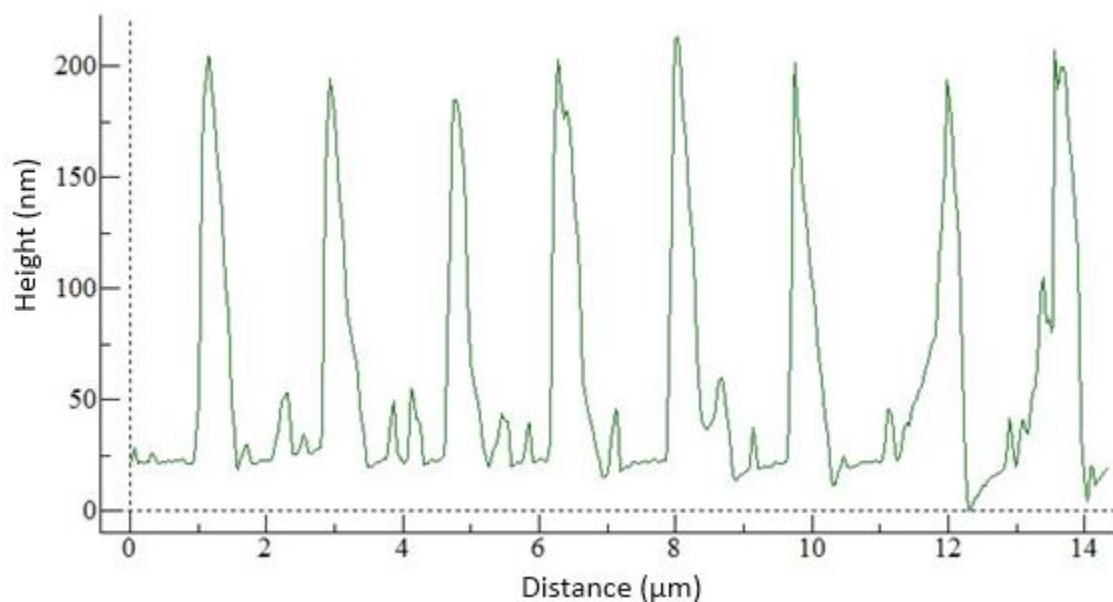


Figure 39 AFM profile of micro-spiral

5.1.2 Nano-spiral

Micro-spacing of the spiral is not difficult for EBL to produce. Once the concept was proven at the same scale used during previous research, the next step was to scale down the structure. The spacing between the spirals would need to be below 500 nm. The first attempt involved a 200 nm line in a 500

nm space. Scaling down the image and writing with the same parameters resulted in underexposure. Dosing factor had to be increased to 12% in order to get the structure shown in Figure 40.

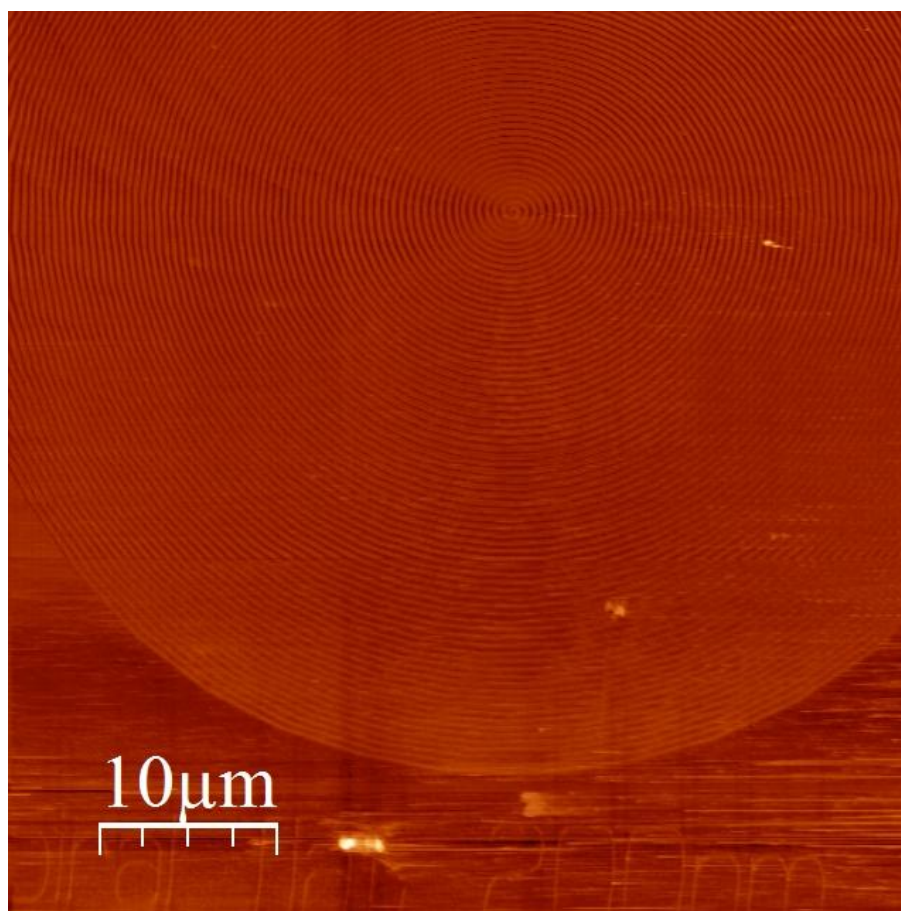


Figure 40 AFM of nano-spiral

5.2 3D Spirals

The next step was to give the sides of the spiral depth variation. In order to create the necessary curvature of the lens, the structure not only needs to take the form of a spiral, but it will also need to be concave. Because the pattern represents is a mold, it is the inverse representation of the object, or a convex shape, that is created in PDMS.

5.2.1 Dose Factor

A critical part of the 3D process is to understand the dose-to-depth relationship of the PMMA PR. The curve for partial development is not given by the manufacturer; it must be empirically determined. This is done using an experimental structure with different dosing, which allows the remaining PR to be measured. The structure is 100 squares that are each 10 nm by 10 nm. They are all separated by no exposure, so there is a good step reference from the substrate to the bottom of the dosed area. This allows easy identification of the depth without concern about planarizing the AFM scan. The resulting measurements help form a dose curve, as shown in Figure 41.

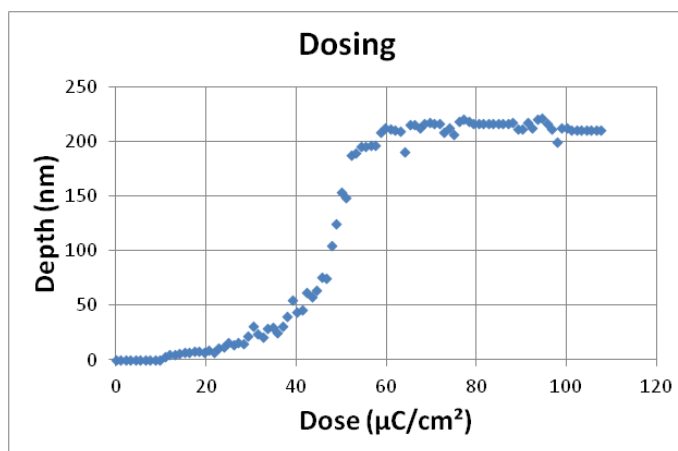


Figure 41 Dose depth curve from nano-scale tests

5.2.2 3D Micro-spiral

Due to the complexity of the required radial dose increase, an image was chosen to convert to the pattern, instead of using the GDS pattern directly. GIMP was used to create the image from which the GDS will be converted. The image started at a 256 x 256 pixel resolution. A radial gradient starting from the center (128,128) from black to white was created in the image. A spiral shape was then used to mask parts of the radial gradient, so that there was no change in the spacing between the arms of the spiral. The image was then exported and run through DOE. Figure 42 shows the depth profile of a spiral with varying depths in the arms. The 3D image of the same spiral is shown in Figure 43.

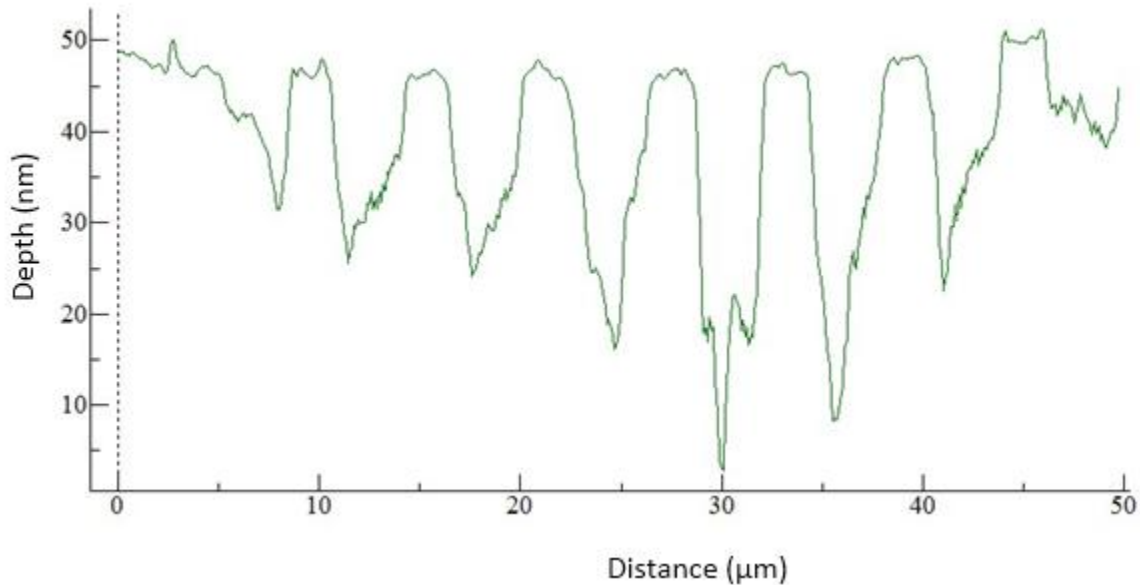


Figure 42 Depth profile of a micro-spiral

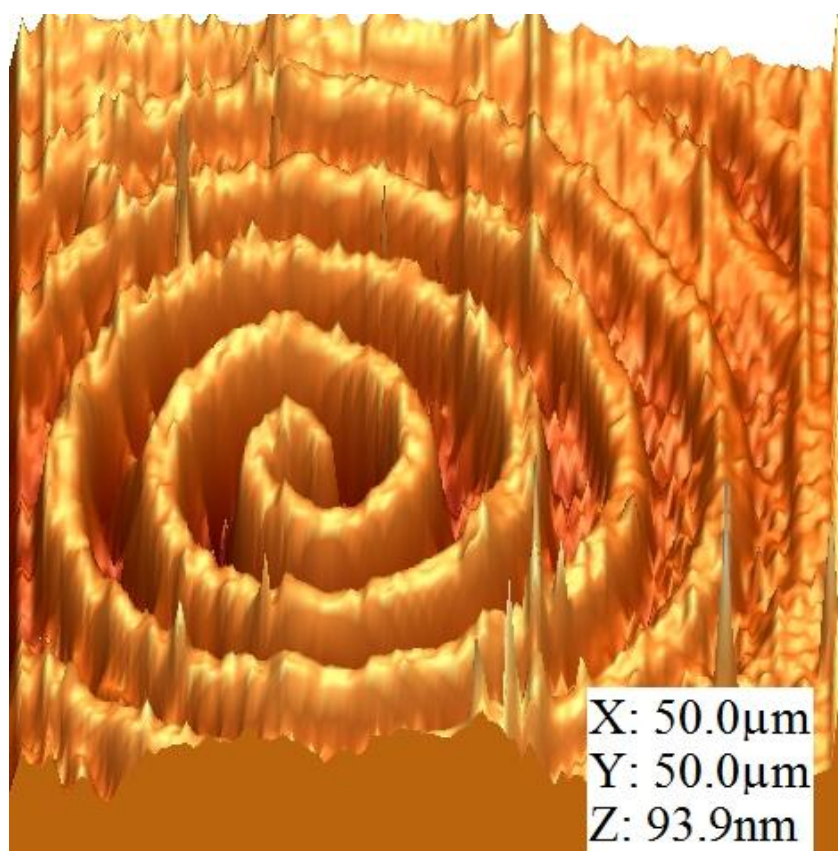


Figure 43 AFM scan of a micro-spiral represented in a 3D image

5.2.3 3D Nano-spiral

After a satisfactory 3D micro-spiral was fabricated, it was again necessary to scale down the structure. The same structure used in the micro-spiral was scaled down, but was not visible at an 8% dose factor. The best result was at 15% dose factor, but this still resulted in only a maximum 27 nm change in measured depth. Table IV compares the maximum depth change seen at various dose factors. Figure 44 shows the AFM scan of the spiral. Due to limitations of the AFM scanning, it was hard to characterize the profile shown in Figure 45; however, the overall concave trend is still present.

Table IV Nano-spiral dose factor vs. max change in depth

Dose Factor	Max Depth Change
8%	~ 0 nm
10%	15 nm
15%	27 nm
20%	25 nm
25%	20 nm
30%	10 nm

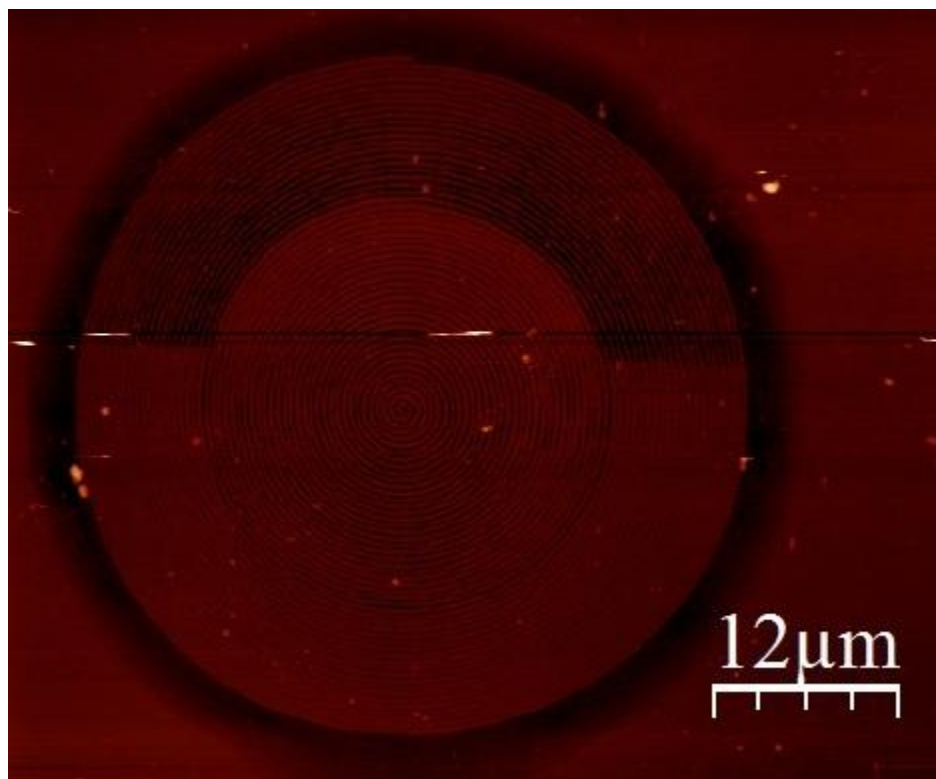


Figure 44 AFM of 3D nano-spiral

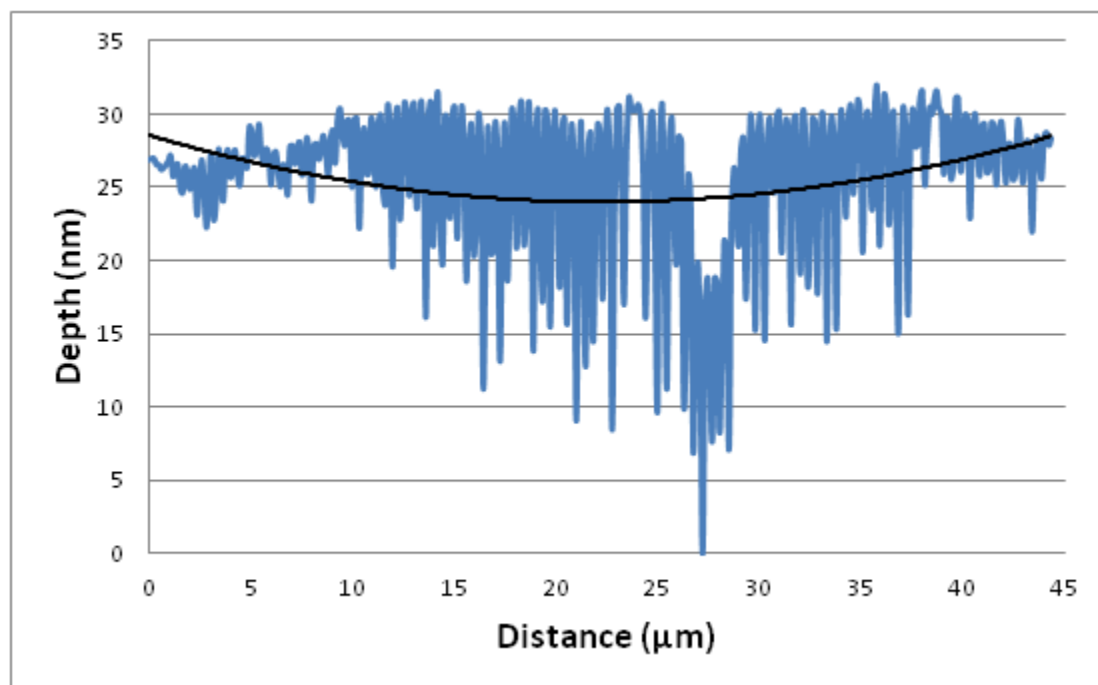


Figure 45 Depth profile with curvature trend of a nano-spiral

5.3 Soft-lithography

PDMS was poured on the micro- and nano-spirals. The PDMS was then peeled from the mold after a curing time of approximately 24 hours. The shape of the structure in the PDMS is the inverse of the original spiral pattern. It is easier to see the peaks, instead of trenches, because they are easier to scan in the AFM.

5.3.1 3D Micro-spiral

The 3D pattern was cleanly transferred to PDMS. There were minor deformations, but the overall pattern matched well. Micro-fabrication can be carried on without much adjustment. Soft-lithography is well developed in this area. The profile of the 3D micro-spiral in PDMS is shown in Figure 46 and an AFM scan of the pattern is shown in Figure 47.

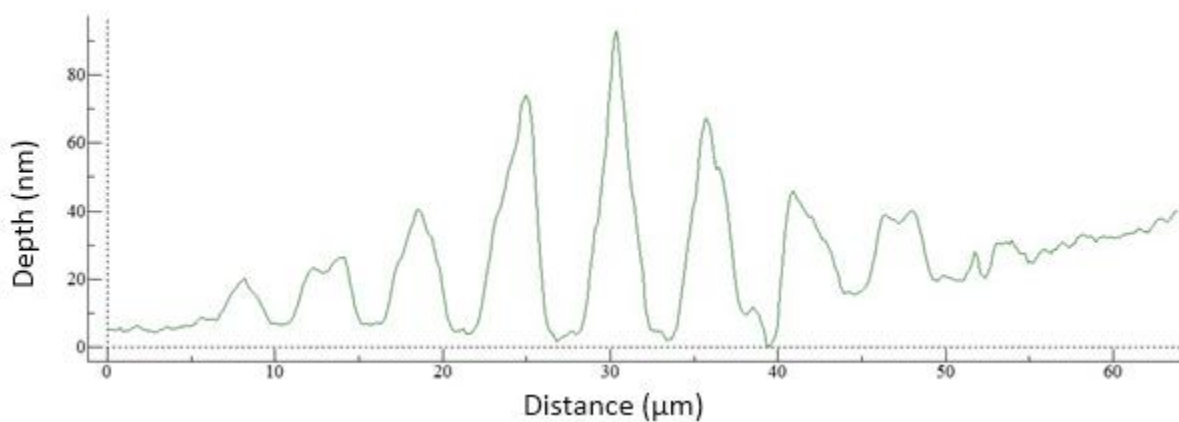


Figure 46 AFM height profile of PDMS 3D micro-spiral

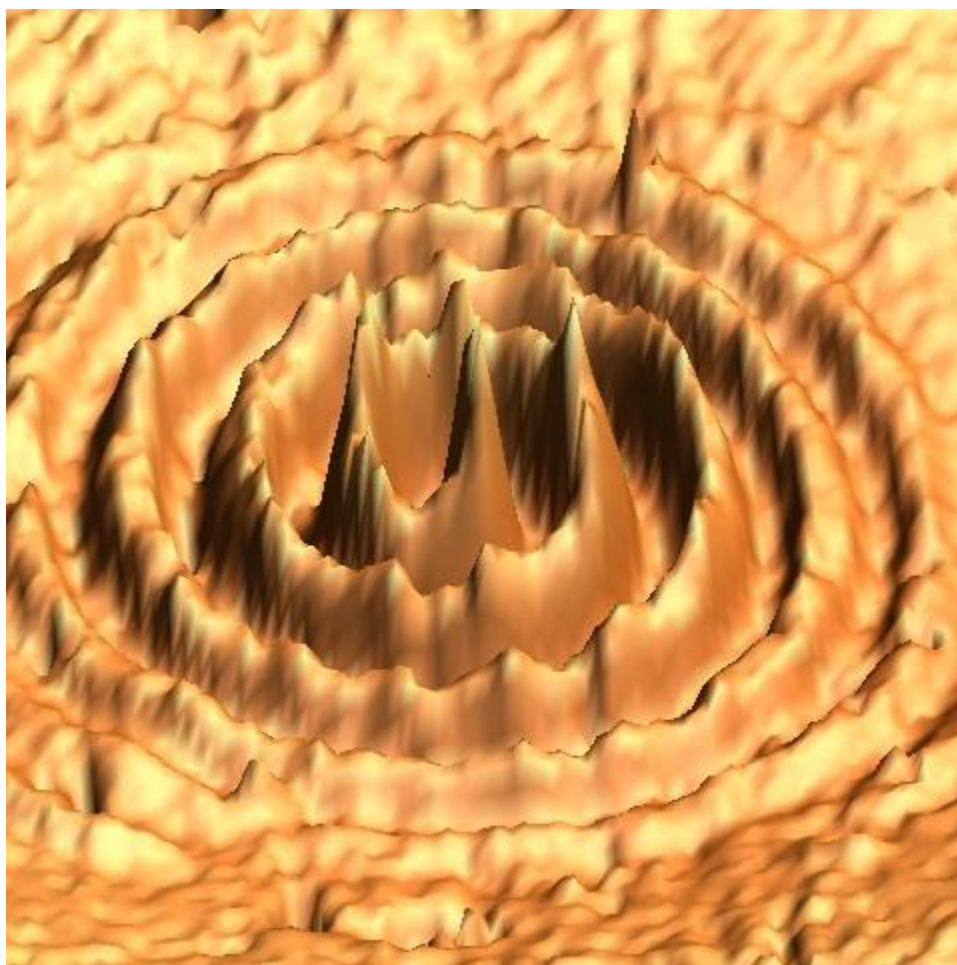


Figure 47 3D image of AFM scan of PDMS 3D micro-spiral

5.3.2 Binary Nano-spiral

There appears to be good spacing between the arms and trenches. The depth of the PDMS closely matches that measured in the PMMA samples. Depth could still be maximized, but this should first be done in the PMMA mold, not in the PDMS. As shown in Figure 48, the depth approached 25 nm in the PDMS samples and the trench spacing was approximately $0.378\text{ }\mu\text{m}$. Figure 49 shows a AFM scan of the same sample.

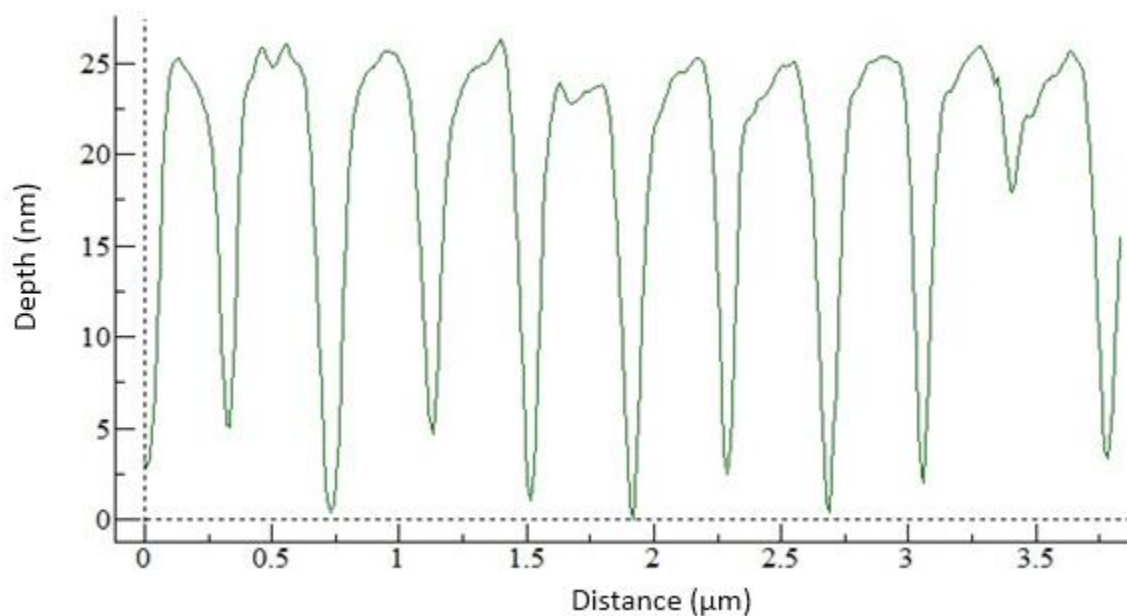


Figure 48 Depth profile of PDMS binary nano-spiral

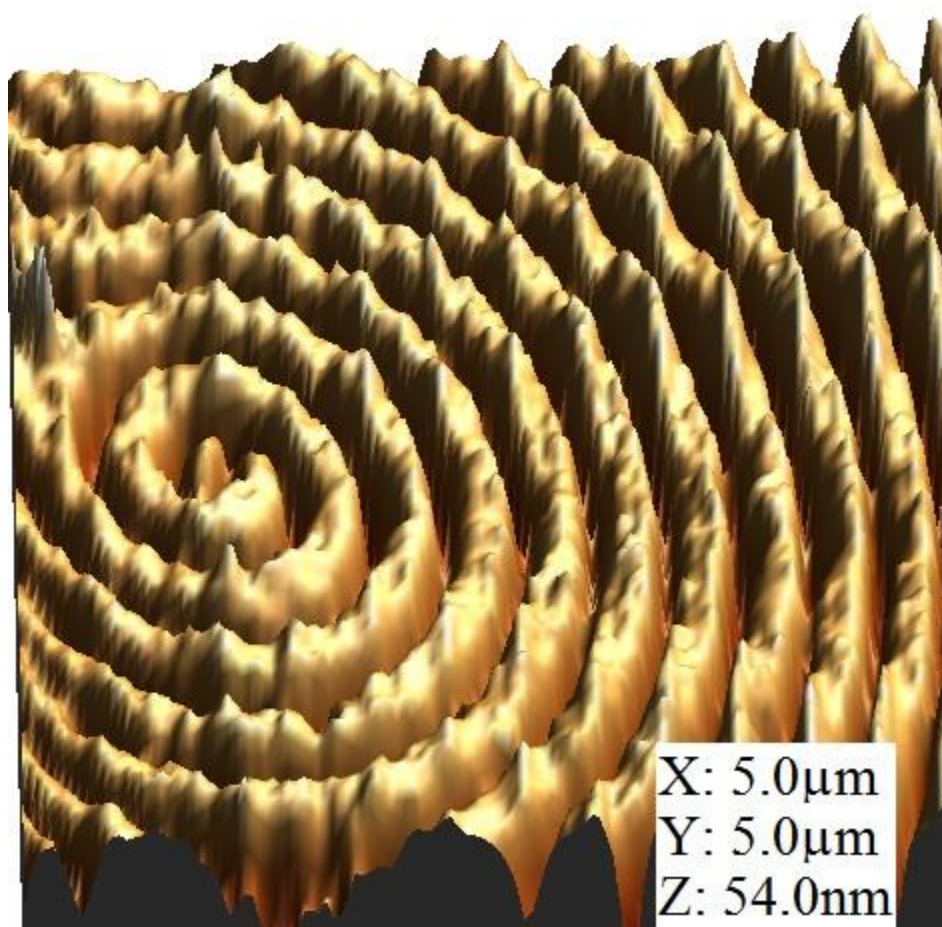


Figure 49 3D AFM image of PDMS binary nano-spiral

5.3.3 3D Nano-spiral

Peeling the PDMS from the 3D nano-spiral did not go as well as with the binary spiral described above. Smaller depths maintained the mold shape, but larger depths towards the center of the mold were deformed and uneven. This could be a factor of the larger depths, or also due to varying curing times or uneven peeling direction and speed. Further investigation is necessary to determine if different mixtures of PDMS, heating or adhesion prevention are helpful in reducing these deformities. Figure 50 shows the extent of deformation from the peeling process, yet the depth profile is not very meaningful. Instead, the SEM image identified as Figure 51 further shows the deformation of the PDMS structure.

Because PDMS is not inherently conductive, it would charge in the SEM. In order to avoid this, the PDMS samples were coated in 2 nm of silver. The metal coating was done on the face side of the sample, and conductive glue was used for the back and sides of the sample to connect it to the sample stage and complete the path to ground. However, charging effects are still evident in the figure.

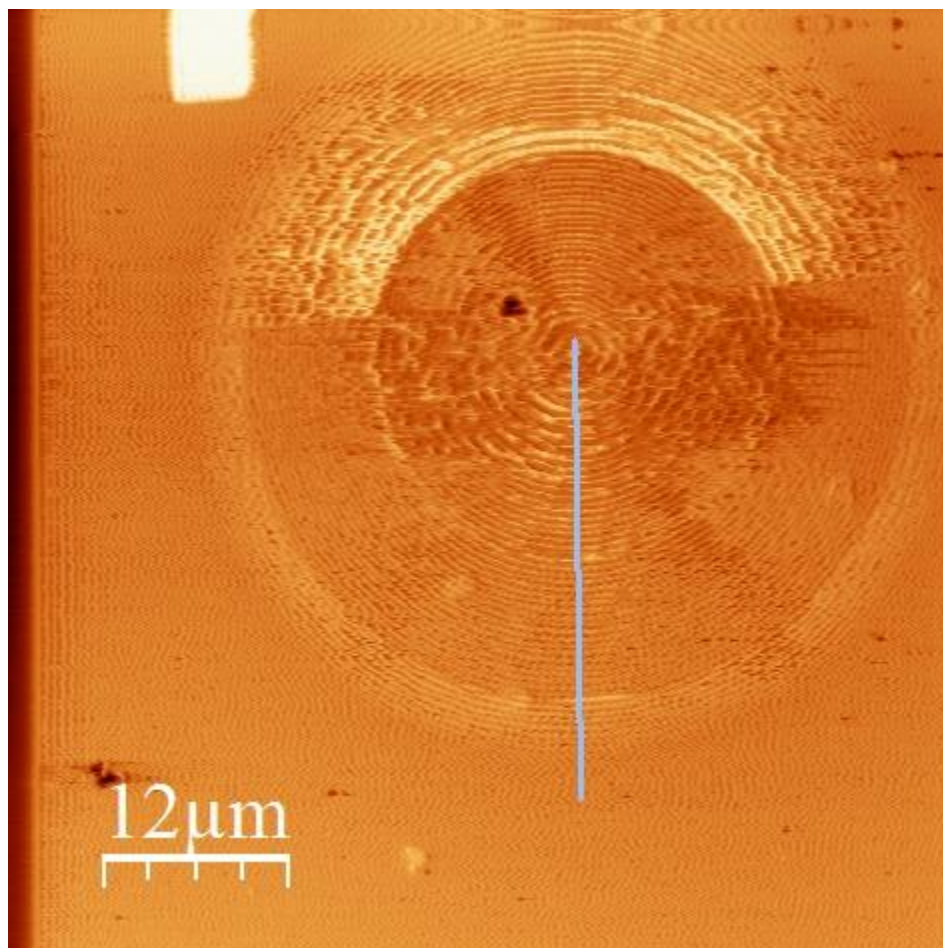


Figure 50 AFM of PDMS 3D nano-spiral

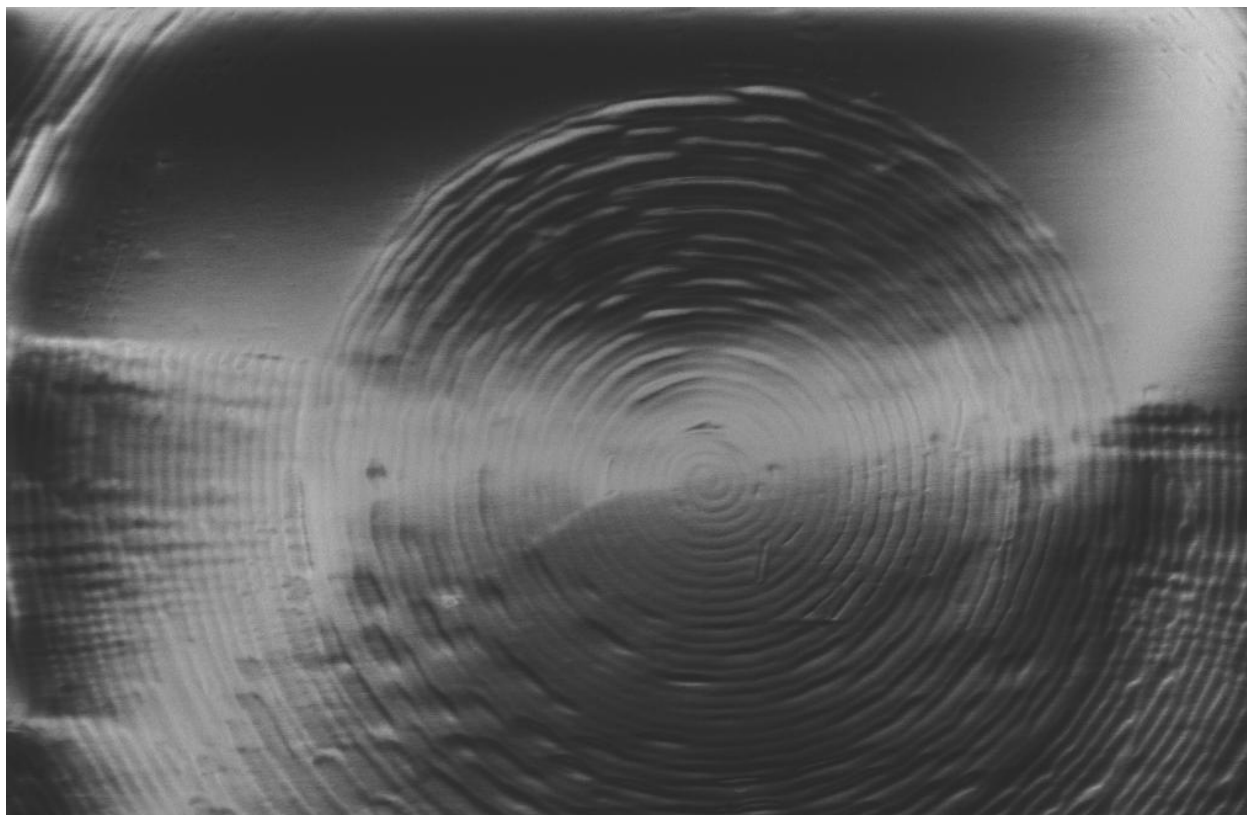


Figure 51 SEM image of PDMS 3D nano-spiral

5.4 Larger Patterns

For all of the previous patterns discussed so far, the write-field was set at 100 μm , and the entire pattern was less than 100 μm by 100 μm . For larger patterns, the write-field, or magnification, was changed to 1000 μm . This allows larger patterns to be written without stage movement and stitching, such as in Figure 52.

The image-to-pattern conversion method was still used. The exact same image in fact was enlarged by increasing the physical size per pixel. This is evident by the pixelation in the background of the image, which is shown in Figure 53. One can see the sharp difference in depths. These are most likely due to the fracturing of different 'colored' areas from the image creation process. A smoother structure would require a larger image that would increase fracturing time.

The write-field size of 1000 μm is the largest available on the Raith. Patterns any larger than the write-field would require separate exposures and subsequent stitching. Due to the fact that a pattern is scanned properly in the write-field, there is no worry about any other writing errors. If the pattern was exposed well for one write-field, it should be fine for the others. The only errors which must be accounted for are the ones in write-field alignment. Another complication due to writing larger patterns is the speed limitation of EBL. Write time becomes the most necessary to optimize. Typical writing times for single write-field of 100 μm were around 2 to 4 hours and 12 to 24 hours for 300 μm by 300 μm on a 1000 μm write-field.

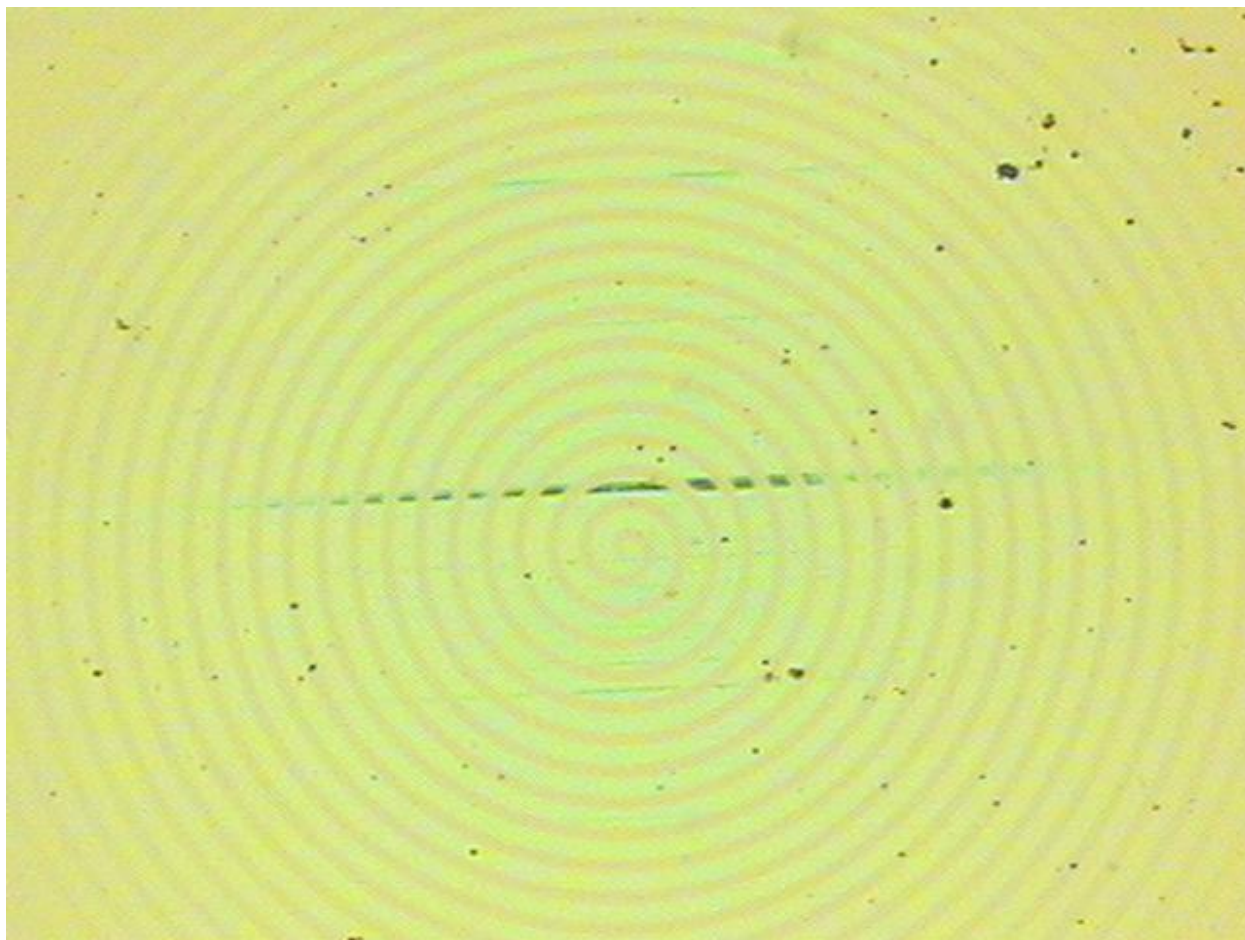


Figure 52 Optical microscope image of a large micro-spiral

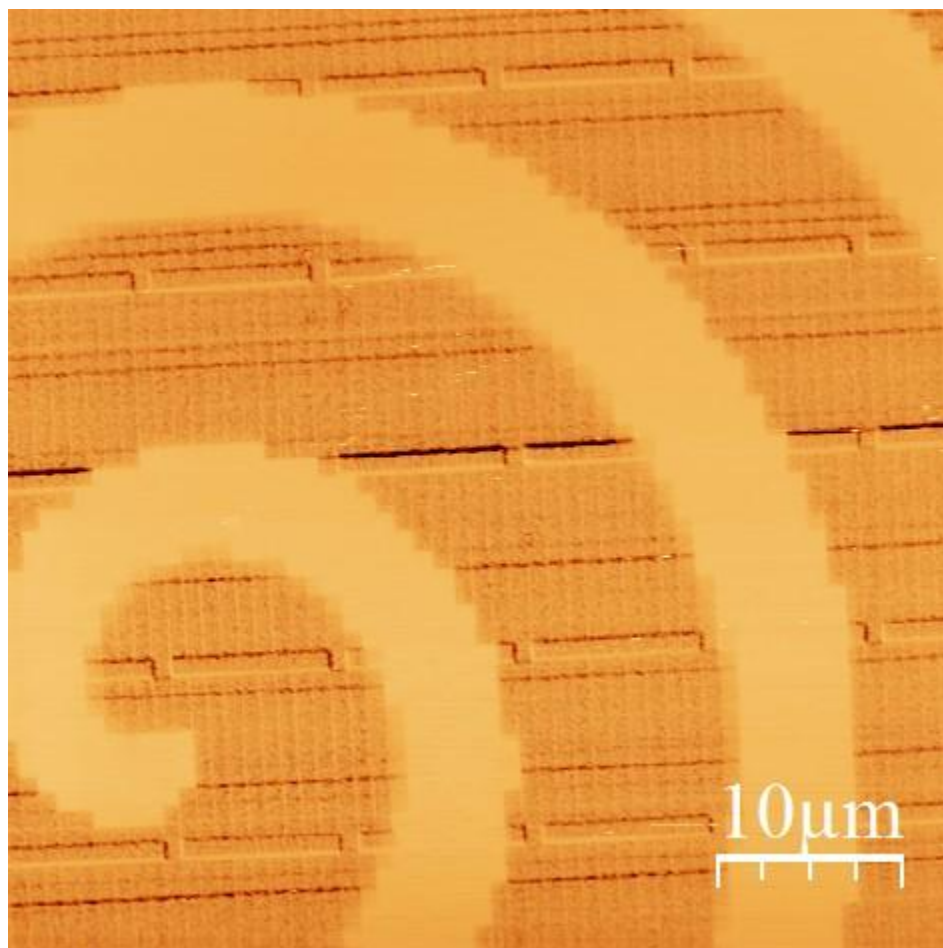


Figure 53 AFM image of a large micro-spiral

5.5 Proximity Correction

Due to its size and nature, the proximity effect did not seem to be detrimental to the fabrication. The overall distortions of the proximity effect would need to be analyzed in the total optical quality of the lens once a functioning prototype is created. As with any micro and macro fabrication process, a maximum defect density would need to be established. Analysis and determination of optical quality and acceptable defects was not performed in this research. However, in short analysis, defects, which are normally on the scale of several nanometers (10 nm), are up to 30 times below the wavelength of visible light. Therefore, individual defects may not be a problem and only larger defects, or clusters of errors, would present a challenge. In the end, proximity correction is probably only necessary for dense circuitry and smaller lenses where defects would be functionally problematic.

5.6 Thermal Reflow

Heating samples to the glass transition temperature (T_g) will melt the PMMA PR and allow it to reflow. This can be used to clean up sharp peaks in the image and final pattern. “Stair-stepped” patterns were made to test the reflow effects on various dosed regions. Samples were heated directly on a hot plate at 120 °C for 5 minutes between each measurement. Analysis of surface roughness of controlled surfaces makes it easier to measure the change due to thermal reflow.

The surface roughness change, shown in Figure 54, corresponds to the softening of a structure. Peaks begin to decrease by melting into surrounding areas, and the overall height is reduced until the area is planar. The root mean squared (RMS) roughness¹ continued to decrease from 13.8 to 9.6 to 8.2. The requirements for roughness were not calculated for this project; however, in general, it should be 20-30 times below the minimum feature size [94].

¹ $R_{RMS} = \sqrt{\frac{1}{n} \sum_{i=1}^n y_i^2}$

The overall softening of the surface is apparent in the profile of the selected spiral structure. For these tests, the temperature was increased 180 °C in order to save time on the larger structure. The images below are directly from the AFM measurement without averaging. Figure 55 is the spiral without any reflow. Figure 56 and Figure 57 represent 5 and 10 minutes of reflow, respectively. Treatment for 10 minutes resulted in a smooth and clean profile. After the processing, the height difference is still well maintained. This is best seen in Figure 58.

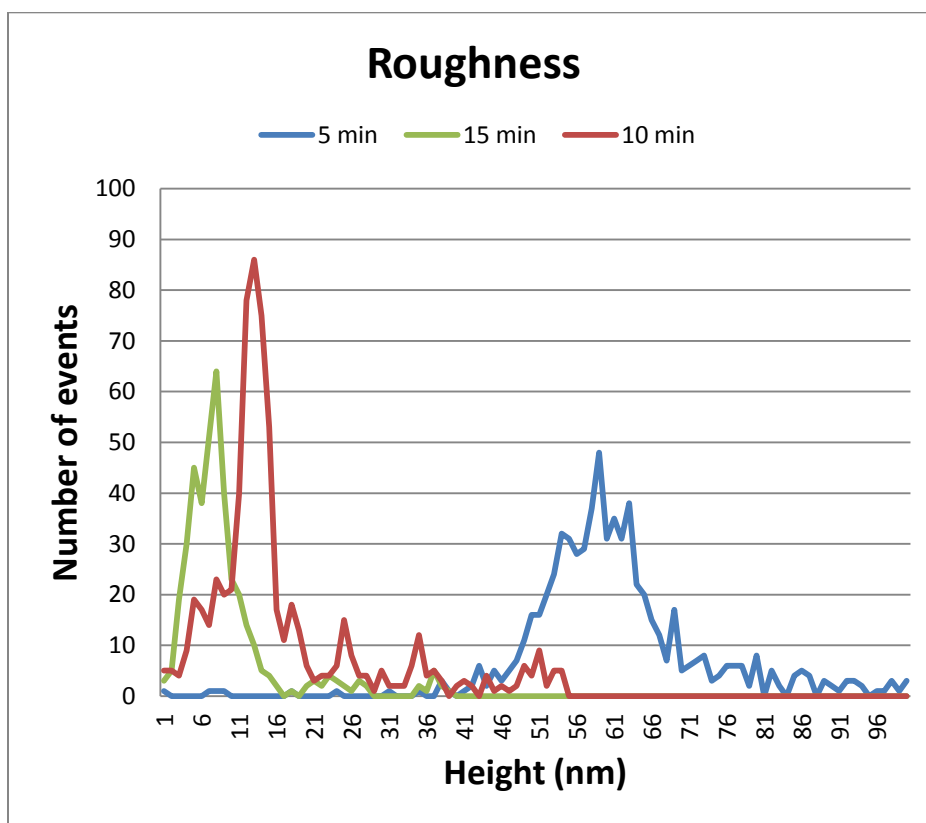


Figure 54 Surface roughness from thermal reflow sample analysis

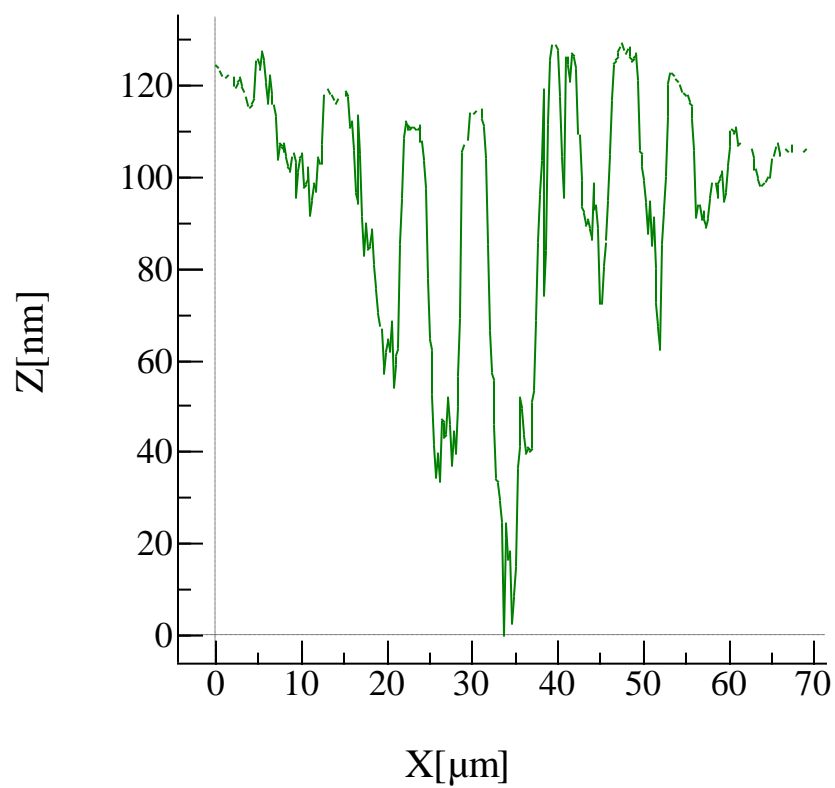


Figure 55 Depth profile for spiral after 0 minutes of thermal reflow

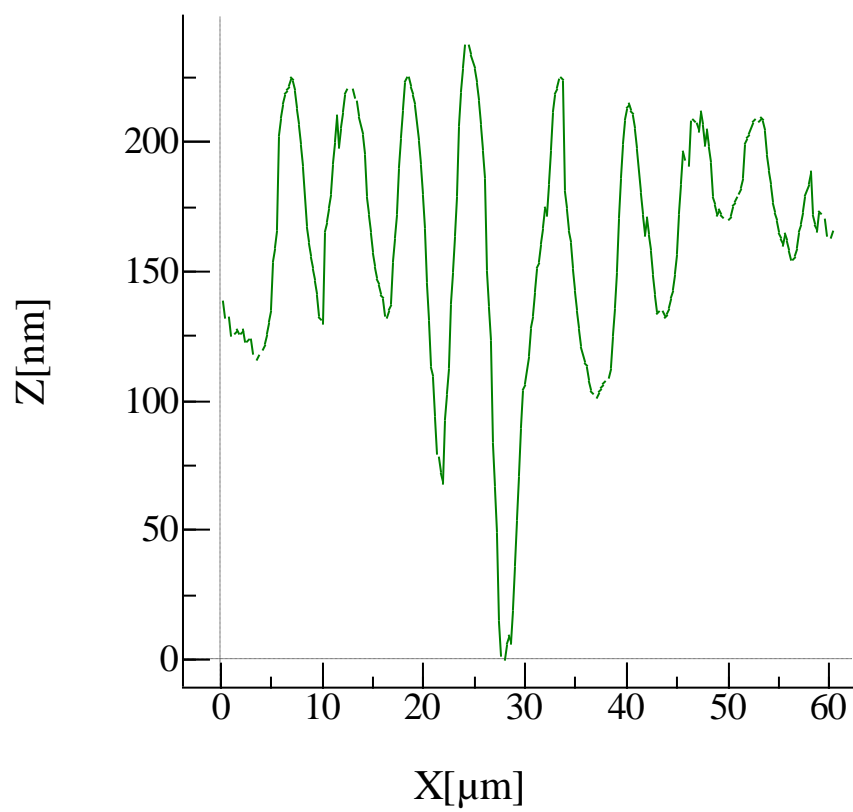


Figure 56 Depth profile for spiral after 5 minutes of thermal reflow

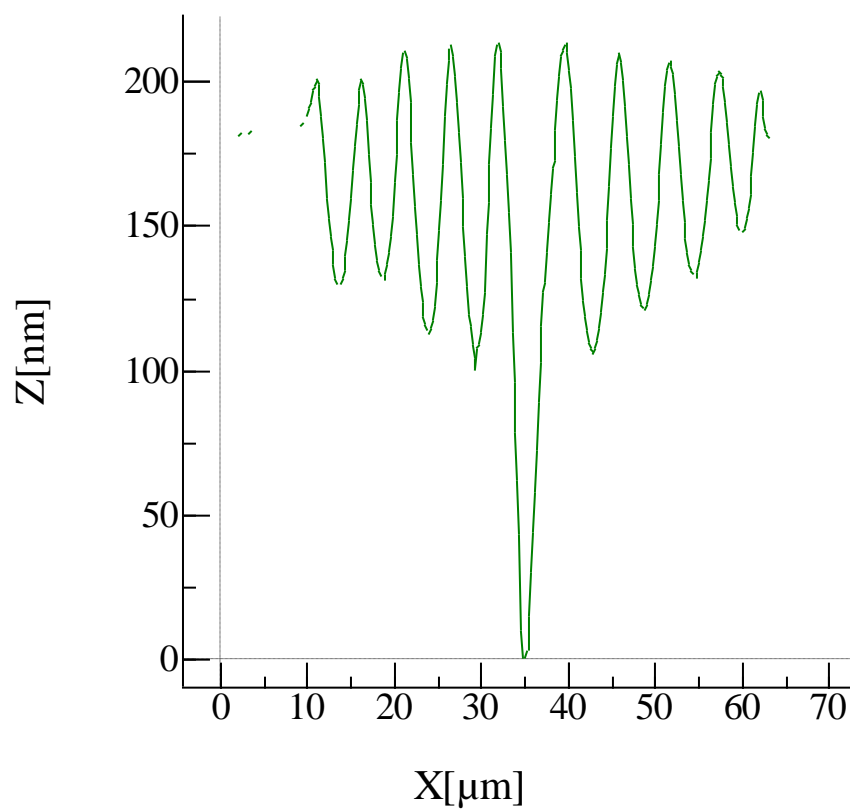


Figure 57 Depth profile for spiral after 10 minutes of thermal reflow

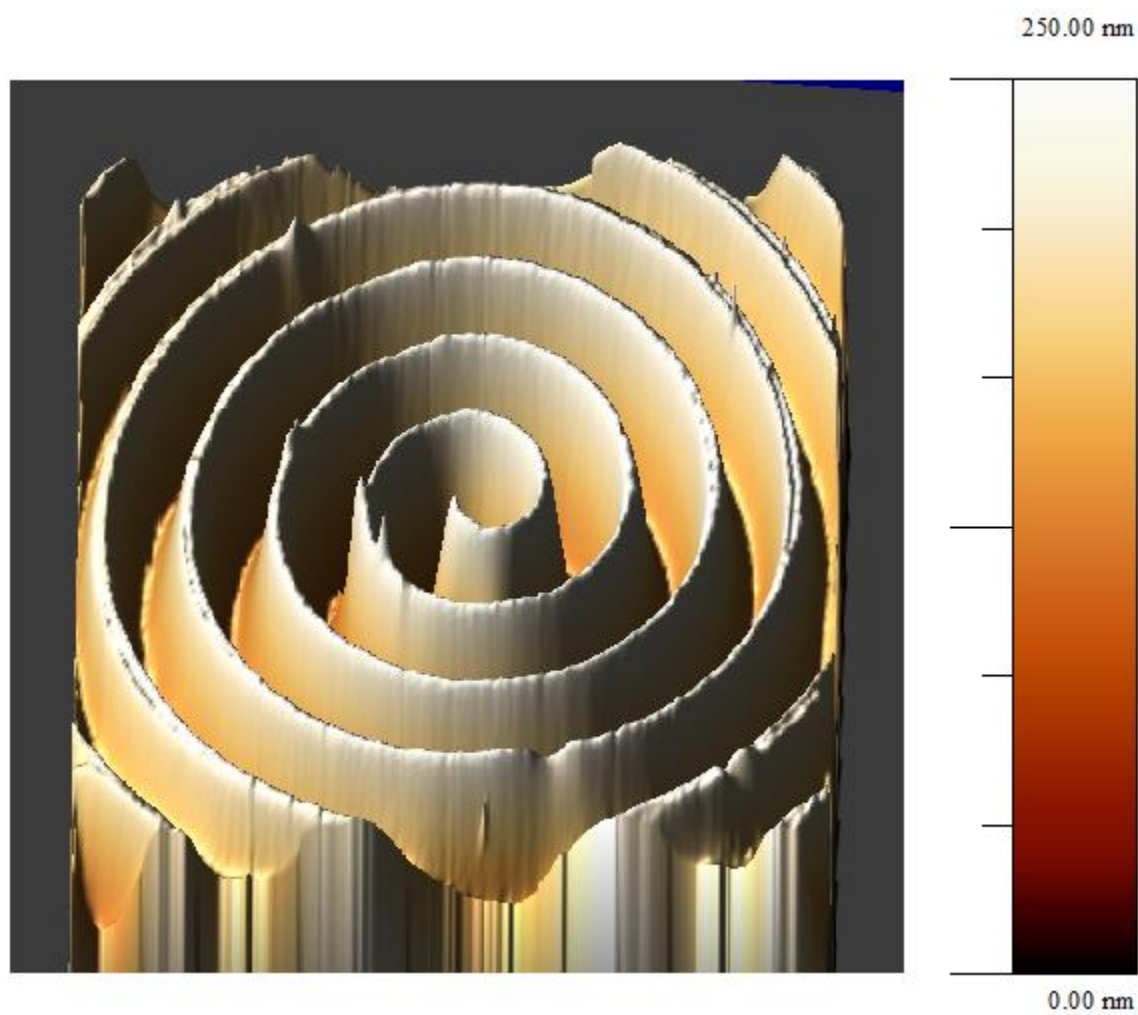


Figure 58 3D AFM image of spiral after 10 minutes of reflow

5.7 Conclusion

In short, this project can be considered a success; several samples showed proof of concept in different areas. EBL was shown to successfully write 3D patterns, which would otherwise be impossible with binary lithography techniques. Even if it was possible to use binary lithography, there would be alignment problems between the process steps. Grayscale lithography eliminates this by writing multiple “layers” in one step. The project also demonstrated that a 3D pattern can be successfully transferred to flexible substrates using soft lithography.

5.7.1 Analysis

In this project, micrometer and nanometer scale patterns of a 3D lens mold and structure were made. Lateral dimensions met design specs, and depth was maximized in the PR. The PDMS structures were not of the quality desired; however, the micrometer scale version can be considered a success, even though there is room for improvements. The nano-scale lens will require additional enhancement, but it should be noted that the proof of concept has not been disproven, and the overall design still has promise.

5.7.2 Improvements

There are several improvements that can be considered for future research. First and foremost is the improved understanding and determination of the 3D contrast of the PR. Contrast curves were determined for different dosing of the PR, but there are opportunities to fine tune contrasting, such as maximizing depth and dose control. Remaining questions include:

- Over what area can a minimum amount of depth be written?
- Are there modifications to the PMMA that can increase the depth control?
- Can and should the process be divided into multiple layers of PR and exposure?

Even without mastering exposure, changes in the design could still lead to improvement. It was learned that at certain scales image conversion resulted in an overly complicated pattern that required excessive write times. Enlarging the pattern from the image will result in pixilation, because of its bitmap nature, but to what extent is this an acceptable quality sacrifice in favor of more efficient lens manufacture?

Acceleration potential (AP) is another value that can be adjusted. The default value of 10kV is suggested by many texts, including the Raith guide. In theory, higher AP gives sharper beam size but increases back-scattering. The Raith has a range of 0.2 to 30 kV, so it would be helpful to characterize how the system handles increasing AP. Remaining questions include:

- What is the best AP for the pattern?
- Does increased AP make higher resolution patterns?
- Does increased current speed up writing time?
- Does back-scattering cause problems with the pattern?
- Is there any damage to the PR?

The aperture of 30 μm is suggested for general patterns. [106] Larger apertures allow more of the beam through, which increases beam size and overall beam current. Increased current lowers dwell time requirements. The following questions need to be answered:

- Does increasing beam current speed up writing time?
- Does increasing beam diameter cause lower resolution?

As stated before, the electron beam can be electromagnetically steered through different sized apertures (up to 6 on the Raith). Theoretically, it is possible to automatically change aperture during the writing of a pattern in order to balance speed and precision for different areas. A combination of processes could then be used. With thermal reflow, it may be possible to approximate only parts of the image to speed up exposure. Then, the image can be softened by reflow.

Working distance affects the depth of field due to the angle of approach on the sample. Further working distance should give a cleaner and deeper exposure. This may be applicable to lines, dots and spaces, but other questions about how working distance affects image quality of the pattern must be answered.

Magnification, or write-field, can also be adjusted on the EBL. Smaller write-fields should allow for more control and detail. Remaining questions include:

- How does magnification of the write-field affect the beam deflection performance?
- Are 1000 μm write-fields quicker for larger patterns?
- Is the resolution of the pattern affected by write-field size?

The soft-lithography portion of this project also requires further research and improvement. Although larger channels can easily be transferred to PDMS, the smaller (nano-scale) channels were more difficult. Design and shape, adhesion preventers and curing times could all affect the success of the smaller features. Also, when the lens is produced, the flexibility of the pattern will also need to be controlled, possibly by using mixture ratio, curing times or temperature.

5.7.3 Limitations

Ultimately, there are several limitations to the improvements in methods and design. One of the improvements to the design is the use of vector format in the GDS file. Limitation is imposed by the layout software. It is quite difficult to draw complicated 3D shapes using the poly functions the software has available. For example, automating the increase in dose and size of various portions at the same time cannot be done, so most of it performed manually. There is the ability to write macros for the software, but the exact use was not determined in this research. Also, with some of the larger patterns in the layout software, errors such as “too many polys” and “cannot fracture” are encountered. Therefore, a different layout is necessary or the design must be drawn specifically in a way that is

compatible with the software. However, time was not available on this project to focus on all of these software aspects.

The biggest limitation of EBL is the long process time. Typical beam current is on the order of 10^{-9} (nA). Assuming the necessity of 10^{-3} C/cm² for exposure over a 1 cm² area, the resulting write time would be around 10^6 seconds or about 12 days.

It has been demonstrated that the patterns can be generated through these methods; next, the scaling must be increased. A time requirement of 4 - 7 days to produce a full-scale model sounds absurd compared to the speed of regular photolithography, but it is not totally unacceptable. The patterning is only done to create “masks”. These masks are used in X-ray lithography to reproduce the true 3D mold structure. The real production is in the soft lithography process. As soon as various sized molds are produced, the production speed of lenses can be increased considerably. Therefore, the speed of the EBL, at present, does not make this design infeasible.

However, the process would be greatly improved if speed was increased. This is one of the many reasons EBL is not used in mass production, such as microprocessors. One way to improve speed in EBL is using multi-beams. The company Multibeam has a technology called Complementary EBL (CEBL), in which arrays of e-beam columns are constructed in modules. Electrostatic lens are used to reduce the footprint of each column. This allows them to have 2D arrays of 100 columns to expose 300 mm wafers, and they claim to be able to process 5 to 10 wafers per hour (WPH). [GK] In clustering tools, which have multiple modules, they can reach 50 to 100 WPH. There are other parallel EBL systems, such as from MAPPER Lithography. These systems use MAPPER technology with over 10,000 parallel electron beams to write on the surface. [115] These systems are not just in the research phase; they are also currently being sold. Taiwan Semiconductor Manufacturing Co. Ltd. (TSMC) is set to receive the Matrix 13,000 from MAPPER. [116]

Though, these systems are most likely designed for binary patterning of repeat patterns. It would be interesting to see if 3D patterning could be implemented on systems like these and how much of a speed increase they could offer. Advancements such as the MAPPER products make EBL technology even more attractive for use in mass nano-fabrication.

5.7.4 Alternative Additional Processing

The fabrication of a focusing Fresnel lens is not the only possibility in this process. With only a few additional steps via LIGA, a true 3D lens can be produced with the dimensions of a natural lens. First, the PMMA mold is covered in gold. Next, electroplating fills in the channels completely with gold. Last, this is then used as a mold in X-ray lithography. With parallel X-rays, the 3D mask patterns another PR. Depending on the thickness of the gold section, it will determine how deep the X-ray exposes the PR. In this process, the contrast can be amplified; therefore, a mask which is on the order of 250 – 500 nm can be translated into mm or even cm thickness. Again, PDMS can then be formed by the final mold. This whole process is diagrammed in Figure 59.

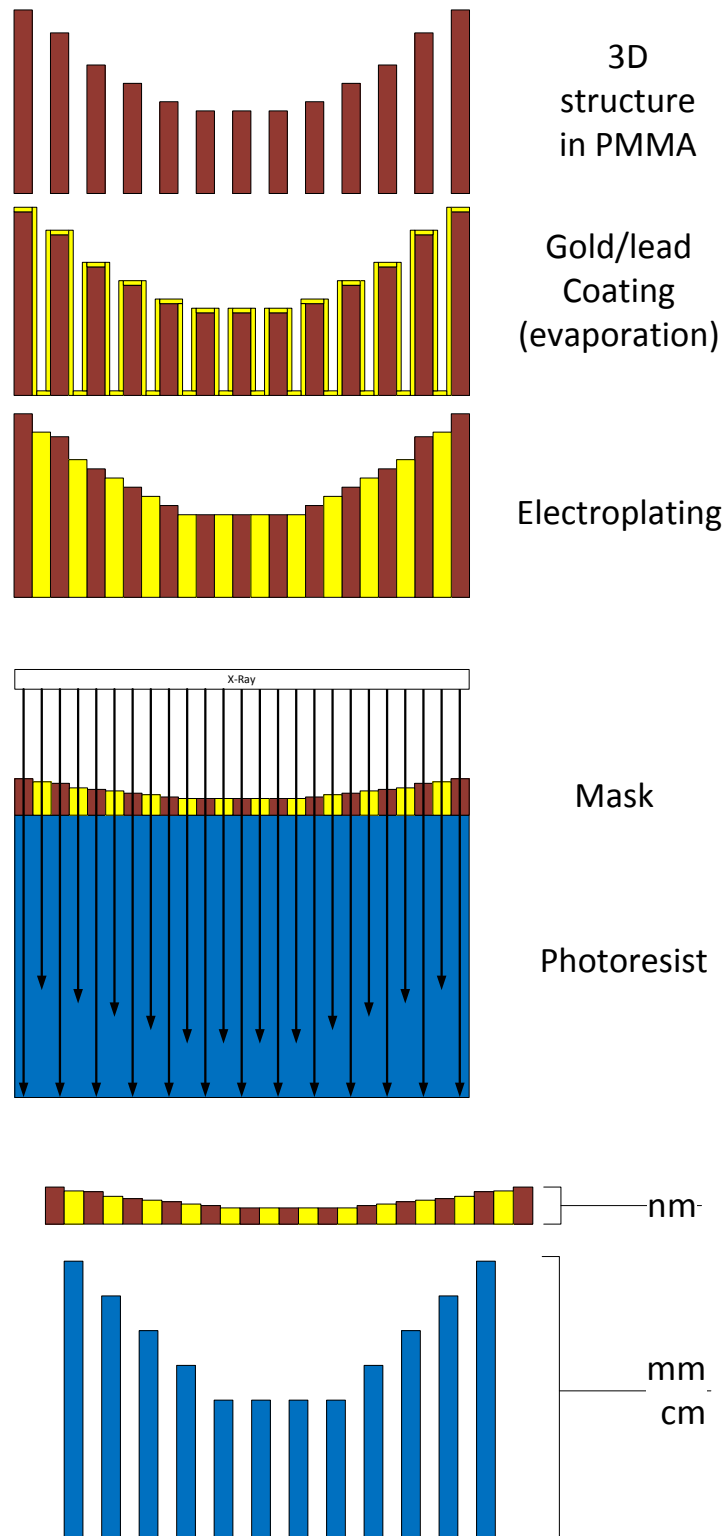


Figure 59 Overview of the LIGA process used in creating a 3D lens.

5.7.5 Future Research

This research is only the first step. Each process step involves individual proofs of concept, all of which require in-depth exploration and development. Nothing presented in this research showed any evidence that is destructive to the design or fabrication process. As such, work on this project should continue. Several improvements, mentioned in the previous section, should be taken into account when continuing this research. Once a more efficient design is finalized, a full-scale mold should be written and a complete lens should be molded. The real determination of feasibility will come in the optical testing of an actual device. The focal power of the device can be correlated with the compression, or muscle power, of the lens. Testing will show how the design compares in practice to what is required to match the functionality of the natural lens. Further testing will also take place in vivo of rabbit and mouse models. If and when the design concept is proven in practice, there can be more development on the mass-scale production.

WORKS CITED

1. *Global initiative for the prevention of avoidable blindness*. 1997, World Health Organization: Geneva.
2. Murray, C.J.L. and A.D. Lopez, *Global mortality, disability, and the contribution of risk factors: Global Burden of Disease Study*. The Lancet, 1997. **349**(9063): p. 1436-1442.
3. Komolafe, O.O., et al., *Visual impairment from age-related cataract among an indigenous African population*. Eye, 2009. **24**(1): p. 53-58.
4. Habiyakire, C., et al., *Rapid Assessment of Avoidable Blindness and Cataract Surgical Services in Kilimanjaro Region, Tanzania*. Ophthalmic Epidemiology. **17**(2): p. 90-94.
5. Athanasiov, P.A., et al., *Cataract surgical coverage and self-reported barriers to cataract surgery in a rural Myanmar population*. Clinical & Experimental Ophthalmology, 2008. **36**(6): p. 521-525.
6. Muñoz, B. and S.K. West, *Blindness and visual impairment in the Americas and the Caribbean*. British Journal of Ophthalmology, 2002. **86**(5): p. 498-504.
7. Shah, S.P., et al., *Preoperative visual acuity among cataract surgery patients and countries' state of development: a global study*. Bulletin of the World Health Organization. **89**: p. 749-756.
8. Jose, N.K., et al., *Screening and surgical intervention results from cataract-free-zone projects in Campinas, Brazil and Chimbote, Peru*. International Ophthalmology, 1990. **14**(3): p. 155-164.
9. The Eye Diseases Prevalence Research, G., *Prevalence of Cataract and Pseudophakia/Aphakia Among Adults in the United States*. Arch Ophthalmol, 2004. **122**(4): p. 487-494.
10. Foster, A., C. Gilbert, and J. Rahi, *Epidemiology of cataract in childhood: a global perspective*. Journal of cataract and refractive surgery, 1997. **23 Suppl 1**: p. 601-4.
11. You, C., et al., *Visual Impairment and Delay in Presentation for Surgery in Chinese Pediatric Patients with Cataract*. Ophthalmology. **118**(1): p. 17-23.
12. Hiratsuka, Y., et al., *Cost-effectiveness of cataract surgery in Japan*. Japanese journal of ophthalmology. **55**(4): p. 333-42.
13. Ferris, F.L., III and J.M. Tielsch, *Blindness and Visual Impairment: A Public Health Issue for the Future as Well as Today*. Arch Ophthalmol, 2004. **122**(4): p. 451-452.
14. Ram, J., et al., *Outcome of cataract surgery with primary intraocular lens implantation in children*. British Journal of Ophthalmology. **95**(8): p. 1086-1090.
15. David F. Chang, H.B.-M., I. Howard Fine, Howard V. Gimbel, Douglas D. Koch, Stephen S. Lane, Richard L. Lindstrom, Thomas F. Neuhann, Rober H. Osher, Saunders Elsevier, *Cataract Surgery*. 3 ed. 2010, Duxbury, MA: Elsevier Inc.

WORKS CITED (continued)

16. Kuszak, J.R., J.G. Sivak, and J.A. Weerheim, *Lens optical quality is a direct function of lens sutural architecture*. Investigative Ophthalmology & Visual Science, 1991. **32**(7): p. 2119-29.
17. Kuszak, J.R. and K.J. Al-Ghoul, *A Quantitative Analysis of Sutural Contributions to Variability in Back Vertex Distance and Transmittance in Rabbit Lenses as a Function of Development, Growth, and Age*. Optometry & Vision Science, 2002. **79**(3): p. 193-204.
18. Edward, et al., *Anatomy, development, and physiology of the visual system*. 2003, New York, NY, ETATS-UNIS: Elsevier. 299.
19. Taylor, V.L., et al., *Morphology of the normal human lens*. Investigative Ophthalmology & Visual Science, 1996. **37**(7): p. 1396-410.
20. Antunes, A., et al., *Analysis of the healthy rabbit lens surface using MAC Mode atomic force microscopy*. Micron, 2007. **38**(3): p. 286-290.
21. Roberto Pineda II, C.A., Sherleen H. Chen, Jae Yong Kim, *Essentials of Cataract Surgery*, ed. B.A. Henderson. 2007, Thorofare, NJ: SLACK Inc.
22. *Cataract Surgery from Routine to Complex: A Practical Guide*. 2011, Thorofare, NJ 08086: SLACK Inc.
23. Amar Agarwal, S.J., *Color Atlas of Ophthalmology: The Quick Reference Manual for Diagnosis*. 2010: Thieme Medical Publishers, Inc.
24. Hayano, S., *Intraocular Lens Implantation*. 1991, APACRS: LIM Lecture.
25. I. Howard Fine, M.M.P., MD, FACS; Richard S. Hoffman, MD, *Refractive lens surgery*. Vol. 2. 2005, Berlin Heidelberg: Springer-Verlag
26. Jayapratha, N., *Implantable Intraocular Lens With Changing Focal Distances*, in *Electrical and Computer Engineering*. 2011, University of Illinois at Chicago: Chicago. p. 64.
27. Banh, A., et al., *The lens of the eye as a focusing device and its response to stress*. Progress in Retinal and Eye Research, 2006. **25**(2): p. 189-206.
28. David J. Apple, M.D., *Sir Harold Ridley And His Fight For Sight*. 2006: SLACK Incorporated.
29. Aliñá, J.L., D.P. Piñero, and A.B. Plaza-Puche, *Visual outcomes and optical performance with a monofocal intraocular lens and a new-generation single-optic accommodating intraocular lens*. Journal of Cataract & Refractive Surgery. **36**(10): p. 1656-1664.
30. Aliñá, J.L., et al., *Visual outcomes and optical performance of a monofocal intraocular lens and a new-generation multifocal intraocular lens*. Journal of Cataract & Refractive Surgery. **37**(2): p. 241-250.

WORKS CITED (continued)

31. Ali³, J.L., et al., *Microincision cataract surgery with toric intraocular lens implantation for correcting moderate and high astigmatism: Pilot study*. Journal of cataract and refractive surgery. **36**(1): p. 44-52.
32. Statham, M., A. Apel, and D. Stephensen, *Comparison of the AcrySof SA60 spherical intraocular lens and the AcrySof Toric SN60T3 intraocular lens outcomes in patients with low amounts of corneal astigmatism*. Clinical & Experimental Ophthalmology, 2009. **37**(8): p. 775-779.
33. Felipe, A., et al., *Residual astigmatism produced by toric intraocular lens rotation*. Journal of Cataract & Refractive Surgery. **37**(10): p. 1895-1901.
34. Koopmans, S.A., et al., *Accommodative Lens Refilling in Rhesus Monkeys*. Investigative Ophthalmology & Visual Science, 2006. **47**(7): p. 2976-2984.
35. *Gates Prevention of blindness in infants and children due to congenital cataract*: Chicago.
36. Menapace, R., et al., *Accommodating intraocular lenses: a critical review of present and future concepts*. Graefe's Archive for Clinical and Experimental Ophthalmology, 2007. **245**(4): p. 473-489.
37. Langenbucher, A., et al., *Cardinal points and image-object magnification with an accommodative lens implant (1 CU)*. Ophthalmic and Physiological Optics, 2003. **23**(1): p. 61-70.
38. Qiao, W., et al., *Bio-inspired accommodating fluidic intraocular lens*. Opt. Lett., 2009. **34**(20): p. 3214-3216.
39. Grendahl, D.T., *Intraocular Lens*, in *Google Patents*, U. States, Editor. 1985: United States. p. 11.
40. Nishimoto, Y., *Variable-focal-length Lens*, in *Google Patents*, U.S.P. Office, Editor. 1986, Canon Kabushiki Kaisha: USA. p. 7.
41. Kern, S.P., *Variable Power Lens System*, in *Google Patents*, U.S.P. Office, Editor. 1986: USA. p. 10.
42. Wiley, R.G., *Micromotor Actuated Adjustable Focus Lens*, in *Google Patents*, U.P. Office, Editor. 1992: USA.
43. Joseph Rizzo, I.J.L.W., Jr, *Intra-ocular Lens System Including Microelectric Components*, in *Google Patents*, U.S.P. Office, Editor. 2000, Massachusettes Eye and Ear Infirmary: USA. p. 5.
44. Conrad-Hengerer, I., et al., *Optimized constants for an ultraviolet light-adjustable intraocular lens*. Journal of Cataract & Refractive Surgery. **37**(12): p. 2101-2104.
45. Administration, U.S.F.a.D. *Medical Devices*. 2011 [cited 2011].

WORKS CITED (continued)

46. Kwok-Hoi Wong, S.A.K., Thom Terwee, and Aart C. Kooijman, *Changes in Spherical Aberration after Lens Refilling with a Silicone Oil*. Investigative Ophthalmology & Visual Science, 2007. **48**(3): p. 7.
47. Nishi, O, and K, *Accommodation amplitude after lens refilling with injectable silicone by sealing the capsule with a plug in primates*. Vol. 116. 1998, Chicago, IL, ETATS-UNIS: American Medical Association.
48. Han, Y.K., et al., *In vitro and in vivo study of lens refilling with poloxamer hydrogel*. British Journal of Ophthalmology, 2003. **87**(11): p. 1399-1402.
49. Koopmans, S.A., T. Terwee, and T.G. van Kooten, *Prevention of capsular opacification after accommodative lens refilling surgery in rabbits*. Biomaterials. **32**(25): p. 5743-5755.
50. Anthony Atala, R.L., James A. Thomson, *Foundations of Regenerative Medicine: Clinical and Therapeutic Applications*. 1 ed. 2010, San Diego, CA: Elsevier, Inc.
51. Nanavaty, M.A., D.J. Spalton, and J.F. Boyce, *Influence of different acrylic intraocular lens materials on optical quality of vision in pseudophakic eyes*. Journal of Cataract & Refractive Surgery. **37**(7): p. 1230-1238.
52. Hu, M.D.L.H.C.M.C.B., *Lubricious, Biocompatible Coatings for Medical Devices*, in *Google Patents*, U.S.P. Office, Editor. 2005, Advanced Medical Optics, Inc.: USA. p. 5.
53. Ionescu, M., et al., *Enhanced biocompatibility of PDMS (polydimethylsiloxane) polymer films by ion irradiation*. Nuclear Instruments and Methods in Physics Research Section B: Beam Interactions with Materials and Atoms. **273**(0): p. 161-163.
54. Preetha, J., et al., *Photodefinable PDMS thin films for microfabrication applications*. Journal of Micromechanics and Microengineering, 2009. **19**(4): p. 045024.
55. Thangawng, A., et al., *An ultra-thin PDMS membrane as a bio/micro–nano interface: fabrication and characterization*. Biomedical Microdevices, 2007. **9**(4): p. 587-595.
56. Kubaloglu, A., et al., *Intraocular lens exchange through a 3.2-mm corneal incision for opacified intraocular lenses*. Vol. 59. 17-21.
57. Chang, D.F., *Silicone IOL biocompatibility* “not all silicone is the same. Journal of cataract and refractive surgery, 2000. **26**(8): p. 1102.
58. Development, B.R. *Integrated Lens Manufacturing: Increasing Productivity and Reducing Costs* 2008 [cited 2011 12/15/11].
59. Colin Fowler, K.L.P., *Spectacle Lenses: Theory and Practice*. 2001: Reed educational and Professional Publishing Ltd.

WORKS CITED (continued)

60. International, D. *DAC ALM Lens Lathe*. 2009 [cited 2011 12/16/11].
61. Heavican, C., *Website form mail from Evan Zaker*, E. Zaker, Editor. 2011: Carpinteria, CA
62. DocShop.com. *IOL Costs*. 2012 [cited 2011 12/17/11]; Available from: <http://www.docshop.com/education/vision/refractive/iol/cost>.
63. Liu, C., *Foundations of MEMS*. 2006, Upper Saddle River, NJ: Pearson Education, Inc. 530.
64. James D. Plummer, M., *Silicon VLSI Technology*. 2000, Upper Saddle River, NJ: Prentice Hall, Inc.
65. Afromowitz, M., *Photolithography with a Twist: A workshop on gray scale and 3-D methods*: University of Washington.
66. Arbuckle, D.J. and A.A.G. Requicha. *Massively parallel scanning probe nanolithography*. in *Nanotechnology, 2003. IEEE-NANO 2003. 2003 Third IEEE Conference on*. 2003.
67. Nave, C.R. *Mean Free Path Calculation*. 2011 [cited 2011 10/15/11]; Available from: <http://hyperphysics.phy-astr.gsu.edu/hbase/kinetic/menfre.html#c3>.
68. Elert, G. *Dielectric Strength of Air*. The Physics Factbook 2009 [cited 2011 2011-12-20].
69. Giere, S., M. Kurrat, and U. Schumann. *HV dielectric strength of shielding electrodes in vacuum circuit-breakers*. in *Discharges and Electrical Insulation in Vacuum, 2002. 20th International Symposium on*. 2002.
70. Wittke, J.H. *Electron Column: Electron Source*. GLG 510 - COURSE OVERVIEW 2003 01/18/2006 01:47 PM [cited; Available from: <http://www4.nau.edu/microanalysis/Microprobe/Column-ElectronGun.html>].
71. Facility, C.N.S.a.T. *SPIE Handbook of Microlithography, Micromachining and Microfabrication*. 2010 [cited 2011 2011-12-20].
72. Westover, T.L., et al., *Photo- and thermionic emission from potassium-intercalated carbon nanotube arrays*. *Journal of Vacuum Science & Technology B: Microelectronics and Nanometer Structures*. **28**(2): p. 423-434.
73. Niels de Jonge, Y.L., Koen Schoots, Tjerk H. Oosterkamp, *High brightness electron beam from a multi-walled carbon nanotube*. *Nature*, 2002. **420**: p. 3.
74. Kuo-Shen, C., I.K. Lin, and K. Fu-Hsang, *Fabrication of 3D polymer microstructures using electron beam lithography and nanoimprinting technologies*. *Journal of Micromechanics and Microengineering*, 2005. **15**(10): p. 1894.
75. Bilenberg, B., et al., *High resolution 100 kV electron beam lithography in SU-8*. *Microelectronic Engineering*, 2006. **83**(4–9): p. 1609-1612.

WORKS CITED (continued)

76. L. Dong, S.P., A. T. Friberg, *One-step fabrication of polymer components for microphotronics by gray scale electron beam lithography*. J. Europ. Opt. Soc. Rap. Public. 11010, 2011. **6**.
77. Hung-Lin, Y., J.Y.C. Hu, and Y. Chih-Sheng. *The Study on 3D Electron Beam Lithography for Sub-micrometer Diffractive Optics*. in *Optical MEMS and Nanophotonics, 2007 IEEE/LEOS International Conference on*. 2007.
78. Cumming, et al., *FABRICATION OF 3 NM WIRES USING 100 KEV ELECTRON BEAM LITHOGRAPHY AND POLY(METHYL METHACRYLATE) RESIST*. Vol. 68. 1996, Melville, NY, ETATS-UNIS: American Institute of Physics. 3.
79. al., H.Y.e. in *1st IEEE Intl. Conf. on Nano/Micro Engineered and Molecular Systems*. 2006.
80. Muhammad, M., et al., *Nanopatterning of PMMA on insulating surfaces with various anticharging schemes using 30 keV electron beam lithography*. Journal of Vacuum Science & Technology B: Microelectronics and Nanometer Structures. **29**(6): p. 06F304-6.
81. Worster, J., *The brightness of electron beams*. Journal of Physics D: Applied Physics, 1969. **2**(3): p. 457.
82. Bean, J.C. *Scanning Electron Microscope*. 2005 [cited; Available from: <http://nanohub.org/resources/446>].
83. Yin Ian, Y. and E. Electrical, *Gray-Scale Electron-Beam Lithography*. 2008.
84. Rammohan, A., et al., *One-step maskless grayscale lithography for the fabrication of 3-dimensional structures in SU-8*. Sensors and Actuators B: Chemical. **153**(1): p. 125-134.
85. Ernst-Bernhard, K., *Continuous profile writing by electron and optical lithography*. Microelectron. Eng., 1997. **34**(3-4): p. 261-298.
86. *Controlling resist thickness and etch depth for fabrication of 3D structures in electron-beam grayscale lithography*. Microelectron. Eng., 2007. **84**(12): p. 2859.
87. Gimkiewicz, et al., *FABRICATION OF MICROPRISMS FOR PLANAR OPTICAL INTERCONNECTIONS BY USE OF ANALOG GRAY-SCALE LITHOGRAPHY WITH HIGH-ENERGY-BEAM-SENSITIVE GLASS*. Vol. 38. 1999, Washington, DC, ETATS-UNIS: Optical Society of America. 5.
88. Murali, R., et al. *Process optimization and proximity effect correction for gray scale e-beam lithography*. 2006: AVS.
89. VerticalNews.com. *Studies from Royal Institute of Technology Further Understanding of Electron Beam Lithography*. 2011 [cited; Available from: <http://nanotechnology.verticalnews.com/articles/5312255.html>].

WORKS CITED (continued)

90. Andriy, K., et al., *Chalcogenide glass e-beam and photoresists for ultrathin grayscale patterning*. Journal of Micro/Nanolithography, MEMS and MOEMS, 2009. **8**(4): p. 043012.
91. Schleunitz, A. and H. Schiff, *Fabrication of 3D patterns with vertical and sloped sidewalls by grayscale electron-beam lithography and thermal annealing*. Microelectronic Engineering. **88**(8): p. 2736-2739.
92. Prather, D.W., *Three-Dimensional Nano-Lithography for Emerging Technologies*. 1998.
93. Schleunitz, A., et al., *Selective profile transformation of electron-beam exposed multilevel resist structures based on a molecular weight dependent thermal reflow*. Journal of Vacuum Science & Technology B: Microelectronics and Nanometer Structures. **29**(6): p. 06F302-06F302-4.
94. Liu, D., et al., *Fabrication of polynomial 3-D nanostructures in Si with a single-step process*. Journal of Micro/Nanolithography, MEMS and MOEMS. **10**(1): p. 010501-3.
95. Xia, Y. and G.M. Whitesides, *SOFT LITHOGRAPHY*. Annual Review of Materials Science, 1998. **28**(1): p. 153-184.
96. Benyus, J.M., *Biomimicry: Innovation Inspired by Nature*. 1997, New York, NY: Harper Perennial.
97. Thomas, B.T. and E.J. Smith, *The Parker Spiral Configuration of the Interplanetary Magnetic Field Between 1 and 8.5 AU*. J. Geophys. Res., 1980. **85**(A12): p. 6861-6867.
98. Istvan Hargittai, C.A.P., *Spiral Symmetry*. 2000, Singapore: World Scientific Publishing Co.
99. Yue, C.P. and S.S. Wong, *Physical modeling of spiral inductors on silicon*. Electron Devices, IEEE Transactions on, 2000. **47**(3): p. 560-568.
100. Mostovoy, M., *Ferroelectricity in Spiral Magnets*. Physical Review Letters, 2006. **96**(6): p. 067601.
101. Brown, E.R., et al., *Photomixing up to 3.8 THz in low-temperature-grown GaAs*. Applied Physics Letters, 1995. **66**(3): p. 285-287.
102. Physorg.com. *New nano-detector very promising for remote cosmic realms*. 2007 1/17/2007 [cited; Available from: <http://www.physorg.com/news88256927.html>].
103. Department of Physics, U.o.C. *State-of-the-art Electron Beam Lithography*. 2012 [cited; Available from: <http://www.phy.cam.ac.uk/research/sp/ebli.php>].
104. MicroChem, *NANO™PMMA and Copolymer*. 2001: Newton, MA.
105. GmbH, R., *Ultra high resolution electron beam lithography and nano engineering workstation*. 2005: Dortmund, Germany.
106. GmbH, R., *e_LiNE Manual*. 2005.

WORKS CITED (continued)

107. GmbH, R., *3-dimensional E-beam Lithography Software: Users Manual*. 2004.
108. GmbH, R., *"3Lith" adds the 3rd Dimension*. 2004.
109. MicroChem, *NANO PMMA and Copolymer Developer*. 2001.
110. Zheng, D.A.Z., et al., *Developer-free direct patterning of PMMA/ZEP 520A by low voltage electron beam lithography*. *Journal of Vacuum Science & Technology B: Microelectronics and Nanometer Structures*. **29**(6): p. 06F303-7.
111. Arne, S. and S. Helmut, *Fabrication of 3D nanoimprint stamps with continuous reliefs using dose-modulated electron beam lithography and thermal reflow*. *Journal of Micromechanics and Microengineering*. **20**(9): p. 095002.
112. Advanced Diamond Technologies, I. *NaDiaProbes™: All-Diamond AFM Probes*. 2011 [cited; Available from: <http://www.thindiamond.com/products/nadiaprobes/>].
113. Instruments, D., *Scanning Probe Microscopy Training Notebook*. 3 ed. 2000: Veeco Metrology Group. 57.
114. ASM. *AFM probes*. 2007 [cited; Available from: <http://www.asmicro.com/Supplies/probes.htm>].
115. Lithography, M. *Mapper technology*. 2011 [cited; Available from: <http://www.mapperlithography.com/>].
116. Clarke, P. *TSMC set to receive Matrix 13,000 e-beam litho machine*. 2012 [cited].

APPENDICES

APPENDIX ACalculation

Wavelength of an electron accelerated by 10 kV.

1/26/12 3:15 PM MATLAB Command Window 1 of 1

```
>> E = 10000
```

```
E =
```

```
10000
```

```
>> e = 1.602*10^-19
```

```
e =
```

```
1.6020e-019
```

```
>> c = 2.9979*10^9
```

```
c =
```

```
2.9979e+009
```

```
>> c = 2.9979*10^8
```

```
c =
```

```
299790000
```

```
>> (E*e)/c
```

```
ans =
```

```
5.3437e-024
```

```
>> h = 6.626e-34
```

```
h =
```

```
6.6260e-034
```

```
>> l = h/ans
```

```
l =
```

```
1.2400e-010
```

```
>>
```

APPENDIX BCopyright Reprint Approvals

APPENDIX B (continued)



Wednesday, February 08, 2012

Andrea Antunes
Universidade Federal de Uberlândia
Avenida João Naves de Ávila - 2121 – Caixa Postal 593, Prédio 1X
Uberlândia - Minas Gerais - Brasil
CEP: 38.400-902

I am writing to request permission to use the figures (mentioned below) from your publication "Analysis of the healthy rabbit lens surface using MAC Mode atomic force microscopy" (doi:10.1016/j.micron.2006.04.006) in my thesis. This material will appear as originally published. Unless you request otherwise, I will use the conventional style of the Graduate College of the University of Illinois at Chicago as acknowledgment.

Figure 4 and figure 5

A copy of this letter is included for your records. Thank you for your kind consideration of this request.

Sincerely,

Evan Zaker

Nanotechnology Core Facility (NCF)
University of Illinois at Chicago
Room 3064, Engineering Research Facility
842 W. Taylor St.
Chicago, IL 60607-7022

The above request is approved.

Approved by: Andrea Antunes Pereira Date: March 08, 2012

APPENDIX B (continued)



Wednesday, January 18, 2012

DAC International
Attn: Trademark Department
6390 Rose Lane
Carpinteria, CA 93013

I am writing to request permission to use your image of the product 'MLC Mill / Lathe Combo – Series IV' (<http://www.dac-intl.com/wp-content/uploads/48-4x.jpg>) from your products web site. The image will be used originally as published, except for changes in size or print quality. Each time this image is used, it will be clearly labeled as the "DAC International MLC Mill/Lathe Combination System" and display a link to the website: www.dac-intl.com.


A copy of this letter is included for your records. Thank you for your kind consideration of this request.

Sincerely,

Evan Zaker

Nanotechnology Core Facility (NCF)
University of Illinois at Chicago
Room 3064, Engineering Research Facility
842 W. Taylor St.
Chicago, IL 60607-7022

The above request is approved.

Approved by:  Date: January 23, 2012
Linda S. Silbert
Sales & Marketing Manager
DAC International, Inc.
6390 Rose Lane
Carpinteria, CA 93013

APPENDIX B (continued)



Wednesday, January 18, 2012

Danton H. O'Day

Professor Emeritus

University of Toronto Mississauga, Department of Biology

University of Toronto, Department of Cell & Systems Biology

I am writing to request permission to use of pictures, listed below, from your publication "Development of the Eye: A Series of Inductive Interactions" (<http://www.utm.utoronto.ca/~w3bio380/lecture17.htm>) in my thesis. This material will appear with minimal editions. Unless you request otherwise, I will use the conventional style of the Graduate College of the University of Illinois at Chicago as acknowledgment.

Use is requested for the below pictures.

<http://www.utm.utoronto.ca/~w3bio380/picts/lectures/lecture17/LensStructure1.jpg>

<http://www.utm.utoronto.ca/~w3bio380/picts/lectures/lecture17/Eye1.h13.jpg>

A copy of this letter is included for your records. Thank you for your kind consideration of this request.

Sincerely,

Evan Zaker

Nanotechnology Core Facility (NCF)

University of Illinois at Chicago

Room 3064, Engineering Research Facility

842 W. Taylor St.

Chicago, IL 60607-7022

The above request is approved.

Approved by:

Danton H. O'Day

Danton H. O'Day

Date:

2012.01.21 14:31:20 -05'00'

APPENDIX B (continued)



Monday, May 14, 2012.

Bruce Gaynes, OD, Pharm D
Loyola University Chicago
Stritch School of Medicine

I am writing to request permission to use your image 'rabbit lens fibers SEM.jpg'. I will use the conventional style of the Graduate College of the University of Illinois at Chicago as acknowledgment.

A copy of this letter is included for your records. Thank you for your kind consideration of this request.

Sincerely,

Evan Zaker

Nanotechnology Core Facility (NCF)
University of Illinois at Chicago
Room 3064, Engineering Research Facility
842 W. Taylor St.
Chicago, IL 60607-7022

The above request is approved.

Approved by: _____

A handwritten signature in black ink, appearing to read "E. Zaker", written over a horizontal line.

Date: _____

5/17/2012

VITA

NAME: Evan Zaker

EDUCATION: B.S., Electrical Engineering, Northern Illinois University, DeKalb, IL, 2005
M.S., Electrical and Computer Engineering, University of Illinois at Chicago, 2012

PUBLICATIONS: K. G. Punchihewa et al., "Improvements of the Sensitivity and Operating Range of MEMS-based Resistive-type Vacuum Gauges," Technical Digest, 24th International Vacuum Nanoelectronics Conference, paper O10-5, p.50, July 18 - 22, Wuppertal, Germany (2011).

T. Dankovic et al., "Extension of Operating Range towards Lower Pressures of MEMS-based Thermal Vacuum Gauges by Laser-induced Heating", Poster, Eurosensors XXVI [Pending]

K. G. Punchihewa et al., "Comparisons between Membrane, Bridge and Cantilever Miniaturized Resistive Vacuum Gauges", Sensors (ISSN 1424-8220; CODEN: SENS9) [Pending, accepted 2012-06-11]

E. Zaker et al., "Thermal-based MEMS vacuum gauges for measuring pressures from 10⁻² Torr to 10⁻⁶ Torr", 25th International Vacuum Nanoelectronics Conference [Pending]

PROFESSIONAL: Process Control Engineer Lead, Archer Daniels Midland, 2005-2010